In vivo monitoring of elastic changes during cancer development and therapeutic treatment

Heldmuth Latorre Ossa

▶ **To cite this version:**

Heldmuth Latorre Ossa. In vivo monitoring of elastic changes during cancer development and therapeutic treatment. Medical Physics [physics.med-ph]. Université Paris-Diderot - Paris VII, 2012. English. NNT : . pastel-00786531

HAL Id: pastel-00786531
https://pastel.hal.science/pastel-00786531

Submitted on 8 Feb 2013

HAL is a multi-disciplinary open access archive for the deposit and dissemination of scientific research documents, whether they are published or not. The documents may come from teaching and research institutions in France or abroad, or from public or private research centers.

L'archive ouverte pluridisciplinaire **HAL**, est destinée au dépôt et à la diffusion de documents scientifiques de niveau recherche, publiés ou non, émanant des établissements d'enseignement et de recherche français ou étrangers, des laboratoires publics ou privés.

THESE

pour obtenir le titre de

Docteur de l'Université Paris Diderot

Spécialité : **Physique**

préparée à l'Institut Langevin

dans le cadre de l'Ecole Doctorale ***Matière condensée et interfaces***

présentée le 15 novembre 2012 par :

Heldmuth Latorre Ossa

In vivo monitoring of elastic changes during cancer development and therapeutic treatment

Directeur de thèse : **Mickaël Tanter**

Co-directeur de thèse : **Jean-Luc Gennisson**

Devant le jury composé de :

Lori Bridal	Rapporteur
Aline Criton	Examinateur
Stefan Catheline	Rapporteur
Patrice Flaud	Examinateur
Jean-Luc Gennisson	Co-directeur de thèse
Mickaël Tanter	Directeur de thèse

Acknowledgments

Many people contributed to this work in one way or another during this three-year adventure called PhD. Hence, I would need tons of paper if I was to name each of them. I would love to write everybody's name, but unfortunately, I do not have the amount of paper or the time such a task would require.

I would specially like to thank:

- La Fondation Pierre Gilles de Gennes, which financially supported me during three years through their PhD fellowship.
- My two directors Mickaël Tanter et Jean-Luc Gennisson for their unconditional support throughout this long but enriching process. They were always beside me, not to let me give up when I thought I was about to.
- My colleagues from the different research teams with whom I collaborated: Foucauld Chamming's, Laure Fournier and Olivier Clement (Hôpital Européen Georges Pompidou); Johanne Seguin and Nathalie Mignet (Faculty of Pharmacy of l'Université Paris Descartes); Emmanuel Farge, Maria Elena Sanchez and Sandrine Barbier (Institut Curie-Mechanics and Genetics of Embryonic and Tumoral Development group); and Anne Tardivon and Alexandra Athanasiou (Institut Curie-Radiology department).
- My colleagues at l'Institut Langevin: Patricia Daenens and Abdelhak Souilah for their technical support.
- My colleagues and close friends at l'Institut Langevin: Mademoiselle Christelle Jacquet et Maximin Jean Emmanuel Cès, who became an additional reason for me to come to the institute every day.
- All the members of the jury, who devoted hours of their busy time to read the manuscript, suggest modifications and attend the defence.
- My family, who always believed I was going to succeed despite the difficulties I encountered.

This PhD has been a tough but excellent experience. My bosses would say that I have learned about ultrasonic imaging, Matlab programming and elastography imaging among other subjects. All this is true. However, if someone asks me what I have learned from my PhD, I would reply: "I've learned that there's nothing a human being cannot accomplish if things are done with passion. I've learned that self-confidence is extremely important if we are to achieve a goal, and I've learned that there will always be some people who will try to make you believe you will not be able to succeed, but that there will also be many more who will believe you can".

Gracias totales ☺.

TABLE OF CONTENTS

General Introduction

Medical imaging is an important, rapidly growing field which groups all the existent imaging modalities. The development of this field has been boosted by the necessity of better understanding and early detecting of a wide range of complex human pathologies. The characteristics of each imaging modality make them more or less suitable for an organ within the human body. Currently, there exist several techniques such as: Ultrasound Imaging (US), Magnetic Resonance Imaging (MRI), X-rays, Computer Tomography (CT), and Positron Emission Tomography (PET) among others. Amid these imaging modalities, US is one of the most popular among clinicians, due to being a "clean" technology which does not pose any risk to patients and to be much more affordable and easier to implement than other imaging techniques.

Ultrasound imaging is based on the propagation of acoustic waves in biological tissues. This technique allows to monitor the human body in real time and to acquire grayscale images from ultrasound signals which have been reflected by different types of biological tissues within the body. Therefore, the images offer only part of the information contained on the reflected waves. Nevertheless, in order to fully exploit information from the reflected signals, other ultrasound-based techniques have been developed during the past decades. For instance, "2D-Colour Flow Imaging" (better known as Doppler Imaging), which allows the retrieval of the blood flow, has become particularly useful in the diagnosis of cardio-vascular pathologies. Aiming to improve tissue characterization, as conventional ultrasonic images offer only qualitative morphological information, another technique called Static Elastography appeared by the late nineties. This technique permitted the qualitative estimation of the tissue elasticity, a parameter which plays a key role in tissue characterization. Later, a technique named Transient Elastography was developed during the doctorate of S. Catheline and L. Sandrin. This technique studied the generation and propagation of shear waves. In fact, at low frequency, the human body behaves like an elastic solid. Thus, it is possible to generate shear waves within the body and to assess their speed which is directly related to the medium elasticity. The impulse elastography technique opened the path for what is today known as the Supersonic Shear Wave Imaging (SSI) technique, which utilizes acoustic radiation force to excite the medium and generate shear waves and ultrafast imaging to track their displacement; offering a quantitative estimation of the tissue elasticity. Other dynamic elastography techniques such as sonoelastography and Magnetic Resonance Elastography which study the shear wave propagation have been developed. These dynamic elastography techniques possess their own advantages and limitations, but none of

them is able to follow the shear wave propagation in real time, an essential aspect in the retrieval of biological tissue elasticity.

The SSI technique has proved to be instrumental in the detection and monitoring of human cancerous tumours. This technique is the base of the work contained in this manuscript. The results of several studies in which tissue mechanical parameters such as elasticity and shear non-linearity are used for the characterization of biological tissues are presented.

This report begins with the elastography state of the art, in which a brief overview of the most relevant elastography techniques developed during the last decades is given. Particular emphasis is placed on the SSI technique due to being the core of this work. This information could be relevant for those readers who are not very familiar with the elastography imaging modalities.

In Chapter 2, the results of a clinical study performed in collaboration with *l'institut Curie* on thirty-three patients presenting breast cancer lesions are introduced. The clinical protocol was divided in two parts: Protocol I and Protocol II. In Protocol I, 3D-US was used to calculate the tumour volumes of twenty-three patients. These volumes were then compared to MRI calculated volumes in order to measure the degree of agreement between both imaging modalities for volume retrieval. In Phase II, ten patients (different from the ones taking part in Phase I) were monitored by using 3D-US and 3D-SWE as they underwent neo-adjuvant chemotherapy treatment. 3D-US was used to measure tumour volume (as done in Protocol I) and 3D-SWE to measure the tumour elasticity at each time measurement point. The aim was to evaluate the feasibility of using 3D-SWE to monitor the chemotherapy treatment efficiency along with tumour volume, which is currently the most important parameter used by clinicians to determine the efficiency of a chemotherapy treatment.

Although clinical studies are extremely important in medical research, they possess their own limitations. For instance, the degree of experimental flexibility is much more reduced than in pre-clinical studies not to put the patient's health in danger. Chapter 3 presents the results of a pre-clinical study performed on mice in collaboration with *L'hôpital Européen Georges-Pompidou (HEGP)*. The study was also divided into two parts: Phase I (tumour growth) and Phase II (chemotherapy). During Phase I, a representative human breast carcinoma was implanted on the flank of immune deficient female mice. US and the SSI techniques were used to measure the tumour volume and elasticity respectively from the moment the tumours become large enough to be monitored. In Phase II, the same type of human breast carcinomas were implanted in a different population of mice. The mice begin to receive a neo-adjuvant chemotherapy treatment when the tumours reached an approximate diameter of 2 cm. US and the SSI techniques were used to measure the tumour volume and

elasticity respectively during chemotherapy. The goal of this pre-clinical protocol was to understand the pathology underlying stiffness. In other words, to comprehend how and which physio-pathological parameters (cellularity, microvascular density, fibrosis and necrosis) are correlated with tissue stiffness.

Since there exists different kinds of anti-cancerous therapies depending on the characteristics and state of the lesions, the information retrieved from studies performed with a given treatment may not be directly transposable to other types of therapies. Chapter 3 introduces the results of another pre-clinical study performed in mice in collaboration with researchers from the faculty of Pharmacy of *L'Universite Paris V Descartes.* Human colon carcinomas were implanted in the flank and in the abdominal cavity of female mice. An antivascular treatment, which attacks the tumour vascular network and whose effects appear much earlier than in chemotherapy treatment, was administered to the mice beginning twelve days after tumour implantation. As done in the protocol presented in Chapter 3, US and the SSI techniques were used to measure the tumour volume and elasticity respectively five days after the implantation. This pre-clinical study intended to know if this particular type of therapy would cause a change in the tumour elasticity, and if this change would take place earlier than the change in the tumour size, which as it was said before, is currently the most important criteria to decide whether a given anti-cancerous treatment is causing a positive effect on the patient or not.

From the beginning of this work, only tissue elasticity has been the parameter employed for the characterization of biological tissues. Nevertheless, in some cases, elasticity may not be sufficient to determine the pathological state of a biological tissue. Chapter 5 presents the development of a technique combining static and dynamic elastography for the retrieval of an additional tissue mechanical parameter: the third order non-linear shear parameter . Here, the first known 2D non-linear shear elasticity maps are presented. The results of the experiences were performed on tissue mimicking phantoms and on beef liver samples. The technique developed was used in *ex vivo* experiences on mice colon to determine the amount of stress induced to the colons by the interaction between a magnet and ferro-magnetic liposomes previously injected into the colon. The induced stress intended to emulate the stress induced by tumour growth on neighbouring tissues, which seemingly plays a key role in the development of cancer tumours in tissues with a genetic cancer predisposition.

1. Chapter 1. Elastography: an important medical imaging research field

1.1 Introduction

It is widely known that the presence of cancerous tumours can be detected by medical palpation [1]. In fact, it is during this medical procedure that clinicians intuitively try to assess the Young's modulus of the tissue (which is a physical parameter linked to the tissue elasticity) in order to determine the presence of any tissue abnormality, due to the fact that the pathological state of a tissue is commonly associated with its elastic properties at the macroscopic level. This concept is the base of a medical imaging technique called ultrasound elastography, which has found great applicability in the detection of breast lesions. Since the 70s, Ultrasound Elastography has gradually become a powerful medical imaging technique as it offers real time qualitative, quantitative and functional information on the inner structure of the human body. However, the technique has its limitations as in some cases it is not able to offer the required information on the areas of interest. This has inspired several scientists who tried to use other techniques to complement the elastography results. R. Dickinson [2] had the idea in 1981 of quantifying the body's natural vibrations. He designed an ultrasound signal correlation method to quantify the amplitude and the frequency of these vibrations. He proposed a relationship between the human organs' elasticity and their natural displacements. Two years later, A. Eisencher [3] exploited, for the first time, the propagation of elastic waves. His idea consisted in replacing the human vibrations by controlled mechanical vibrations. He called his technique echosismography and it consisted in combining conventional ultrasound with the use of an external vibrator. He showed that it was possible to qualitatively interpret the images obtained by this technique to determine different elasticity areas (Fig 1.1). The applied vibrations were distinguishable on the image and the analysis of their amplitude allowed (with some experience) the determination of tumour lesions (pointed out by the white arrow on Fig 1.1). In this way, Eisencher showed the feasibility of detecting the presence of hard masses surrounded by healthy tissue. His work set the basis for the development of the dynamic elastography domain.

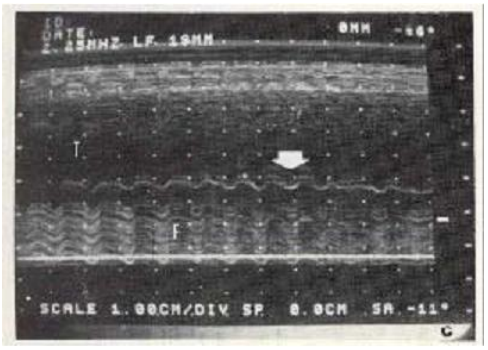

Fig 1.1. One the first echosismography images of human breast. The qualitative analysis of the obtained vibrations allows the discrimination of areas of different elasticity [4].

Another pioneer in the elastography domain is J. Ophir [5]. In the 90's, he suggested that the use of ultrasound was sufficient to determine the elasticity of biological soft tissues. His technique was based on the simple comparison of several ultrasound images acquired before and after the application of static compression on the medium under investigation. Thus, he substituted the external vibrations by the static compression.

The work of Eisencher and Ophir set the foundations for all the currently existing ultrasound elastography modalities, which can be classified into static and dynamic elastography depending on the sort of mechanical excitation employed. Dynamic elastography techniques can then be sub-classified in monochromatic and transient as it will be described further in this chapter. Explaining all the existing elastography modalities constitutes a big challenge. Hence, in this chapter, only a brief explanation of the most important elastography techniques will be given, before focusing on the structure and main characteristics of the transient elastography technique which constitutes the core of this work.

1.1.1 Static Elastography

Ultrasound static elastography was first introduced in 1991 by Ophir [5]. It consists in measuring the displacement induced within the tissue by a continuous mechanical force. This technique is based on Hooke's law which states that for homogenous and isotropic material, the deformation (ε) is directly proportional to the uni-axially applied stress (σ) (see Eq. 1); where E represents the elastic Young's modulus of the material.

$$\sigma = E\,\varepsilon \qquad Eq.1$$

The static elastography technique employs an external, quasi-static uni-axial source of compression such as mechanical actuators to compress the tissue and generate displacement and strain (Fig 1.2). Local strains are derived from the ultrasonic backscatter signals before and after compression by the 2D cross-correlation of the ultrasound pre and post compression data. This technique thus produces qualitative deformation gradient images (elastograms) (Fig

1.3) which are easy to interpret as long as the applied stress is relatively uniform. The technique is based on the physical principle that the lower the Young's modulus of a material, the higher the strain or deformation.

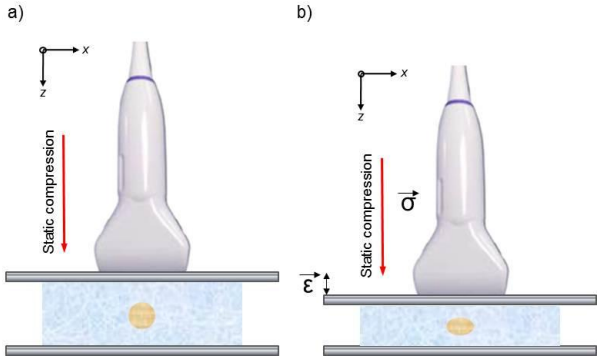

Fig 1.2. Static Elastography principle. Axial-compression (σ) is applied to the medium to cause a deformation (ε); a) medium before compression and b) after compression.

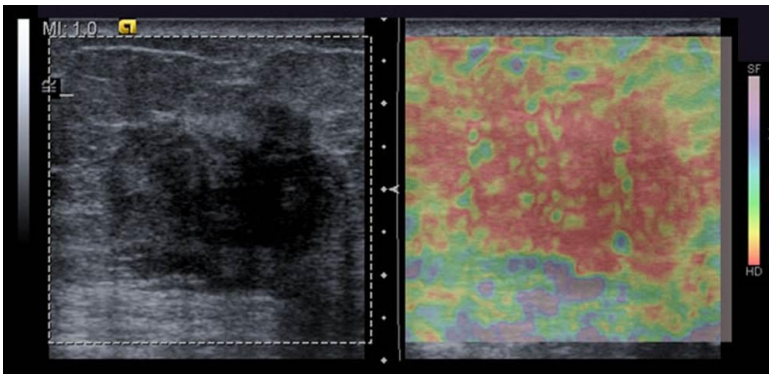

Fig 1.3. (Left) Echographic image of a biopsy proven breast carcinoma; (Right). The elastogram depicts the deformation caused by the quasi-static compression for each pixel on the image. The lesion appears significantly stiffer (reddish) than its healthy surrounding tissue. eSie TouchTM software elasticity imaging – ACUSON S200 ultrasound system (SIEMENS).

The efficiency of static elastography as a complementary medical imaging tool has been shown [6][7]. It has the advantage of being relatively easy to apply. Moreover, the fact that the ultrasound probe can be used to produce localized compression near the region of interest for the breast and other superficial targets make it an appealing imaging technique. However, it possesses some limitations for *in vivo* imaging: the boundary conditions are not taken into account; nearly uniform stress must be applied in order to be able to interpret the images which renders it very operator dependant; the targets tend to move out of plane during compression; it is difficult to compress deeper organs and the elastograms give only qualitative information since the amount of applied compression is unknown and hard to control.

In order to overcome the limitations of static elastography and more importantly, to obtain quantitative elasticity maps, new elastography modalities have been developed in the last decade. Unlike static elastography, these new modalities known as dynamic elastography

techniques, do not excite the tissue by mechanical means but employ a vibrating force (sonoelastography) [8], a given frequency shift (vibroacoustography) [9], a very short impulsion (transient elastography) [10] or acoustic radiation force [11][12]. All these methods have shown their efficiency to determine elastic properties of biological soft tissues, as they give access to quantitative elastograms with better resolution than the qualitative ones obtained through static elastography. Nonetheless, they are slightly more difficult to implement since they need more complex setups able to generate and detect shear waves. A brief explanation of the principal dynamic elastography methods is given as follows.

1.1.2 Dynamic Elastography

Parallel to the static elastography technique, dynamic elastography methods based on shear wave propagation were also developed. The biggest advantage lies on their capability to offer quantitative elastograms. Depending on the way the tissue is excited, the dynamic elastography techniques can be classified into monochromatic and transient.

1.1.2.1 Monocromatic

Unlike transient elastography, monochromatic elastography techniques utilize a monochromatic (continuous) source to excite the tissue. The shear wave velocity is then retrieved by ultrasonic (sonoelastography and vibro-acoustography) or magnetic resonance (magnetic resonance imaging) imaging methods.

1.1.2.1.1 Sonoelastography

In 1987, *Krouskop et al*. [13] performed the first *in vivo* quantitative measurements of tissue elasticity on amputated limb stumps. In his experiments, a vibrator excited the muscles of the living part of the leg attached to the amputee at a frequency of 10 Hz. The displacements induced by the shear wave propagation were measured by the Doppler effect avec un ultrasound probe. This technique was based on the fact that the frequency shift obtained by the Doppler effect is proportional to the amplitude of the displacements. Then, by applying a simple viscoelastic model, the tissue elasticity could be retrieved. This technique would be later known as sonoelastography.

Sonoelastography is a method that combines mechanical vibrations and ultrasound Doppler imaging. Lerner and Parker carried out later in 1992 [14][15] and in 1998 [8] new experiments on sonoelastography, in which a low frequency vibration (20 to 100 Hz) was externally applied to excite internal vibrations within the tissue under investigation. They believed that the elasticity of a medium was directly connected to the amplitude of the displacements. The hypothesis was that stiffer areas would vibrate at much lower amplitude than softer ones.

The first sonoelastography images show the presence of a hard inclusion within a sponge (Fig 1.4). The level of stiffness was represented by colours. The stiffer areas were depicted in darker colours. Hence, the higher the elasticity the darker the colour and the lower the vibration amplitude. Nevertheless, this simplified approach did not take into consideration the undesirable effects caused by diffraction, dissipation and stationary waves, diminishing the application of the technique for *in vivo* measurements of the elasticity of biological tissues such as muscle.

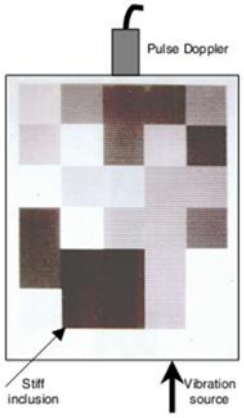

Fig 1.4. First known sonoelastographic image (7x5 cm2). The image shows the vibration within a sponge containing a stiff inclusion (low-dark region). The stiffer regions are represented by darker colours [16].

A second approach was developed by Sato [17][18]. Aiming to overcome the obstacles encountered by the first sonoelastography experiments, his work focused on the visualization of the shear wave propagation. In fact, for any source exciting the surface of an homogenous isotropic medium, two types of waves are generated: a shear wave and a compressional wave. Each wave possess a velocity (V_S and V_P for the shear and compressional wave velocities respectively) which can be expressed with the Lamé coefficients λ and μ as follows:

$$V_S = \sqrt{\frac{\mu}{\rho_0}} \quad and \quad V_P = \sqrt{\frac{\lambda + 2\mu}{\rho_0}} \qquad Eq.2$$

Where ρ_0 is the initial medium density, μ the elastic shear modulus and (λ + 2μ) the elastic modulus of compression. The wave velocities are linked to a couple of independent coefficients (λ, μ) which are expressed as a function of the medium's Young's modulus (E) and Poisson's ratio (ν) [19]:

$$\lambda = \frac{E\,\nu}{(1+\nu)(1-2\nu)} \quad and \quad \mu = \frac{E}{2(1+\nu)} \qquad Eq.3$$

Which means that:

$$E = \frac{\mu(2\mu + 3\lambda)}{\lambda + \mu} \quad and \quad \nu = \frac{\lambda}{2(\lambda + \mu)} \qquad Eq.4$$

Since we deal with biological tissues, which are quasi-incompressible materials ($\nu \approx 0.5$), *Eq. 3* becomes:

$$E \approx 3\mu \qquad Eq.5$$

The medium's Young's modulus is directly linked to the shear wave speed. Moreover, the shear modulus μ is negligible compared to the Lamé coefficient λ. It has been experimentally proven that in soft media, the compressional wave velocity ($V_P \approx 1500$ m/s) is much higher that the shear wave velocity ($V_S \approx 1$ m/s).

It was on measuring the shear wave velocities that S. Levinson focused one of his first *in vivo* studies in 1995. Here, he measured the elasticity evolution as a function of the force delivered by a group of leg muscles (the quadriceps) [20]. He came to the conclusion that the more the group of muscles was contracted, the higher the global Young's modulus (Fig 1.5).

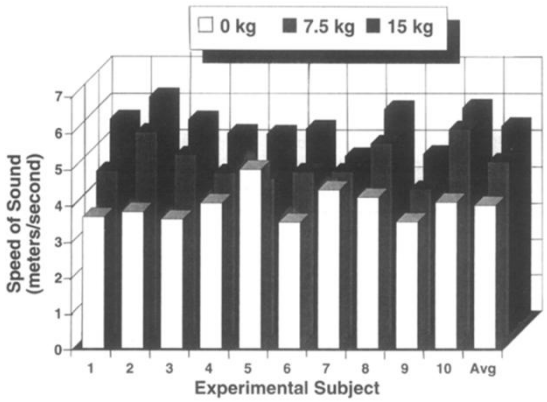

Fig 1.5. Shear wave speed values in ten subjects as a function of the applied load. The values have been averaged over all the eighteen combinations of frequency, knee flexion angle and propagation direction. The speed of sound increased uniformly with increasing load (apart from subject 5), supporting the theoretical link between elasticity and sound speed [20].

There exist a considerable amount of literature on sonoelastography. In their respective work, K. Fujii [21] measured the shear wave velocity by Laser-Doppler Interferometry at several frequencies; V. Dutt and J. Greenleaf [22] employed a method of Quadrature- Phase on the echographic signals and also measured the shear wave velocities for frequencies ranging from 200 to 500 Hz without measuring the elasticity.

Fig 1.6 presents the sonoelastographic image of a biopsy proven cancer tumour. The sonoelatographic image puts in evidence a stiffer zone which appears normal on the B-mode image.

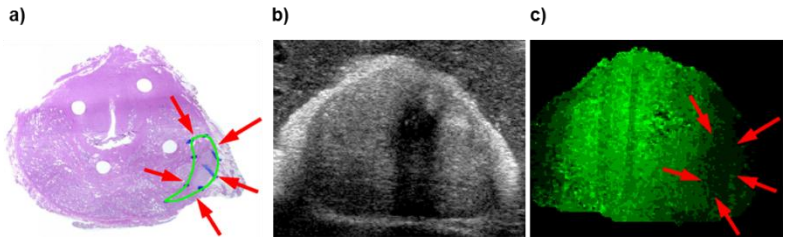

Fig 1.6. Sonoelastography image of a histology proved prostate cancer tumour. a) histologic image portrays the tumour enclosed by the green contour line; b) the corresponding B-mode image obtained on the same plane does not show any kind of tissue abnormality; c) the sonoelastographic image of the same area shows a vibration deficit (red arrows) characteristic of stiffer tissue areas [23].

The sensibility of all these methods to the boundary conditions made it very difficult to interpret the shear wave phase velocity maps. Nevertheless, this obstacle can be overcome by Magnetic Resonance Elastography (MRE), a technique which gives access to the three spatial components of the induced tissue displacement with high accuracy and precision, facilitating the resolution of the inverse problem. It uses the same low-frequency excitation system but the ultrasound imaging system is replaced by a magnetic resonance imaging one.

1.1.2.1.2 Magnetic Resonance Elastography (MRE)

It was initiated in 1995 by J. Greenleaf [24] when the first displacement phase and displacement amplitude images were obtained by using Magnetic Resonance. This technique uses a low frequency vibrator to excite the tissue at a central frequency ranging between 50 and 1000 Hz (usually centred at 100 Hz for human beings) depending on the targeted organ. A special Magnetic Resonance Imaging (MRI) sequence allows the movement codification at the given central frequency. A stroboscopic technique is then employed to rebuild the three-dimensional movement within the organ from several points taken for each period. The retrieved 2D displacement vector field is used to retrieve the tissue's Young's Modulus. MRE very much depends upon the number of cycles (which is elevated) and permits the measurement of the three components of the displacement vector having a vector base of the right gradient. Its precision for measuring the tissue displacement reaches the 100 nm. The acquisition time depends on the image resolution and can easily achieve several minutes, which makes it impossible to use in moving organs such as the heart and the kidney. Moreover, the mechanical excitation must be "monochromatic", since the displacement acquisition is not instantaneous and requires a perfect synchronization between the MRI device and the low frequency mechanical excitation. Therefore, the observed waves are exclusively monochromatic.

Fig 1.7 presents the MR and MRE images of a breast lesion before and after chemotherapy, where a change in the tissue elasticity pre and post treatment of the lesion is observed.

Sinkus et al. [25] used MRI to show the feasibility of the determination of additional tissue biological parameters such as anisotropy, and its importance when assessing the pathological state of a lesion. Additionally, Oliphant [26] succeeded in estimating the complex shear modulus and showed the feasibility of retrieving the shear viscosity modulus. In vivo studies have been performed. Plewes [27] visualized and quantified the breast mechanical properties and Dresner [28] quantified the biceps elasticity during muscular contraction.

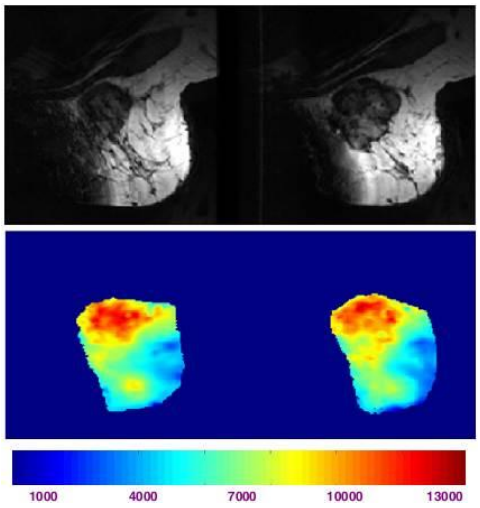

Fig 1.7. Representative MRE study of a breast lesion. (Top) the MR images of a the lesion before and after chemotherapy. (Bottom) Corresponding quantitative elasticity maps based on MRE of the same areas of interest, at both time points. A reduction of the highest values of stiffness is noted after chemotherapy [16].

MRE is particularly useful for imaging the brain since it rests still within the cranial cavity. Even though MRE offers 3D quantitative images of very good resolution, its cost, limited mobility and long acquisition times are important obstacles for *in vivo* imaging studies. In addition to this, the technique is very noise sensitive and the inverse problem is difficult to resolve. Nevertheless, these obstacles can be overcome with the use of impulse elastography, whose main characteristics are explained further in this chapter.

1.1.2.1.3 Vibro-acoustography

As an ultrasound beam propagates through an absorbing medium, the energy transfer results in a second-order effect that produces a force proportional to local intensity and absorption, which is termed radiation force [34]. In 1990, Sugimoto et al [35] came up with a set-up which applied radiation force to a tissue sample while measuring the resulting tissue displacement with an ultrasound probe. The displacement vs. the relaxation curve were fitted to a multi-exponential function as a model of the mechanical properties [16].

M. Fatemi and J. Greenleaf [36] developed a two-frequency method which measured the acoustic responses to the excitation caused by the radiation force of two interfering ultrasound beams. A confocal transducer produced two continuous ultrasound waves whose

frequencies (f and f + Δf) slightly differ and which intersected at the object. The acoustic remote intersection of the two beams produced an oscillating radiation force over the object at the frequency difference which made it vibrate, emitting an acoustic field in the surrounding medium. The beam's remote intersection eliminates the object's acoustic emissions and the transducer's interference. The sound waves generated by the vibration of the object are detected by an hydrophone tuned to the difference frequency (Δf) and filtered by a band-pass filter centred at the same frequency. In order to build a 2D image, the confocal transducers sweep out the entire area in raster scanning like motion (Fig 1.8). The main frequency (f) and the difference frequency (Δf) are in the order of MHz and kHz respectively.

Covering the entire region by the radiation force caused a considerable energy transfer to the medium under test and a relatively long acquisition time, which limited the in vivo applicability of this technique. Moreover, the measured parameter depended on the radiation force and the stiffness and geometry of the vibrating object. Fig 1.9 shows a x-ray mammography of a healthy breast and its corresponding vibro-acoustographic image.

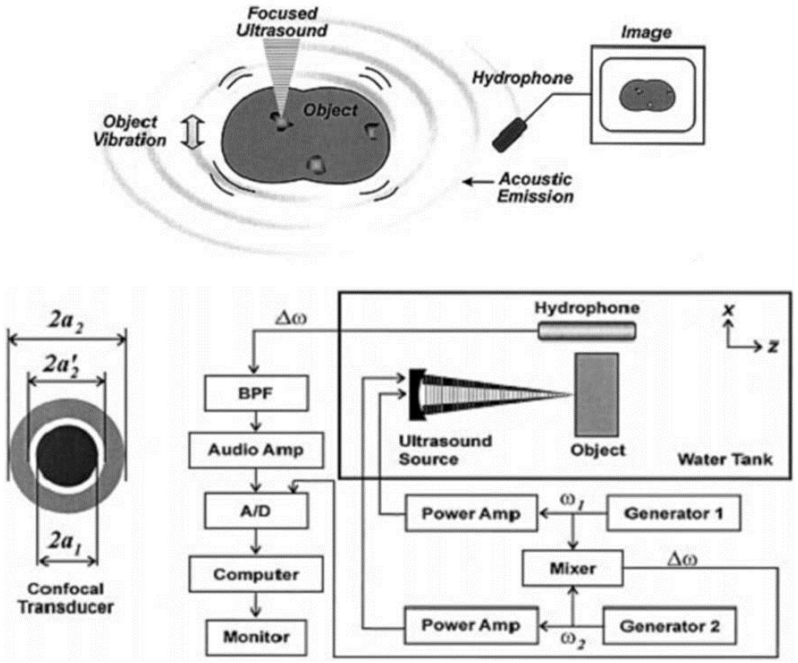

Fig 1.8. Vibro-acoustography system diagram. (Top) A simplified vibro-acoustography set-up. (Bottom)Two continuous wave generators drive these elements at slightly different frequencies. The transducer is focused on the object, with the beams interacting at the joint focal point to produce an oscillating radiation force on the object at the difference frequency. This force causes the object to vibrate and as a result an acoustic emission field is produced in the surrounding medium. This field is detected by the hydrophone and filtered by a band-pass filter centred at the difference frequency. The amplitude of the resulting signal, detected by the detector, is used to modulate the intensity of the image at a point corresponding to the position of the beam on the object. [37].

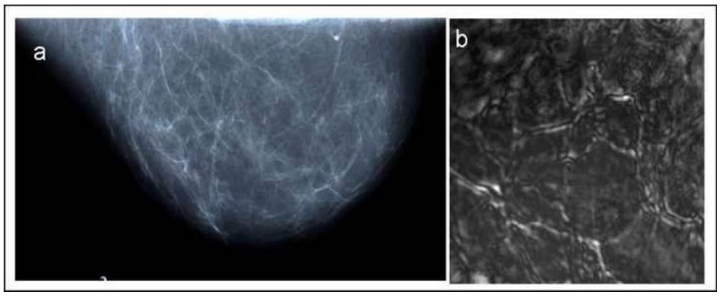

Fig 1.9. Breast Images of a healthy breast. (a) X-ray mammography of the entire breast and (b) its corresponding vibro-acoustographic image focused at 2 cm depth from the skin (Δf = 50 kHz) [38].

Later in 2004, Greenleaf developed a quantitative method called Shear Wave Dispersion Ultrasound Vibrometry (SDUV) [39] to measure stiffness and viscosity of soft tissue non-invasively. SDUV uses a focused ultrasound beam within the FDA power limits to stimulate (within the studied tissue) cylindrical harmonic monochromatic shear waves propagating outwards from the beam axis. The shear wave propagation is tracked using a separate ultrasound beam in pulse\echo mode. The phase of shear wave is measured at two different points within the propagation path and used to retrieve the shear wave speed. This processes is repeated at several frequencies and fitted with a theoretical Voigt dispersion model to inversely solve for tissue viscosity and elasticity.

Despite the fact that the monochromatic excitation elastography techniques offer a quantitative mapping of the tissue elasticity, the disadvantage of the monochromatic vibrations lies on the impossibility to separate the compressional waves from the shear waves, an aspect that can affect the shear wave velocity calculation. This aspect paved the way for the development of new elastography techniques, in which the tissue excitation was not monochromatic but transient.

1.1.2.2 Transient Elastography

Several techniques focus on the propagating shear waves resulting from a transient (impulsive or short tone burst) tissue excitation, whose displacement history along the central axial line can be extracted by ultrasonic techniques. This allows the global estimation of the tissue shear wave velocity and therefore the tissue elasticity.

1.1.2.2.1 1D Impulse Elastography

One-dimensional impulse elastography was born in 1994 during the PhD thesis of S. Catheline [29]. The idea consisted in measuring the tissue elasticity after exciting the tissue not monochromatically like in sonoelastography or MRE but by using a short impulsion. This technique allowed separating the compressional wave (which propagates very rapidly) from the slower shear wave without taking into account the boundary conditions. Therefore, the shear wave (generated by the pulse) displacement was no longer stroboscoped but recorded in

real time by using a conventional ultrasound probe along the entire trajectory. Fig 1.10 illustrates a typical 1D impulse elastography setup.

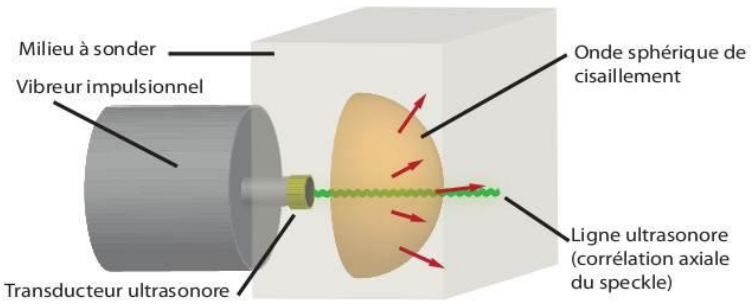

Fig 1.10. The vibrator gives a low frequency touch (about 50 Hz) to the sample, generating a compressional and a shear wave. The ultrasound probe (which is placed over the vibrator) permits monitoring the shear wave propagation within the medium by using speckle axial correlation more than 1000 times/s. Therefore, the shear wave velocity and the material's Young's modulus can be retrieved [31].

Initially, a shear wave and a spherical compressional wave were generated when a circular piston (with a diameter ranging from 5 to 20 mm) slightly touched the medium [30]. A 3 MHz transducer placed right in front of the piston and focused, permitted to image the entire area of interest. The displacement generated within the medium by the shear wave propagation was then retrieved by correlating the back-scattered echo signals using an ultrasound probe more than 1300 times (repetitions) per second [4]. Finally, the shear wave velocities were retrieved from a spectral analysis around the displacement central frequency. Therefore, the Young's modulus of the medium (considered as isotropic and non-viscous) could be retrieved using the expression on the left side of Eq. 2.

The technique was first tested mainly on agar-gelatine tissue mimicking samples which simulated the properties of biological tissues. These materials have the advantage of being homogeneous, isotropic, viscoelastic and linear. This method was then employed to perform measurements in the skin and muscles by J. Gennisson [4]. Due to its effectiveness, the technique has been commercialized as *Fibroscan*® and permits to characterize the liver fibrotic state by giving a global score based on the mean elasticity. This non-invasive imaging technique can avoid performing biopsies in some cases. Fig 1.11 portrays the shear wave displacement simulation with the Green's function (left) and the wave-front displacement as a function of depth and time in human muscle (right).

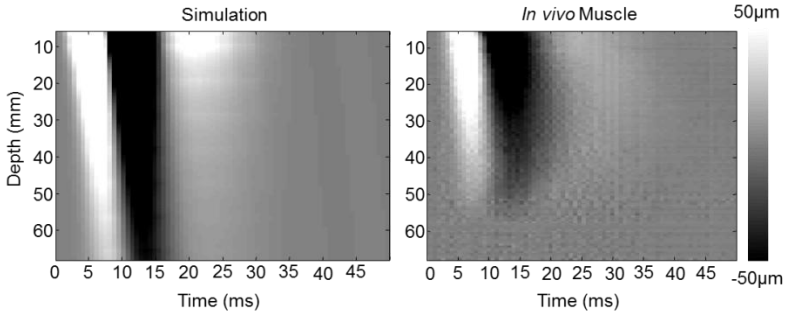

Fig 1.11. 1D-Transient Elastography. Shear wave displacement as function of the depth and time in (left) a simulated environment and (right) human muscle in vivo[4].

The 1D transient impulse elastrography technique allowed the determination of the Young's modulus of isotropic materials along the beam axis. However, in order to retrieve the complete 2D Young's modulus map of the medium, the shear wave front propagation must be tracked in two dimensions with conventional ultrasound probes. Thus, it is necessary to have a ultrasonic frame rate (frequency) high enough to catch the shear wave propagation in real time, which reaches a few meters per second. Therefore, a frame rate of a few thousands of images per second is needed. At that time, the echographic systems were limited to 50 images per second, which was too low for following the shear wave propagation. Hence, an ultrafast imaging system was developed to meet with the high frame rate requirements. Such system was part of a technique initially known as 2D impulse elastography.

1.1.2.2.2 2D Impulse Elastography

Continuing with the development of the one-dimensional impulse elastography technique, some features were upgraded. In 1997, an echographic device used for acoustics time reversal experiments was adapted to perform ultrafast imaging [32] based on the emission of ultrasound plane waves. The system was composed of 128 independent emission\reception channels, each one with a 2 MB memory capacity. The ultrasound signals were sampled at 50 MHz. The transducer was fixed to a mechanical vibrator capable of generating shear waves within the medium at a frequency of 100 Hz (Fig 1.12 - right). The entire system was then controlled by a computer (Fig 1.12 - left). Once the shear wave propagation film was reconstructed, the inversion of the wave equation allowed the retrieval of the complete 2D Young's modulus map of the medium. This system was known as two-dimensional impulse elastography.

Fig 1.12. (Left) ultrafast imaging system. The electronic system composed by 128 independent channels (emission/reception), allows the acquisition of the echo-signals coming from each of the 128 elements of the probe. The entire system is controlled through a computer. (Right) The ultrasound probe (linear array) is fixed to a vibrator which excites the tissue to generate the shear waves[4].

An ultrafast imaging sequence takes place as follows:

Initially, unlike a conventional echographic device, there is not beamforming during the emission. Therefore, the ultrasonic image is not formed by emitting a series of focused ultrasound beams to cover the complete region of interest (Fig 1.13(a)) but by emitting a single ultrasonic plane wave by all the probe transducers (Fig 1.13(b)) at the same time. The acquired backscattered signals are subsequently saved and post-processed. The displacements generated by the shear wave propagation are then calculated by the cross-correlation of consecutive images as done in the 1D version of the technique. In this way, only a single emission is needed to obtain a complete ultrasound image of the medium. This method allows the acquisition of approximately 8000 raw RF data images per second.

The resolution of the inverse problem in two dimensions of the shear wave propagation permitted the retrieval of the 2D velocity map and therefore the 2D elastic map of the medium.

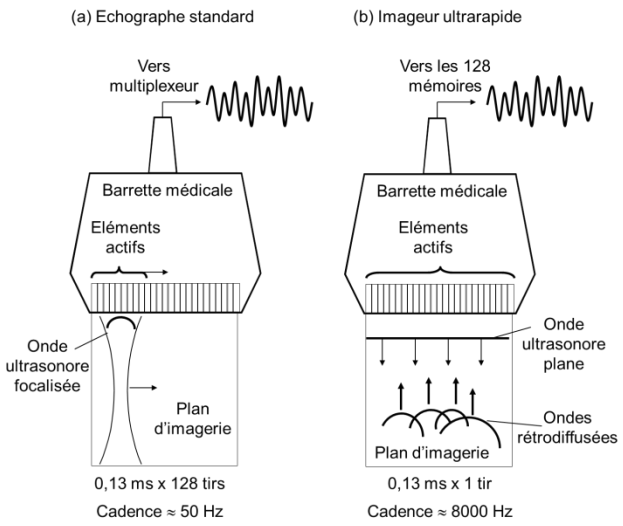

Fig 1.13. (a) Schematic principle of a classical ultrasonic device. The ultrasound waves are focused at emission, with a time interval of about 0.13 ms between the activation of two neighbouring transducer elements. Such systems can reach an imaging frequency of approximately 50 Hz.(b) Ultrafast imaging principle. The medium is imaged after a single emission of a plane ultrasound wave. The shear wave displacements are obtained after post-processing the back-scattered signals. This system can reach an imaging frequency of about 8000 Hz.

The first *In vivo* experiments with this technique on humans were performed in 2003 with encouraging results [33]. Here, the technique was employed on patients presenting breast lesions. The 2D maps of elasticity showed an important elasticity contrast between the lesions and their healthy surrounding tissue (Fig 1.14). However, the device remained bulky and not very practical for *in vivo* experiments.

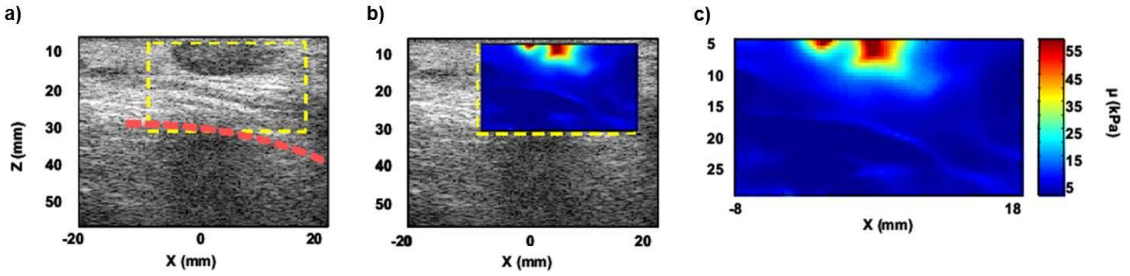

Fig 1.14. Malignant breast tumour (adenocarcinoma): a) The lesion (which is enclosed by the dotted yellow rectangle) appears darker than its surrounding tissue on the echographic image; b) Superposition of the shear modulus map of the same region over the echographic image. The colour-contrast shows that the lesion has a much higher elastic modulus than the surrounding healthy tissue; c) Zoomed shear modulus map of the region of interest [33].

1.1.2.2.3 Acoustic Radiation Force Imaging (ARFI)

The ARFI or Acoustic Radiation Force Method is a dynamic elastography technique method developed by Nightingale *et al.* [40] in 2001, which uses acoustic radiation force to generate localized tissue displacements that are directly correlated with localized variations in tissue stiffness. These displacements are measured using ultrasonic correlation based methods and their magnitude is inversely proportional to the local tissue stiffness. In this method, focused ultrasound is used to apply localized radiation force (pushing) to small volumes of

tissue (2 to 3 mm) for short durations (less than 1 ms). The resulting tissue displacements are mapped using ultrasonic correlation-based methods [40]. Therefore, the ARFI technique allows to track the tissue displacement and relaxation directly after the radiation force has been applied (Fig 1.15). The temporal properties of such relaxation curves permit the retrieval of information regarding the elasticity and viscosity at the focal point only [41]. Moreover, radiation force induced tissue displacements are generated at multiple locations and combined to build a complete quantitative map of tissue stiffness (Fig 1.16). This increases the time needed to build one entire image [42] as well as the tissue temperature due to multiple "pushing". This technique has been used to build quantitative elasticity maps on breast , prostate and liver [43][44].

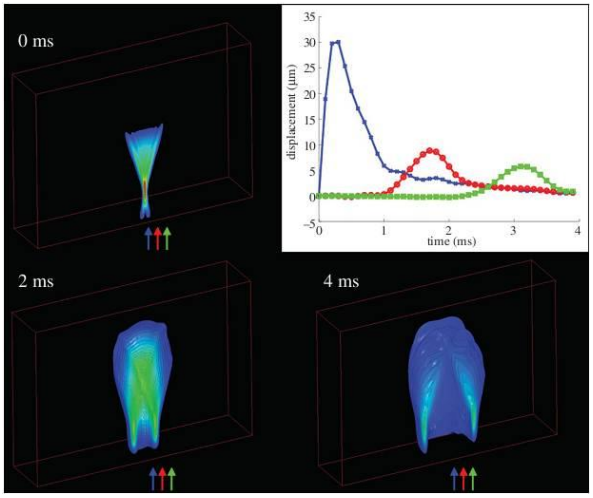

Fig 1.15. 3D finite-element simulation of the shear wave propagation represented as isocontours of displacement at different times after ARFI excitation. The medium was assumed to be purely elastic, with a Young's modulus of 4 kPa and an acoustic attenuation coefficient of 0.7 dB cm^{-1} MHz^{-1}. The 0 ms isocontour image portrays the radiation force region of excitation (ROE). The central axis of this displacement profile is the location used to generate qualitative ARFI images as shown in Fig 1.16. The plot in the upper right shows the displacement-through-time profiles at the axial focal depth of the radiation force excitation at three different lateral positions (indicated by the arrows in the isocontour images). Blue, 0 mm; red, 1.5 mm; green, 3 mm [45].

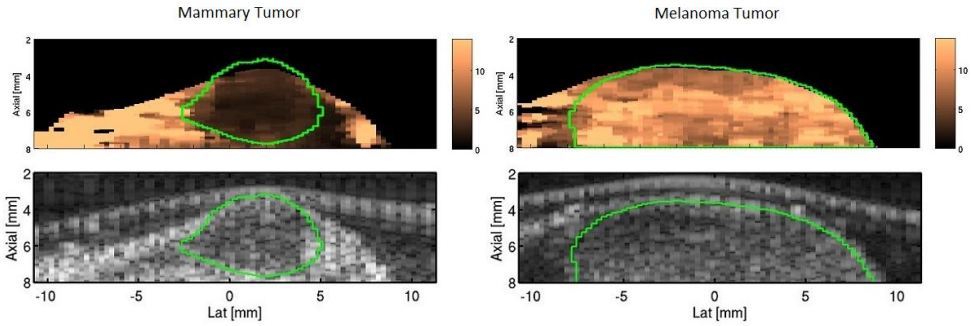

Fig 1.16. Images of a mammary tumour (left) and a melanoma tumour (right) implanted on mice. (Above) ARFI images and (below) the corresponding B-mode images. ARFI imaging uses the acoustic radiation force to generate the "pushing" within the tissue and conventional ultrasonic methods to track their displacements. Although the two tumours are both displayed as slightly anechoic regions in the B-modes images, the mammary tumour appears as a dark, lower displacement region (i.e. stiffer) in the ARFI image, whereas the melanoma tumour appears as a bright higher displacement region (soft) in the ARFI image. Source: http://kathynightingalelab.pratt.duke.edu

1.1.2.2.4 The Supersonic Shear Wave Imaging (SSI) Technic

The SSI technique is a step further in the development of the 2D impulse elastography technique [12]. This dynamic elastography technique born in 2004, utilizes radiation force to excite the medium and generate shear waves and ultrafast imaging to track their displacement. The idea of associating radiation force to the study of generated shear waves comes from Sarvazyan, who introduced the concept of Shear Wave Elasticity Imaging (SWE) in 1998 [46]. It was in 2004 that Bercoff [47] combined two fundamental ideas to overcome the limitations encountered by the 2D elastography technique. These two concepts, radiation force and ultrafast shear wave imaging are the base of the Supersonic Shear Imaging technique. The technique can be subdivided into two basic steps as follows:

- *The Mach-cone creation:* ultrasound waves are focalised successively at different depths to create spherical waves at each focal point. All the generated spherical waves interfere constructively to create a sort of Mach-cone [12] (quasi-plane on the imaging plane and cylindrical in three dimensions) which propagates in opposite directions (Fig 1.17(a)). The constructive spherical wave interference increases the shear wave amplitude and the signal to noise ratio. In the imaging plane, the plane wave front allows the simplification of propagation hypotheses, which is of great interest for the inverse problem. Only one Mach-cone is needed to generate the quasi-plane shear wave fronts that travel across the medium to cover the entire region of interest.
- *Ultrafast Imaging:* ultrasound plane waves are generated to track the shear wave displacement along the entire imaging plane. During a single acquisition, up to 8000 images per second can be acquired. Hence, only one Mach-cone is enough to acquire the complete 2D shear velocity map of the medium (Fig 1.17(b)).

In the SSI technique, the external vibrator employed to generate the shear waves in the 2D impulse elastography technique is replaced by the acoustic radiation force. Therefore, both the excitation and imaging processes are carried out using an ultrasound probe. The generated shear waves have an amplitude (from 0 to the maximum) of several dozens of micrometres and are detectable with a good signal to noise ratio by axial correlation and ultrafast imaging. The latter allows to perform an entire single acquisition in less than 30 ms, imaging in real time the shear wave displacement and permitting the retrieval of the shear wave velocity and the complete 2D quantitative elasticity map of the medium (using Eq. 2 and Eq. 5) with great precision. The Spatial resolution of the elasticity maps obtained with this technique at 8 MHz and 15 MHz are of 1.2 mm and 0.4 mm respectively.

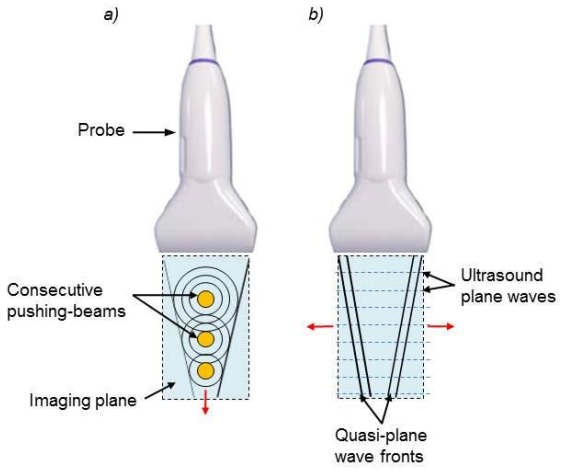

Fig 1.17. The two basic steps of a SSI technique experiment: (a) Generation of the shear wave. (b) Propagation of the quasi-plane wave sources on opposite directions. Acoustic radiation force is used to excite the medium and generate shear waves. Then, by using ultrafast imaging, the shear wave displacement is tracked. Only one Mach-cone is needed to image the entire region of interest. The entire imaging process take less than 30 ms.

The SSI technique is also not very sensitive to breathing movement. As in 2D Impulse Elastography, the shear elasticity maps are obtained by the inversion of the wave equation. Bercoff [47] developed the technique for the first prototypes and acquired the first *in vivo* images within the frame of his doctorate.

Nowadays, the techniques based on the application of the acoustic radiation force to excite the tissue (ARFI and SSI) are very popular due to the fact that they give very accurate quantitative estimation of the tissue elasticity and being very suitable for *in vivo* applications. Whereas today ARFI offers a quantitative elasticity value only at one given location at a time, the ultrafast ultrasonic imaging capabilities of the SSI technique give the ability to produce full quantitative elasticity maps of the medium in real time.

Tanter *et al* [48] performed a first clinical trial of breast cancer imaging using SSI in 2008. The trial showed the capability of the SSI technique to sharply discriminate between benign and malignant lesions in a limited number of patients *(N=15)*. In 2012, Berg *et al.*[49] showed in a multi-centric clinical study involving a very large cohort of a 939 patients, that the SSI technique offers a very high specificity level which could help improve the ultrasonographic assessment of breast masses. Fig 1.18 presents B-mode images and their corresponding shear wave elastography images (acquired by using the SSI technique) of three different human breast lesions. For the elastographic images, the colour-bar was fixed between 0 and 180 kPa, with black and red representing the lowest and highest elasticity values, respectively. In this case, the SSI measurement of elasticity correlated with the malignancy degree of a biopsy proven grade I infiltrating ductal carcinoma (a), a grade III invasive ductal carcinoma (b) and a fibroadenoma (c).

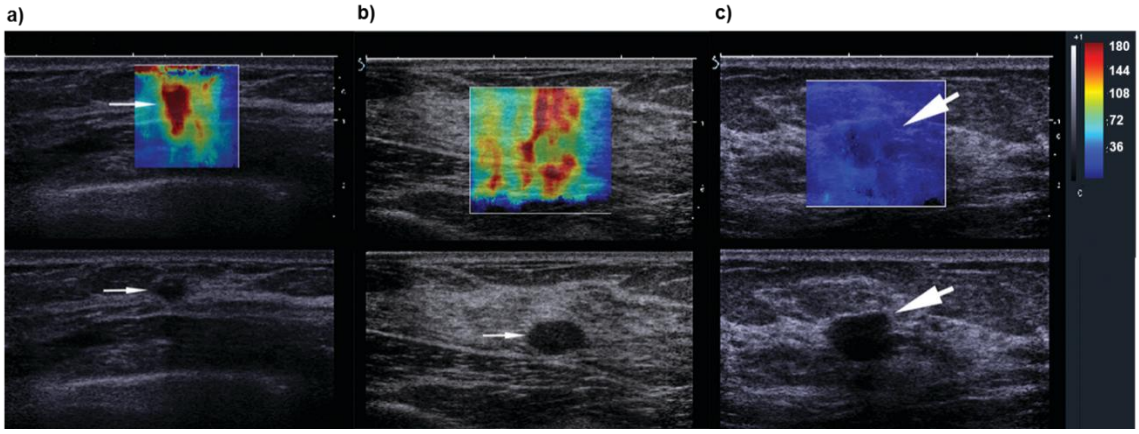

Fig 1.18. B-mode images(bottom) of three different breast lesions and their corresponding elastographic images (top)acquired by using the SSI technique. (a) A 6-mm irregular hypoechoic mass considered to be BI-RADS category 5 in a 58-year-old woman. Biopsy showed grade I infiltrating ductal carcinoma. (b) An oval, circumscribed mass considered to be BI-RADS category 3 in a 67-year-old woman. Shear wave (SW) elastographic image shows that the mass and surrounding tissue are heterogeneously stiff and that the zone of stiffness is irregular, all of which are suspicious findings on an SW elastographic image. Biopsy showed grade III invasive ductal carcinoma. (c) An oval, mostly circumscribed mass considered to be BI-RADS category 4a in a 35-year-old woman. SW elastographic image shows that the mass (arrow) was relatively homogeneously soft. On the basis of the benign appearance on SW elastographic image, this mass could have been considered BI-RADS category 3. Biopsy showed fibroadenoma [49].

Cosgrove [50] performed a study on 758 breast masses that were visible on ultrasound to evaluate the reproducibility of the SSI technique. Fig 1.19 shows the B-mode images (bottom) and their corresponding elastographic (top) images for one of the lesions. For the elastographic images, the colour-bar was fixed between 0 and 180 kPa, with black and red representing the lowest and highest elasticity values respectively. The colourless areas within the Q-boxes (white square) denote the regions with no detectable echo. In order to assess the intraobserver reproducibility (when one observer examines the same material more than once), each observer obtained three consecutive SWE images of 758 masses that were visible on ultrasound. 144 (19%) were malignant. For the interobserver reproducibility (when two or more observers examine the same material), a blinded observer reviewed images and agreement on elastographic features was determined. This clinical study showed that SWE is highly reproducible for assessing elastographic features of breast masses within and across observers. Moreover, it also showed that the SWE interpretation is at least as consistent as that of ultrasound B-mode features.

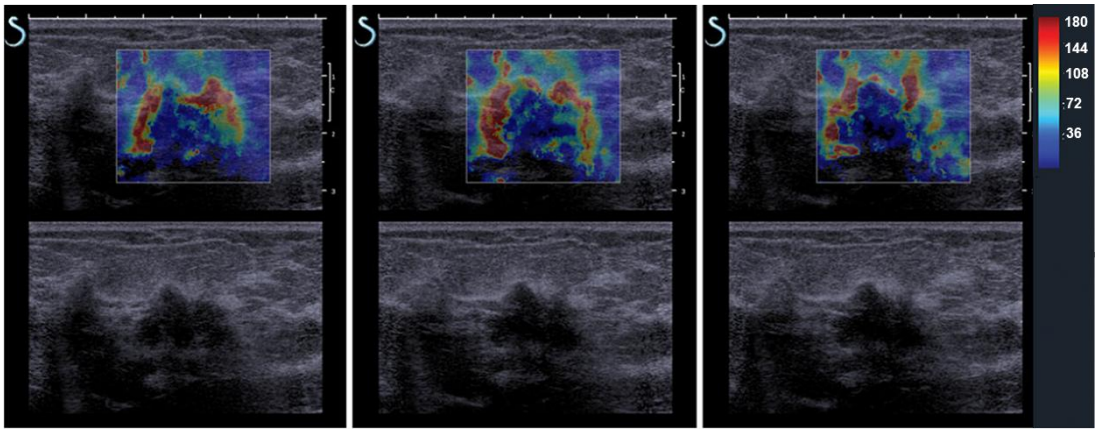

Fig 1.19. Three sequentially acquired B-mode images and the corresponding Shearwave Elastography images of a breast cancer showing the small changes registered over time. The acquisitions show a high repeatability. The colour-bar represent the lowest and highest elasticity values in black and red respectively [50].

The performed clinical studies proved that the SSI technique is a powerful tool for the detection and characterization of breast lesions with good specificity and reproducibility [49][50]. Nevertheless, there is room for improving the performance of the technique. For instance, it has not been yet proved if the technique can be used to monitor the development and medical treatment of cancer tumours *in vivo*. The question as to whether cancer tumour characterization can be enhanced with the use of 3D-SWE elastography is answered throughout this work.

Elastography imaging modalities present an added value with respect to other imaging modalities for medical diagnosis, which lies in the contrast observed in the tissue viscoelastic properties that correlate with significant changes in the stroma and connective tissues during disease processes.

In the last two decades, the use of elastography as a medical imaging technique has grown rapidly. New techniques have been developed; some of them with a great applicability as medical imaging tools. However, for some others, their cost, limited mobility and the lack of quantitative information limit their *in vivo* applicability. Therefore, it is important to have a good understanding of the advantages and limitations of each technique to better exploit them.

1.2 Conclusion

This work focuses on the application of SWE for the characterization and monitoring of cancerous tissues in human beings and mice. Chapter 2 contains the results of a clinical study on patients presenting different kinds of breast abnormalities. The study aimed to evaluate the feasibility of using 3D-SWE and 3D ultrasound to monitor tumour growth and tumour response to neo-adjuvant chemotherapy treatment. In this study, the tumour volumes measured by conventional ultrasound and MRI were correlated.

In Chapter 3, the results of an animal study are presented. In this case, the idea was to understand the pathology underlying stiffness. A representative type of human breast cancer

tumour was implanted in the flank of nude mice. The tumour volumes and their global elasticity values were measured by conventional ultrasound and 2D-SWE respectively before and after chemotherapy treatment. Histological analyses were performed to retrieve the percentages of cellularity, fibrosis and necrosis of the tumours.

Continuing with the monitoring of the cancer tumour behaviour pre and post treatment by the SSI technique, the results of a second animal study are presented in Chapter 4. This time, fragments of human colon-rectal tumour were ectopically and orthotopically implanted in mice. The tumour volumes and elasticity values pre and post treatment were measured by ultrasound and the SSI technique respectively. Unlike the study mentioned in Chapter 3, in this study the animals were treated with an antivascular drug to destroy the tumours vascular network and halt their development.

In Chapters 2 to 4, the elasticity is utilized as a biomarker for the tissue characterization. Nevertheless, there exist additional parameters such as elastic non-linearity, which could offer new and precious information on tissue characteristics. Chapter 5 presents the first known 2D-nonlinear elasticity maps of tissue mimicking phantoms and liver beef samples. Here, the third order non-linear parameter is retrieved for a wide range of elasticity values by using a developed technique, which employs a conventional ultrasonic probe and combines both the SSI technique and the Static Elastography concepts to retrieve elastic nonlinearity. Chapter 5 ends by presenting the result of a study performed *ex vivo* on mice colon samples, in which the technique used to retrieve the non-linear parameter is employed to understand the mechano-transduction processes involved in tumour development in biological tissues. The colon samples were taken from genetically and non-genetically modified mice. Some of the genetically modified mice had developed cancer tumours in the colon. The goal of the experiments was to calculate the amount of intracellular stress needed to trigger the development of cancerous tumours in mouse tissue. The stress was calculated by combining quasi-static compressions with the SSI technique through Hooke's law.

References

[1] C. Elsberg. "The Edwin smith surgical papyrus and the diagnosis and treatment of injuries to the skull and spine 5000 years ago". *Ann. Med. Hint.*, 8 pp. 271-279, 1981.
[2] R. J. Dickinson, C. R. Hill. "Measurement of soft tissue motion using correlation between A-Scans", *Ultr. Med. & Bio.*, 8, No. 3, pp. 263-271, 1982.
[3] A. Eisenscher, E. Schweg-Toffler, G. Pelletier, P. Jacquemard. "La palpation échographique rythmée: Echosismographie. Une nouvelle technique de différentiation des tumeurs bénignes et malignes par l'étude ultrasonore de l'élasticité tissulaire", *J. Radiol.*, 64, No. 4, pp. 255-261, 1983.
[4] J.L. Gennisson. "Le palpeur acoustique: un nouvel outil d'investigation des tissus biologiques", Thèse de Doctorat de l'Université Paris 6 – Pierre et Marie Curie, Septembre (2003).
[5] J. Ophir, I. Cespedes, H. Ponnekanti, Y. Yazdi, X. Li. "Elastography: a quantitative method for imaging the elasticity of biological tissues". *Ultrasonic Imaging*, 13, pp. 111-134, 1991.
[6] Itoh A, Ueno E, Toho E et al. "Breast Disease: Clinical Application of US Elastography for Diagnosis". *Radiology*, 239(2): 341-350, 2006.

[7] A. Tardivon, C. El Khoury, F. Thibault, A. Wyler, B. Barreau and S. Neuenschwander. "Elastography of the breast: a prospective study of 122 lesions". *Journal of Radiology*, vol. 88, (5) Pt 1, pp. 657-62, 2007.
[8] R. M. Lerner, K. J. Parker, J. Holen, R. Gramiak, R.C. Waag. "Sono-elasticity: Medical elasticity images derived from ultrasound signals is mechanically vibrated targets", *Acoustical Imaging*, L. J. Kessler, Ed. New York: Kluwer Academic, vol. 16, pp. 317-327, 1998.
[9] M. Fatemi, J. F. Greenleaf. "Ultrasound-Stimulated vibro-acoustic spectrography". *Science*, vol. 280, pp. 82-85 1998.
[10] L. Sandrin, B. Fourquet, J.M. Hasquenoph, S. Yon., C. Fournier, F. Mal, C. Christidis, M. Ziol, B. Poulet, F. Kazemi, M. Beaugrand, R. Palau, "Transient elastography: a new non-invasive method for assessment of hepatic fibrosis*", Ultr. Med. & Bio*. 29, pp. 1705–1713, 2003.
[11] K. R. Nightingale, M. S. Soo, R. W. Nightingale, G. E. Trahey, "Acoustic radiation force impulse imaging: In vivo demonstration of clinical feasibility", *Ultrasound in Med. & Biol.*, 28 (2), pp. 227-235, 2002.
[12] J. Bercoff, M. Tanter, M. Fink. "Supersonic Shear Imaging: A new technique for soft tissue elasticity mapping". *IEEE Trans. Ultra., Ferro. Freq. Ctrl.*, 51(4), pp. 396-409, 2004.
[13] T. A. Krouskop , B. S. Dougherty, F. S, and F. S. Vinson. "A pulsed Doppler ultrasonic system for making noninvasive measurements of the mechanical properties of soft tissue", *J. Rehabil. Res. Dev.*, 24, pp. 1-8, 1987.
[14] S. R. Huang, R. M. Lerner, K, and J. Parker. "Time domain Doppler estimators of the amplitude of vibrating targets", *J. Acoust. Soc. Am*, 91 (2), pp. 965-974, 1992.
[15] K. J. Parker, and R. M. Lerner. "Sonoelasticity of organs: Shear waves ring a bell", *J. Ultrasound Med.*, 11, pp. 387-392, 1992.
[16] K. J. Parker, M.M. Doyley and D.J. Rubens. "Imaging the elastic properties of tissue: the 20 year perspective". *Phys. Med. Biol*. 56, R1–R29 (2011).
[17] Y. Yamakoshi, M. Suzuki, and T. Sato. "Imaging the elastic properties using low frequency vibration and proving ultrasound wave", *Japanese meeting of applied physics, Tokyo, 1987*.
[18] Y. Yamakoshi, J. Sato, and T. Sato. "Ultrasonic imaging of internal vibration of soft tissue under forced vibration", *IEEE Trans. Ultra., Ferro. Freq. Ctrl.*, 37(2), pp. 45-53, 1990.
[19] L. M. Brekhovskikh, and V. Goncharov. "Mechanics of continua and wave dynamics", *Ed. Springer-Verlag*, 1993.
[20] S. F. Levinson, M. Shinagawa, and T, Sato. "Sonoelastic determination of human skeletal muscle elasticity", *J. Biomech*., 28, No. 10, pp. 1145-1154, 1995.
[21] K. Fujii, T. Sato, K. Kameyama, T. Inoue, K. Yokoyama, and K. Kobayashi. "Imaging system of precise hardness distribution in soft tissue in vivo using forced vibration and ultrasonic detection", *Acoust. Imaging Proceedings*, Plenum, 21, pp. 253-258, 1994.
[22] V. Dutt, R. R. Kinnick, and J. F. Greenleaf. "Acoustic shear wave displacement measurement using ultrasound", *IEEE Ultrasonics symposium*, 2, pp. 1185-1188, 1996.
[23] L. S. Taylor, D. J. Rubens, B. C. Porter *et al*.. "Prostate Cancer: Three-dimensional Sonoelastography for in Vitro Detection", *Radiology*, vol. 237, no. 3, pp. 981-985, 2005.
[24] R. Muthupillai, D. J. Lomas, P. J. Rossman, J. F. Greenleaf, A. Manduca, R. L. Ehman. "Magnetic resonance elastography by direct visualization of propagating acoustic strain waves". *Science*, vol. 269, pp. 1854-57 (1995).
[25] R. Sinkus, J. Lorenzen, D. Schrader et al. "High resolution tensor MR-elastography for breast tumor detection". *Phys. Med. Biol*, 45, pp. 1649-60 (2000).
[26] T. E. Oliphant, A. Manduca, R. L. Ehman, J. Greenleaf. "Complex-valued stiffness reconstruction for magnetic resonance elastography by algebraic inversion of the differential equation", *Magnetic Res. Med*., 45, pp. 299-301 (2001).
[27] D. B. Plewes, J. Bishopo, A. Samani, J. Sciarretta. "Visualization and quantification of breast cancer biomechanical properties with magnetic resonance elastography", *Phys. Med. Biol*, 45, pp. 1591 (2000).
[28] M. A. Dresner, G. H. Rose, P. J. Rossman, R. Muthupillai, A. Manduca, R. L. Ehman. "Magnetic resonance elastography of skeletal muscle", *J. Mag. Res. Imaging*, 13, pp. 269-276 (2001).
[29] S. Catheline. "Interférometrie-speckle ultrasonore: application à la mesure d'elasticité", *Thèse de Doctorat de l'Université Paris 7 – Denis Diderot*, (1998).
[30] S. Catheline, J. Thomas, F. Wu, and M. Fink. "Diffraction field of a low frequency vibrator in soft tissues using transient elastography", *IEEE Trans. Ultra., Ferro. Freq. Ctrl.*, 46(4), pp. 1013-1019, 1999.
[31] T. Deffieux. "Palpation par force de radiation ultrasonore et échographie ultrarapide: Applications à la caractérisation tissulaire in vivo". *Thèse de Doctorat de l'Université Paris 7 – Denis Diderot*, Décembre (2008).
[32] W. Walker, B. Friemel, L. Bohs, and G. Trahey. "Real-time imaging of tissue vibration using a two-dimensional speckle tracking system", *Ultrasonics symposium*, vol. 2, pp. 873-877, 1993.
[33] J. Bercoff, S. Chaffai, M. Tanter, L. Sandrin , S. Catheline , M. Fink ,J. L. Gennisson and M. Meunier. "*in vivo* breast tumor detection using transient elastography". *Ultrasound in Med. & Biol.*, Vol. 29, No. 10, pp. 1387–1396, 2003.
[34] G. R. Torr. "The acoustic radiation force", *Am.J.Phys*. 52, 402–8 (1984).
[35] T. Sugimoto, S. Ueha and K. Itoh. "Tissue hardness measurement using the radiation force of focused ultrasound". *Proc. IEEE Ultrason. Symp*. pp1377–80 (1990).
[36] M. Fatemi and J. Greenleaf. " Ultrasound-simulated vibro-acoustic spectrography". *Science*, vol. 280, no. 5360, pp. 82-85, 1998.
[37] M. Fatemi, L. E. Wold, A. Alizad, and J. F. Greenleaf. "Vibro-Acoustic Tissue Mammography", IEEE Transactions on Medical Imaging, vol. 21, pp. 1-8, no. 1 (2002).
[38] A. Alizad, D. H. Whaley, J. F. Greenleaf and M. Fatemi. "Image Features in Medical Vibro-acoustography: In Vitro and in Vivo Results", *Ultrasonics*, 48(6-7):559-562 (2008).
[39] S. Chen, M. Fatemi, and J. Greenleaf. "Quantifying elasticity and viscosity from measurement of shear wave speed dispersion", *The Journal of the Acoustical Society of America*, vol. 115, no. 6, pp. 2781-2785, 2004.
[40] K. Nightingale, M. Palmeri and R. Nightingale. " On the feasibility of remote palpation using acoustic radiation force", *The Journal of the Acoustical Society of America*, vol. 110, no. 1, pp. 625-634, 2001.
[41] K. Nightingale, R. Bentley, and G. Trahey. "Observations of tissue response to acoustic radiation force: opportunities for imaging", *Ultrasonic Imaging*, vol. 24, no. 3, pp. 129-138 (2002).
[42] B. Fahey, M. Palmeri, and G. Trahey, "Frame rate considerations for real-time abdominal acoustic radiation force impulse imaging", *Ultrasonic Imaging*, vol. 28, no. 4, pp. 193-210 (2006).

[43] K. Nightingale, S. McAleavey, and G. Trahey, "Shear-wave generation using acoustic radiation force: *in vivo* and *ex vivo* results", ". *Ultrasound in Med. & Biol.*, vol. 29, No. 12, pp. 1715–23, 2003.
[44] M. Palmeri, M. H. Wang, J. J. Dahl, K. D. Frinkley, and K. Nightingale. "Quantifying hepatic shear modulus in vivo using acoustic radiation force", ". *Ultrasound in Med. & Biol.*, vol. 34, No. 4, pp. 546–558, 2008.
[45] M. L. Palmeri, K. R. Nightingale. "Acoustic radiation force-based elasticity imaging methods". *Interface Focus*, (1), 553-564 (2011).
[46] A. Sarvazyan, O. Rudenko, S. Swanson, and J. Fowlkes. "Shear wave elasticity imaging: a new ultrasonic technology for medical diagnostics", ". *Ultrasound in Med. & Biol.*, vol. 24, No. 9, pp. 1419–1435, 1998.
[47] J. Bercoff. "L'imagerie échographique ultrarapide et son application à l'étude de la viscoélasticité du corps humain ". *Thèse de Doctorat de l'école supérieure de Physique et de Chimie Industrielle*, 2004.
[48] M. Tanter, J. Bercoff, A. Athanasiou, T. Deffieux, J. L. Gennisson, G. Montaldo, M. Muller, A. Tardivon, and M. Fink, "Quantitative assessment of breast lesion viscoelasticity: Initial clinical results using supersonic shear imaging", *Ultrasound in Med. & Biol.*, vol. 34, No. 9, pp. 1373–1386, 2008.
[49] W. A Berg, D. O. Cosgrove, C. J. Doré et al.. "Shear-wave Elastography Improves the Specificity of Breast US: The BE1 Multinational Study of 939 Masses", *Radiology*, 262(2): 435-449. 2012.
[50] D. O. Cosgrove, W. A Berg, C. J. Doré et al.. "Shear wave elastography for breast masses is highly reproducible". *Eur Radiol*, Dec 31, 2011.

2. Chapter 2. Monitoring Chemotherapy treatment by using 3D-Shear Wave Elastography (3D-SWE)

2.1 Introduction

Breast cancer is the most commonly diagnosed cancer and the leading cause of women death worldwide, accounting for 23% of the total number of new cases and 14% of deaths in 2008 [1][2].

Imaging plays a key role in the early detection of cancer abnormalities. Screening is based on mammography and B-mode Ultrasound (US). The discrimination of breast abnormalities between benign or malignant with ultrasound imaging is purely based on morphological criteria (e.g. mass margins, shape and orientation), which is defined in the BI-RADS lexicon (Breast Imaging Reporting And Data System) of the ACR (American College of Radiology) [3]**.** However, some cancers, including high pathological grade carcinoma may exhibit morphological features similar to benign lesions in 15 to 18% of the cases, while some seemingly 'suspicious' lesions may actually be benign [4]-[6]. Hence, morphological criteria are not always sufficient to fully characterize lesions.

Over the last two decades, researchers and industry have been trying to develop novel imaging techniques to measure new parameters which could help improve the characterization of breast lesions. Among the methods developed, there exist the Shear Wave Elastography (SWE) family, which groups those techniques that study the displacement of generated shear waves to quantify the medium elasticity. Amid the SWE family, we have the Supersonic Shear Wave Imaging (SSI technique), which has become increasingly popular as a complementary imaging tool to conventional US for the diagnosis of breast cancer abnormalities *in vivo* on humans [7]-[9]. Recent studies have shown that the SSI technique could improve the specificity of breast ultrasound up to 78.5% without loss of sensitivity [7], whereas it could be fairly reproducible in at least 87.9% of the 758 studied cases [8]. The technique has also shown that malignant lesions have much Young's modulus values than benign ones [9]. These new findings along with the classical morphological criteria seem to help improve breast lesion ultrasound characterization as shown by some recent studies [10]-[12]. Due to the proven efficacy of SWE, some approaches have been made to develop 3D-quasi-static elastographic methods [13][14]. Although they constituted interesting approaches to 3D-Elastography, these quasi-static elastographic systems offered only qualitative information and lacked robustness as some of the planes were dominated by strain estimation errors.

In this chapter, the concept of 3D-Shear Wave Elastography (3D-SWE) is introduced. It combines the multi-planar imaging benefits of 3D-US with the quantitative elasticity mapping of the SSI technique. Compared to 2D-US, 3D-US offers more information, *i.e.* the additional coronal view due to the real-time multi-planar lesion view. This additional plane permits a better evaluation of lesion features such as shape, margins and orientation. Lesion dimensions can be measured in three planes and the volume estimated. 3D-SWE has the advantage of offering detailed elasticity distribution in three dimensions. All the previously mentioned features would be particularly useful to evaluate lesion response to pre-operative anti-cancerous treatment.

This chapter presents the results of a clinical study aiming to evaluate the feasibility of using 3D-SWE in the monitoring of patients undergoing a type of chemotherapy which is intended to shrink the tumour before performing surgery (neo-adjuvant chemotherapy). This sort of treatment is usually for patients who desire to avoid mastectomy (surgical removal of the entire breast). Tumour volumes were measured with 3D-US and compared to MRI measurements. Tumour elasticity was measured with 3D-SWE.

2.2 Materials and Methods

2.2.1 Clinical protocol

This study was approved by the local research and ethics committee (CPP 2010-07-01) and written consent was obtained from all patients. Between December 2010 and January 2012, thirty-three patients (mean age of 51 ± 5 years [range 32 to 61] and mean lesion diameter of 32 ± 5 mm [range 22 to 48 mm] presenting with suspicious breast lesions were included. Characterization of breast lesions was performed using the Breast Imaging Reporting and Data System (BI-RADS) [16]. Lesions were classified as BIRADS 4 and BIRADS 5 . Biopsy was performed in all cases.

The study was subdivided into two protocols: Protocol I and Protocol II. In Protocol I, the tumour volumes of twenty-three patients were measured by using MRI and 3D-US imaging before the patients begun any kind of anti-cancerous therapy. The aim was to correlate the volumes retrieved with both techniques. In Protocol II, ten patients (which were not part of Protocol I) presenting with breast tumours were monitored periodically as they underwent neo-adjuvant chemotherapy treatment. The tumour volumes and elasticity were measured by 3D-US and 3D-SWE respectively. The 3D-US, 3D-SWE and MRI acquisitions were performed and interpreted by two experienced breast radiologists from the Radiology department at the *Institut Curie (Paris, France)*. 3D-US and 3D-SWE images were acquired by using the *Aixplorer ultrasound system (SuperSonic Imagine, Aix en Provence, France*).

2.2.2 3D-Ultrasound (3D-US)

A 2D probe (*SuperLinearTM Volumetric (SLV 16-5) - Supersonic Imagine*) designed for 3D imaging was implemented into the *Aixplorer* system to be able to perform 3D-US acquisitions. This probe is composed by a 1D linear array of 192 elements with a central frequency of 8 MHz. The linear array is displaced in fixed angular intervals by means of a small mechanical motor that sweeps the entire region of interest in about 5 s (Fig 2.1). However, the acquisition time varys depending on the image depth. At each probe position, 2D images are acquired. The 3D ultrasound volume of the lesion is then reconstructed from the acquired 2D image dataset. The system allows multi-planar navigation within the lesion in three different imaging planes: axial (z-axis), sagittal (y-axis) and coronal (x-axis) as presented in Fig 2.2 to Fig 2.4. This feature permits better and more accurate lesion visualization.

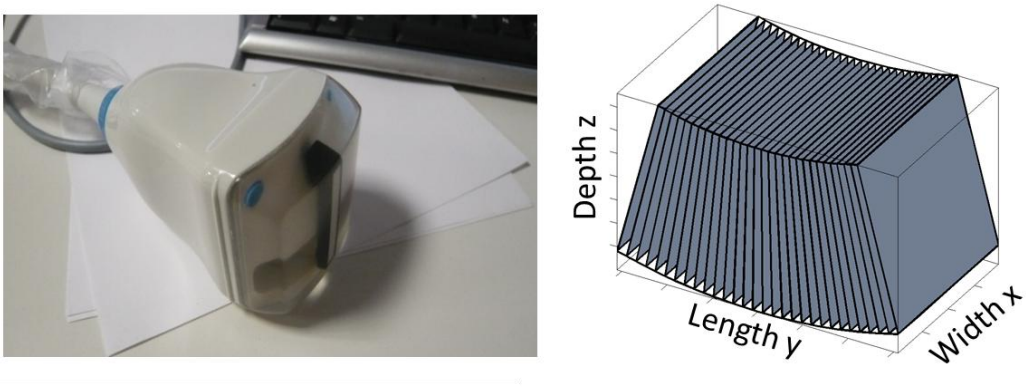

Fig 2.1. (a) Probe used for 3D-US and 3D SWE.; (b) The probe sweeps along the lesion, acquiring 2D images at each angular position which are then used to reconstruct and display a 3D volume.

Imaging settings such as image depth, focal position, contrast and resolution, can be adjusted before performing a 3D acquisition depending on the patient morpho-type and lesion localization inside the breast. A 3D-US sequence proceeded as follows:

The 3D probe was positioned along the tumour's central-axial plane before launching the image acquisition. Several acquisitions were performed at each probe position. Before each acquisition, the probe was removed and repositioned in order to test the robustness of the technique. Once the 3D sequence had been launched, the probe remained still until the acquisition had finished and the entire tumour had been covered. The complete volume was then displayed in three-orthogonal slice planes (axial, sagittal and coronal), along with a texture-mapped 3D rendering which showed the 3D relative position of each plane (Fig 2.2). The tumour's maximal diameters were measured in the central axial, sagittal and coronal planes of each 3D-US acquisition. To facilitate the volume calculations, the lesions were assumed to have an ellipsoidal shape. Therefore, tumour volumes were calculated by introducing the measured maximal diameters into the mathematical expression for the volume

of an ellipsoid presented in (1), in which d_a, d_s and d_c represent the tumour maximal diameters measured in the axial, sagittal and coronal planes respectively.

$$V = \frac{\pi . d_a . d_s . d_c}{6} \qquad \text{Eq. 1}$$

2.2.3 3D-Shear Wave Ultrasound Elastography (3D-SWE)

3D-SWE acquisitions were performed using the same 3D probe by simply switching on the Shear Wave imaging mode. In this mode, the Supersonic Shear Wave Imaging (SSI) technique presented in the last chapter, uses the shear wave propagation to remotely displace tissue in real time at each imaging plane. 2D quantitative elasticity maps are obtain at each angular position as the entire tumour is swept by the probe as in the 3D-US acquisitions. The 3D elasticity volume is then reconstructed from the acquired 2D images. The probe was then rotated 90° and placed in the central-sagittal plane of the tumour. As for the 3D-US acquisitions, 3D-SWE acquisitions were again performed along the central-axial and central-sagittal plane. Each pixel within the 3D elastic volume is quantified in kiloPascals (kPa) and colour-coded from black (softer) to red (harder). In this study, the colour-bar was fixed between 0 kPa and 180 kPa for all the patients. A complete 3D-SWE acquisition takes approximately 25s. Nevertheless, the acquisition time varies depending of the imaged depth. At the end of the acquisition, three orthogonal planes (axial, sagittal ad coronal) are displayed together with a texture-mapped 3D rendering (see Fig 2.8(b), Fig 2.9(b) and Fig 2.10(b)). Hence, the system offers precious quantitative information on the tissue stiffness at every single voxel within the 3D elastic volume. The tumour elasticity was retrieved by calculating the mean elasticity value within a circular region covering the largest possible tumour area. As said in the previous chapter, the spatial resolution of the elasticity maps obtained with this technique at 8 MHz is 1.2 mm.

2.2.4 Magnetic Resonance Imaging (MRI)

Breast MRI protocols were standardized according to the EUSOMA (European Society of Breast Cancer Specialists) and EUSOBI (European Society of Breast Imaging) recommendations [17,18] and comprised a bilateral examination including morphologic sequences (T1 or T2 with or without fat saturation) and dynamic sequences after intravenous injection of gadolinium. Subtraction and maximum intensity projections (MIP) were performed in post-processing. MIP is a volume rendering method for 3D data, which projects in the visualization plane the voxels with maximum intensity that fall in the way of parallel rays traced from the viewpoint to the plane of projection. This implies that two MIP renderings from opposite viewpoints are symmetrical images if they are rendered using

orthographic projection. Lesion volume was calculated on MRI by using the appropriate segmentation tools of the *Volume Viewer* software available in the work station. The MRI system (1.5 Tesla Siemens Symphony - TIM Magnet) has an in-plane spatial resolution of 0.8 mm x 0.8 mm.

2.2.5 Statistical analysis.

A statistical Bland-Altman plot and Box-plot were employed to analyse the agreement between the calculated 3D-US and MRI volumes.

The Bland-Altman plot compared pairwise the mean values of the volume measurements performed with US and MRI. In this method, the difference between the volumes was plotted against the average. The test gave as a results the bias, or the average of the differences. The bias was computed as the volume determined by MRI minus the volume determined by 3D-US. Ideally, the bias should be very close to zero. If it is not the case, this indicates that the two measurement methods are producing different results. The confidence interval was set to 95%, which means that in future volume measurements using 3D-US and MRI, the difference between both techniques should lie within the confidence interval approximately 95% of the time.

The Box-plot gave three statistical measures: the median, the upper and lower quartiles, and the minimum and maximum data values. Each box within the plot contained the middle 50% of the data. The box's upper and lower edges illustrated the 75^{th} and 25^{th} percentile of the dataset. The horizontal line within the box indicated the median dataset value. Ideally, the median line should be equidistant from the upper and lower edges, otherwise the data distribution (which was assumed non-Gaussian for this study) is distorted. The ends of the vertical lines depicted the maximum and minimum data values.

2.3 Results

2.3.1 Protocol I

Fig 2.2, Fig 2.3 and Fig 2.4 present the 3D-US multi-planar views of a *carcinoma* (1.20 cm^3) present in Patient 15, a *fibroadenoma* (2.06 cm^3) present in Patient 02 and a *carcinoma* present in Patient 08 (6.31 cm^3), respectively. The central axial (A), sagittal (T) and coronal (C) planes of the lesions are also depicted. The centre of the volume is represented by the yellow line overdraw on top of the volumetric view. The system allows navigation in any plane. The lesion morphology can be clearly distinguished from the surrounding tissue.

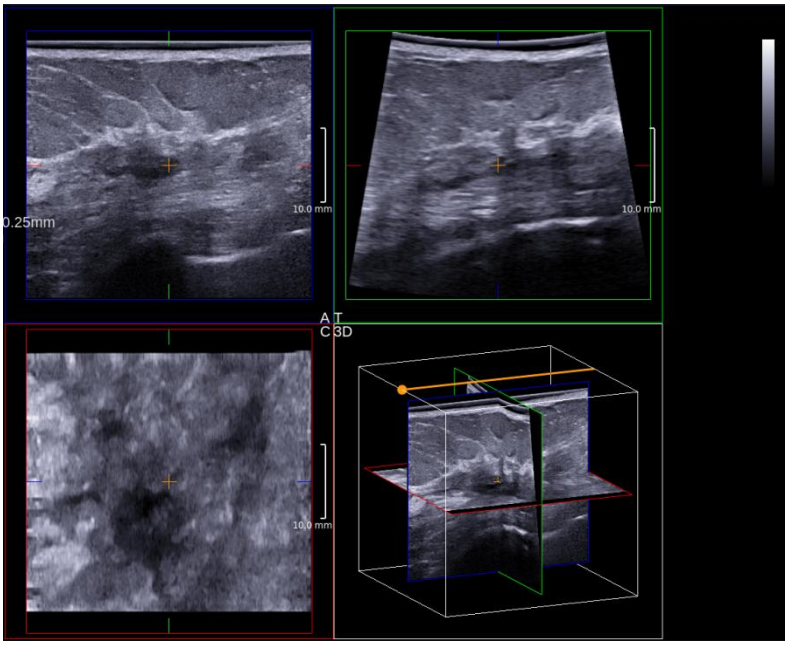

Fig 2.2. 3D-US multi-planar view of the carcinoma present in Patient 15 (Protocol I). (Upper-left corner) Axial plane (A); (Upper-right corner) Transversal plane (T); (Lower-left corner) Coronal plane (C). The lesion volume estimated from the 3D-US images was 1.20 cm^3.

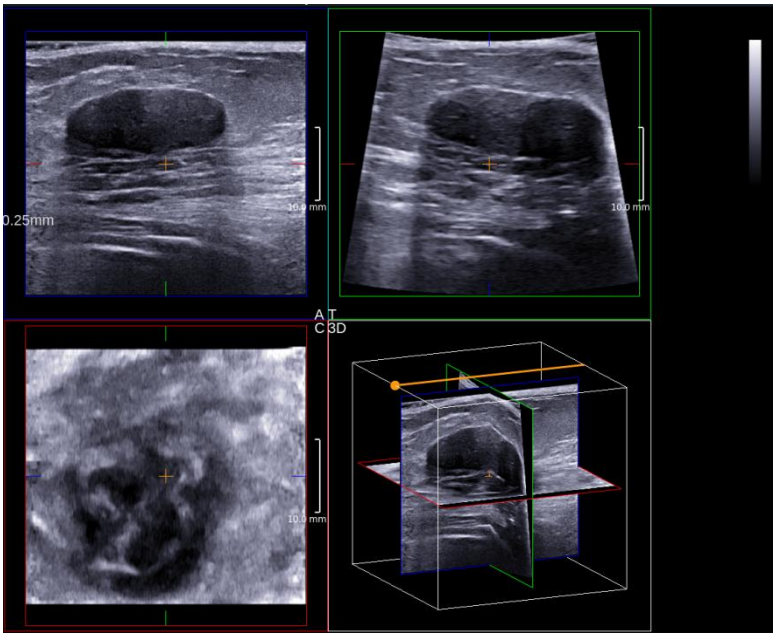

Fig 2.3. 3D-US multi-planar view of a fibroadenoma present in Patient 02 (Protocol I). (Upper-left corner) Axial plane (A); (Upper-right corner) Transversal plane (T); (Lower-left corner) Coronal plane (C). The lesion volume estimated from the 3D-US images was 2.06 cm^3.

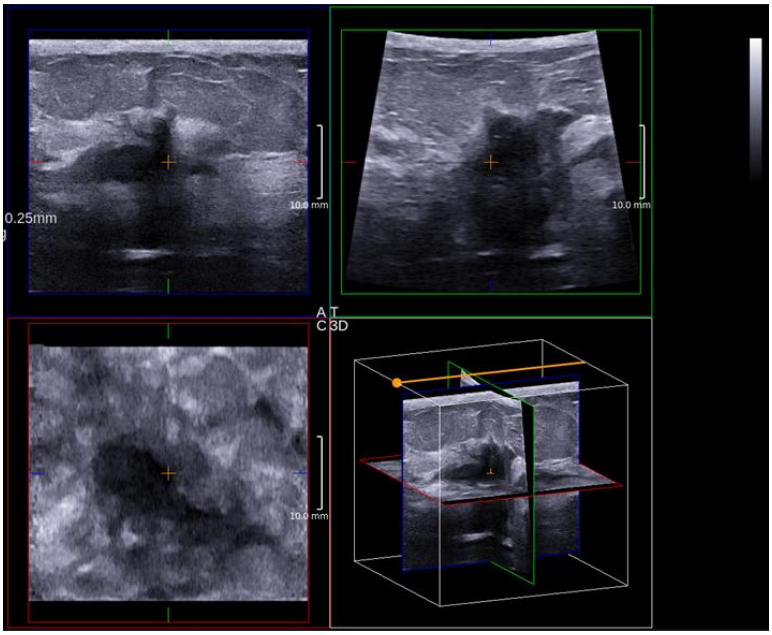

Fig 2.4. 3D-US multi-planar view of the carcinoma present in Patient 08 (Protocol I). (Upper-left corner) Axial plane (A); (Upper-right corner) Transversal plane (T); (Lower-left corner) Coronal plane (C). The lesion volume estimated from the 3D-US images was 6.31cm^3.

Fig 2.5 presents MRI images of the *fibroadenoma* present in Patient 02 (a) and a *carcinoma* present in Patient 15 (b). The tumour volumes estimated by MRI were 3.90 cm^3 and 6.34 cm^3, respectively.

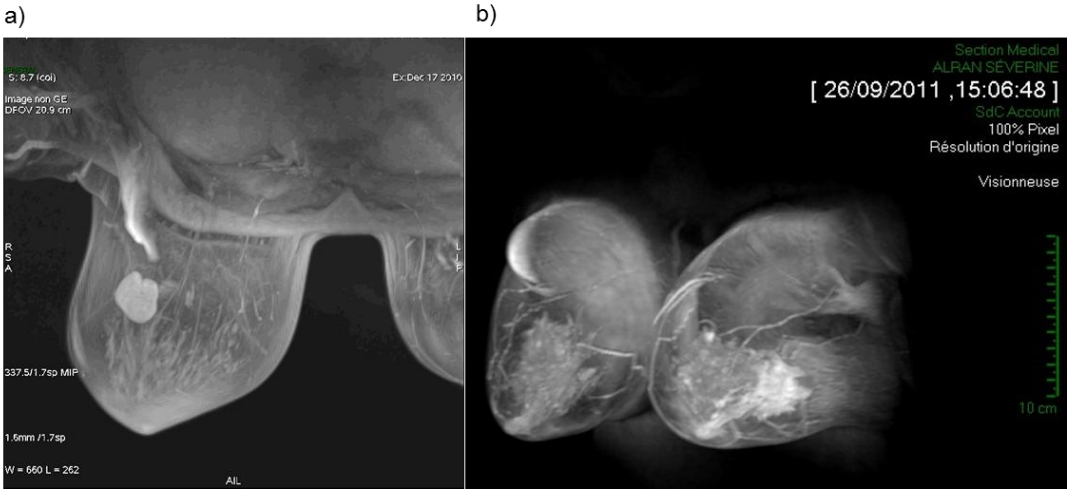

Fig 2.5. (a) MRI image of the benign lesion (fibroadenoma) present in Patient 02. The tumour volume calculated by MRI was 3.90 cm^3; (b) Carcinoma present in Patient 15. The tumour volume calculated by MRI was 6.34 cm.^{3}

Table 2.1 and Fig 2.6 present the estimated 3D-US and MRI volumes for the twenty-three patients who took part in the Protocol I. No error bars are displayed on the graphs since the 3D-US and the MRI volumes were estimated once by only one operator. The calculated MRI volumes of all the patients (except for Patient 09) were higher than the 3D-US volumes. There was a good agreement between the volumes calculated with both imaging techniques.

Table 2.1. Monitoring of Protocol I patients. The volumes of twenty-three patients presenting different breast tumours were retrieved by using MRI and 3D-US imaging. In all cases (except for Patient 09), the MRI volume was higher than the 3D-US one.

	Vol. 3D US [cm^3]	*Vol. 3D MRI [cm^3]*
Patient 01	1.02	2.15
Patient 02	2.06	3.90
Patient 03	3.63	4.20
Patient 04	2.36	5.11
Patient 05	4.38	6.95
Patient 06	5.81	10.70
Patient 07	3.30	3.83
Patient 08	6.31	13.01
Patient 09	4.21	3.70
Patient 10	13.82	14.79
Patient 11	22.46	24.36
Patient 12	4.81	6.10
Patient 13	2.04	3.89
Patient 14	5.22	14.99
Patient 15	1.20	6.34
Patient 16	0.56	5.33
Patient 17	3.15	4.07
Patient 18	1.40	1.98
Patient 19	3.35	4.09
Patient 20	2.04	6.34
Patient 21	1.96	6.71
Patient 22	3.46	4.93
Patient 23	3.04	3.98

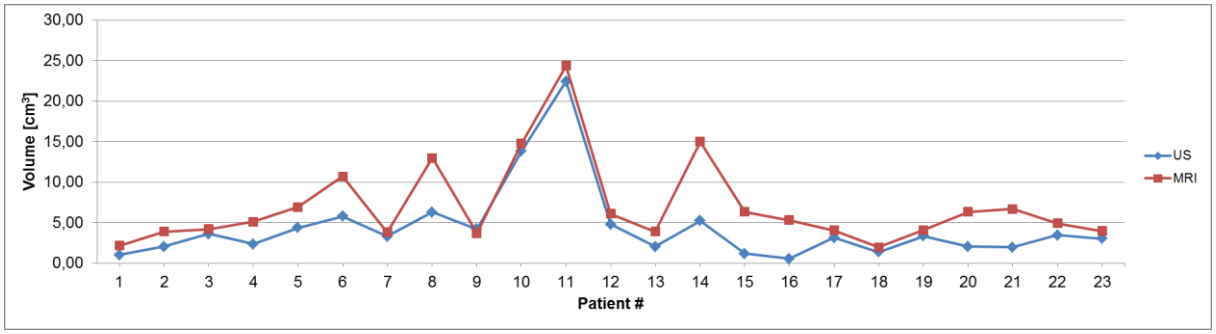

Fig 2.6. Tumour volume monitoring. The tumour volumes of the twenty-three patients who took part in Protocol I were measured with MRI and 3D-US. Both imaging techniques presented close volume measurements. In all the cases (except for Patient 09) , the MRI volumes were higher than the US ones. No error bars are displayed on the graphs since the 3D-US and the MRI volumes were estimated once by only one operator.

2.3.1.1 Statistical analysis

The difference between the 3D-US and MRI volumes (MRI-3D-US) was plotted against their ratio (MRI/3D-US) in a Bland-Altman plot Fig 2.7(a). The mean value of the differences between both data-sets (bias) was 2.60 cm^3 and the standard deviation 2.45 cm^3. The interval of confidence was set to 95% and laid between -2.21 cm^3 and 7.41 cm^3. Otherwise stated, in future measurements, the difference between the volumes measured with both imaging techniques should be within the same interval [-2.21,7.41] in 95% of the cases if they are correctly done.

Fig 2.7(b) contains a box-plot of both datasets. Both volumes presented a similar value interval, with the 3D-US and MRI volumes ranging from 0.56 cm^3 to 22.46 cm^3 and 1.98 cm^3

to 24.36 cm^3, respectively. The range within which 50% of the volumes were located with respect to the median value (often called interquartile range or IQR) went from 2.04 cm^3 to 4.81 cm^3 and 3.98 to 6.95 cm^3 for US and MRI respectively. Moreover, the MRI volumes had a mean value 0f 5.08 cm^3 and the 3D-US volumes one of 3.33 cm^3.

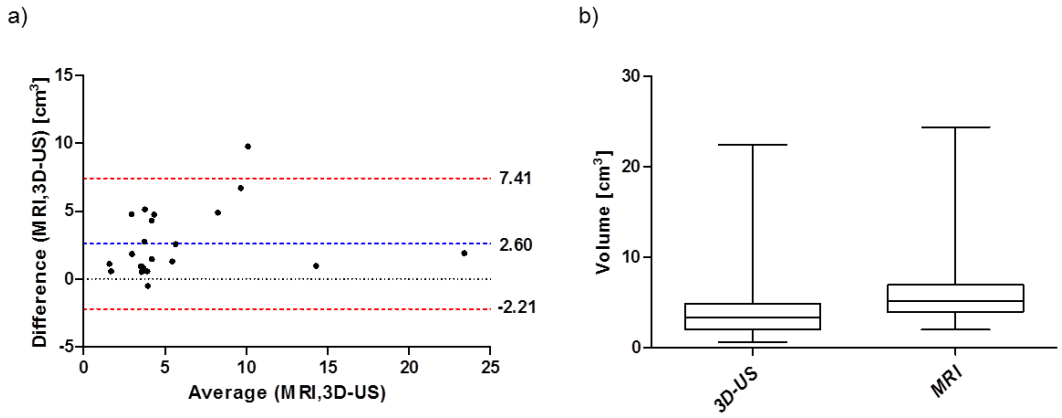

Fig 2.7. a) Bland-Altman plot of the volume difference (MRI -3D-US) versus the average (MRI/3D-US) of the two datasets. The dotted red lines and the blue line represent the 95% confidence interval and the bias respectively. The bias is the mean value of the differences between both datasets. b) Box-plot of the tumour volumes with each imaging technique. The boxes represent the interquartile range, within which 50% of the volumes are located with respect to the median value of each volume dataset.

2.3.2 Protocol II

2.3.2.1 Tumour volume

As done for Protocol I, tumour volumes were calculated at each session for the patients taking part in Protocol II. Fig 2.8(a) , Fig 2.9(a) and Fig 2.10(a) contain the 3D-US volumes and multi-planar views of the *carcinomas* present in Patients 07, 05 and 03 (Protocol II), respectively. The 3D-US lesion volumes were 3.01 cm^3, 2.05 cm^3 and 6.27 cm^3 for Patients 07, 05 and 03, respectively.

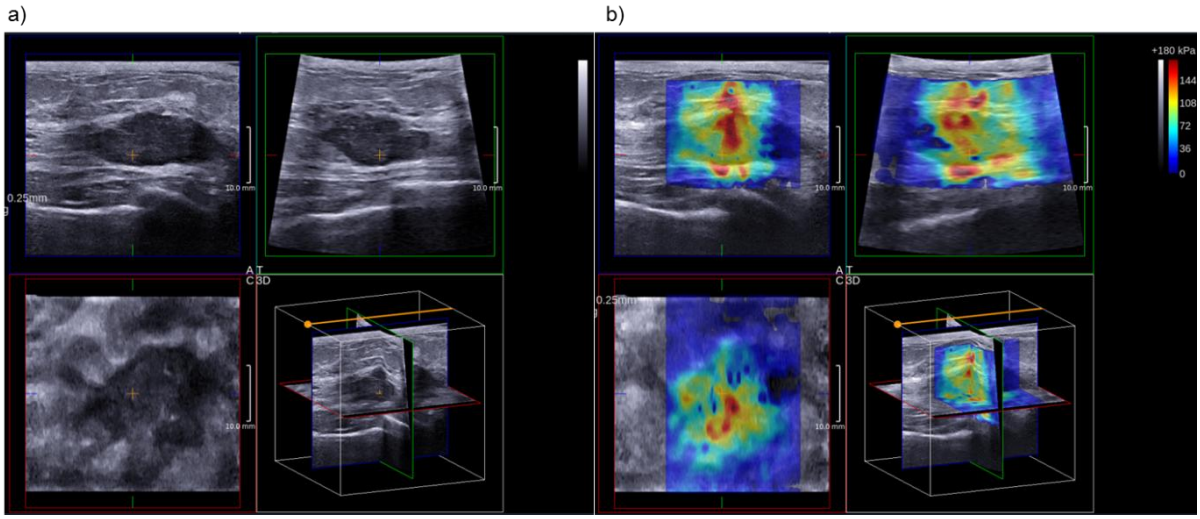

Fig 2.8. (a) 3D-US and (b) 3D-SWE multi-planar views of the carcinoma present in Patient 07- Protocol II. The tumour volume and Young's modulus measured 23 days after the beginning of the treatment were 3.01 cm^3 and 83.4 ± 20.7 kPa respectively.

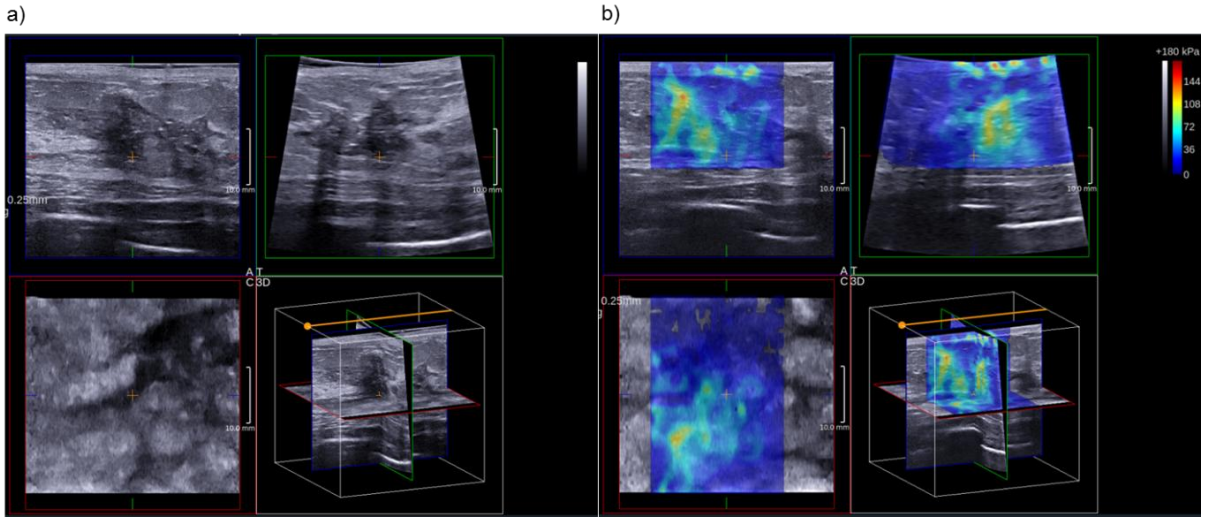

Fig 2.9. (a) 3D-US and (b) 3D-SWE multi-planar views of the carcinoma present in Patient 05-Protocol II. The tumour volume and Young's modulus measured 29 days after the beginning of the treatment were 2.05 cm^3 and 58.9 ± 26.6 kPa respectively.

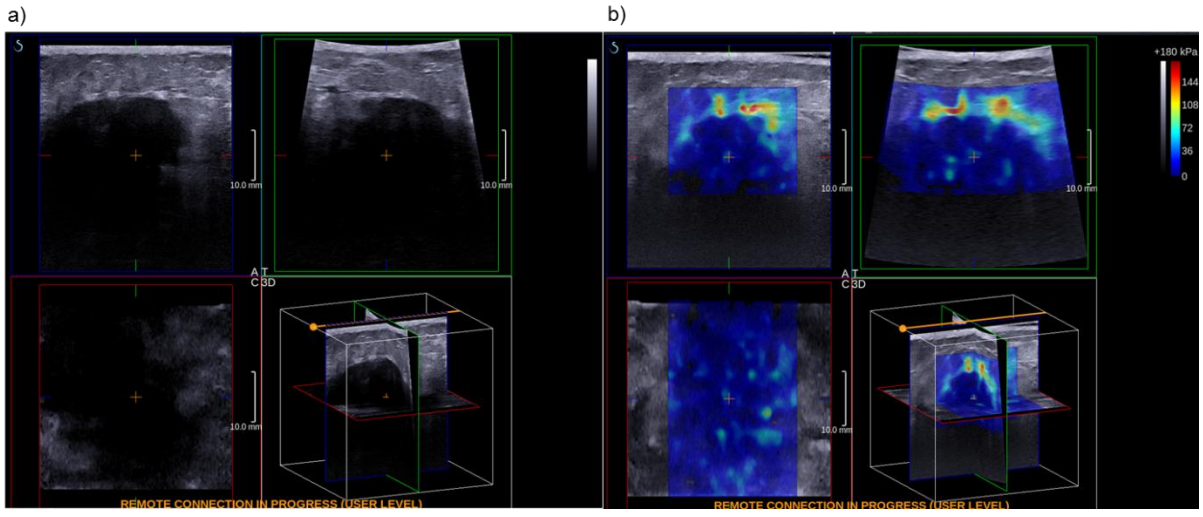

Fig 2.10. (a) 3D-US and (b) 3D-SWE multi-planar views of the "soft" carcinoma present in Patient 03- Protocol II. The tumour volume and Young's modulus measured at the very beginning of the treatment were 6.27 cm^3 and 13.4 ± 41.7 kPa respectively.

Table 2.2 and Fig 2.11 contain the 3D-US volumes for all the patients who took part in Protocol II. Every single point displayed on Fig 2.11 represents a measurement time point (M1 to M6) presented in Table 2.2. Throughout the protocol, the patients were monitored several times depending on their availability and health conditions. Four patients were monitored three times, four patients four times, one patient five times and one patient six times. One can appreciate that the tumour volumes sharply decreased during the chemotherapy treatment in almost all the patients. This drastic change in volume took place within the first forty days of treatment in most of the cases. Only Patient 05 and Patient 10 showed a volume increase between the second (M2) and the third (M3)measurement, after the volume had dramatically decreased between the first (M1) and the second (M2) measurement from 4.48 cm^3 to 2.05 cm^3 and 9.76 cm^3 and 2.37 cm^3 in Patient 05 and Patient 10 respectively.

Table 2.2. Monitoring tumour volume of Protocol II patients. The tumour volumes of ten patients (which did not take part in Protocol I) were estimated periodically with 3D-US as they underwent neo-adjuvant chemotherapy treatment. Not all the patients were necessarily monitored the same number of times. In other words, the number of measurements (M1 to M6) may vary from one patient to another.

	3D-US volume [cm^3]					
	M1	*M2*	*M3*	*M4*	*M5*	*M6*
Patient 01	2.05	1.81	0.58	1.23	--	--
Patient 02	4.84	0.54	0.40	0.29	--	--
Patient 03	6.27	0.74	0.36	0.07	--	--
Patient 04	1.40	0.59	0.44	--	--	--
Patient 05	4.48	2.05	2.81	--	--	--
Patient 06	2.39	0.38	0.19	0.60	--	--
Patient 07	8.51	3.01	1.84	0.84	0.80	0.83
Patient 08	4.30	2.03	2.13	0.37	0.59	
Patient 09	2.10	3.27	2.40			
Patient 10	9.76	2.37	3.85			

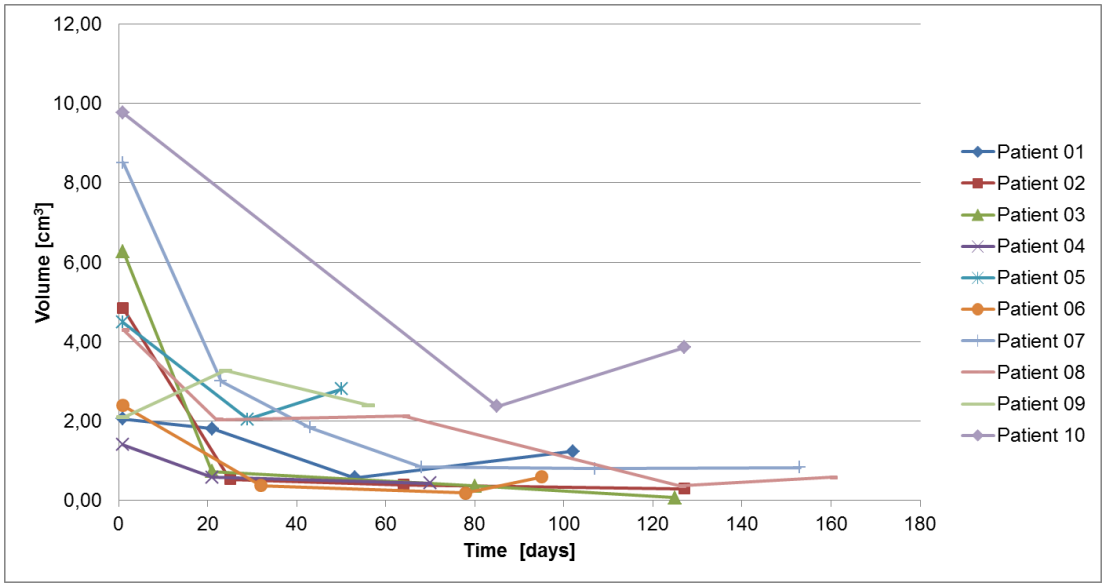

Fig 2.11. Tumour volume monitoring during chemotherapy treatment for the ten patients taking part in Protocol II. Each point within the graph represents a measurement time point (M1 to M6). One can appreciate from the graph that, overall, the tumour size decreased during the treatment.

Fig 2.12 depicts the volume evolution during the chemotherapy for the carcinoma present in Patient 07. The tumour volume decreased sharply, going from 8.51 cm^3 at the beginning of the treatment to 0.84 cm^3 in 68 days. The lesion volume remained quasi-constant during the subsequent days until the end of the patient's treatment.

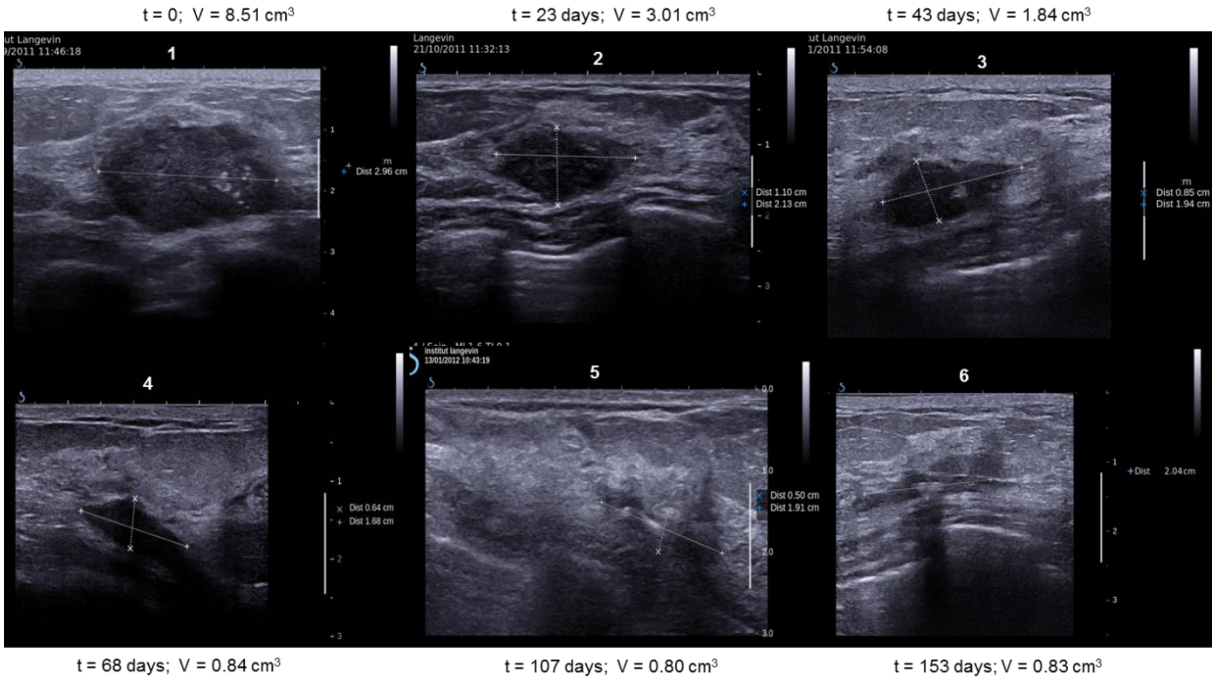

Fig 2.12. Tumour volume monitoring during chemotherapy. The volume of the carcinoma present in Patient 07 showed a remarkable decrease in size during the treatment. The tumour volume went from 8.51 cm^3 at the beginning of the treatment to 0.84 cm^3 in 68 days.

In order to corroborate the 3D-US volume measurements, MRI volume estimations were performed on the same patients at the beginning and the end of the chemotherapy treatment. Table 2.3 and Fig 2.13 present the MRI volumes. Patients 02, 09 and 10 did not

have a second MRI session since they underwent mastectomy (breast ablation). In most of the cases, the 3D-US and MRI acquisitions were not performed on the same day. Apart from Patients 01 and 06, the MRI volumes estimated in the final weeks of the chemotherapy were considerable smaller than the ones obtained when the treatment begun.

Table 2.3. Monitoring tumour volume of Protocol II patients with MRI. The tumour volumes of the ten patients taking part in the Protocol II, were estimated with MRI at the beginning (M1) and the end (M2) of the neo-adjuvant chemotherapy treatment. Patients 02, 09 and 10 do not have a second MRI session since they underwent mastectomy (breast ablation).

MRI volume [cm^3]		
	M1	*M2*
Patient 01	1.93	3.98
Patient 02	5.64	--
Patient 03	12.97	1.04
Patient 04	2.93	0.61
Patient 05	7.97	2.86
Patient 06	2.96	2.17
Patient 07	10.76	1.58
Patient 08	6.77	3.01
Patient 09	5.96	--
Patient 10	3.44	--

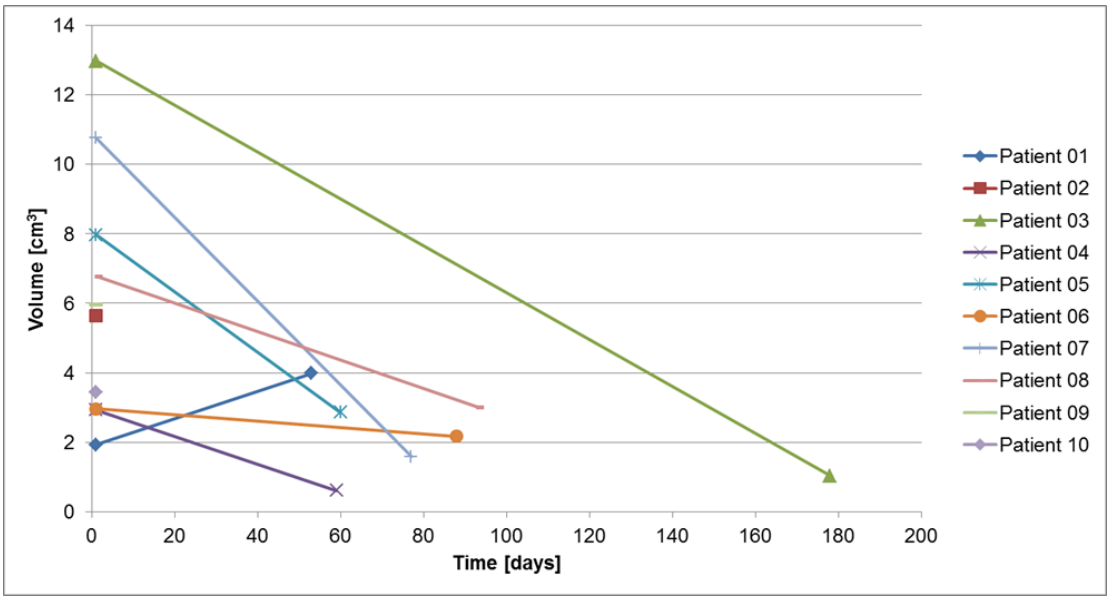

Fig 2.13. Tumour volume monitoring with MRI during chemotherapy treatment for the ten patients taking part in Protocol II. The MRI tumour volume estimations were performed at the beginning (M1) and the end (M2) of the chemotherapy for seven patients. For the other three patients of the protocol, the volume estimations were performed only at the beginning of the treatment since they underwent mastectomy. Each point within the graph represents a measurement time point (M1, M2). One can appreciate from the graph that, overall, the tumour size decreased during the treatment.

2.3.2.2 Tumour elasticity

Fig 2.8(b), Fig 2.9(b) and Fig 2.10(b) present the 3D-SWE volumes and multi-planar views of the *carcinomas* present in Patients 07, 05 and 03 (Protocol II) measured at different

times during their chemotherapy treatment. The tumour elasticity was 83.4 ± 20.7 kPa for Patient 07, 58.9 ± 26.6 kPa for Patient 05 and 13.4 ± 41.7 kPa for Patient 03.

The 3D-SWE volume offers a multi-planar view of the tumour elasticity distribution. The lesion contours are very well delimited from the surrounding tissue. As for the 3D-US images, the system also allows navigation in the axial (A), sagittal (T) and coronal (C) planes. In this particular case (or for all the patients), the elasticity colour-bar was fixed between 0 and 100 kPa.

Table 2.4 and Fig 2.14 present the tumour elasticity measurements for all the patients who took part in Protocol II. The volume and elasticity measurements were performed during the same sessions along the central-axial and central-sagittal plane of the lesions. Hence, four patients had their tumour elasticity measured three times, four patients four times, one patient five times and one patient six times. One observes a decrease in the tumour elasticity as the chemotherapy treatment takes place in almost all the patients. Only Patient 09 seemed not to react positively to the treatment, as the tumour elasticity increased from 80.0 ± 22.6 kPa to 97.7 ± 61.3 kPa between the first (M1) and the second (M2) measurement respectively. Nevertheless, the tumour elasticity appeared to remain quasi-stable by the time the third measurement was performed. Patient 10 also seemed not to react positively to the treatment, since the tumour elasticity increased from 89.7 ± 36.7 kPa to 102.4 ± 63.3 kPa from the first (M1) to the second (M2) measurement. However, by day the third measurement was performed, the elasticity had fallen to 79.3 ± 35.7.

Table 2.4. Monitoring tumour elasticity of the Protocol II patients. The tumour elasticity of ten patients (which did not take part in Protocol I) were measured periodically with 3D-SWE as they underwent neo-adjuvant chemotherapy treatment. As with the volume, the number of tumour elasticity measurements (M1 to M6) may vary from one patient to another since they were not necessarily monitored the same amount of times.

	Elasticity 3D-SWE [kPa]					
	M1	*M2*	*M3*	*M4*	*M5*	*M6*
Patient 01	94.9 ± 20.1	17.2 ± 5.7	18.4 ± 2.5	16.7 ± 5.7	--	--
Patient 02	99.5 ± 47.1	47.6 ± 16.3	25.3 ± 3.5	29.0 ± 14.0	--	--
Patient 03	13.4 ± 41.7	13.3 ± 22.6	15.9 ± 7.9	--	--	--
Patient 04	164.2 ± 29.2	62.2 ± 26.8	4.2 ± 11.7	--	--	--
Patient 05	156.9 ± 29.4	58.9 ± 26.6	37.7 ± 14.6	--	--	--
Patient 06	126.2 ± 53.6	67.6 ± 22.6	20.2 ± 4.5	24.7 ± 6.2	--	--
Patient 07	148.5 ± 33.1	83.4 ± 20.7	30.0 ± 19.1	26.8 ± 23.5	22.7 ± 7.4	17.0 ± 3.1
Patient 08	46.1 ± 43.6	49.8 ± 19.3	9.7 ± 11.1	14.9 ± 7.5	11.3 ± 6.6	--
Patient 09	80.0 ± 22.6	97.7 ± 61.3	97.9 ± 15.8	--	--	--
Patient 10	89.7 ± 36.7	102.4 ± 63.3	79.3 ± 35.7	--	--	--

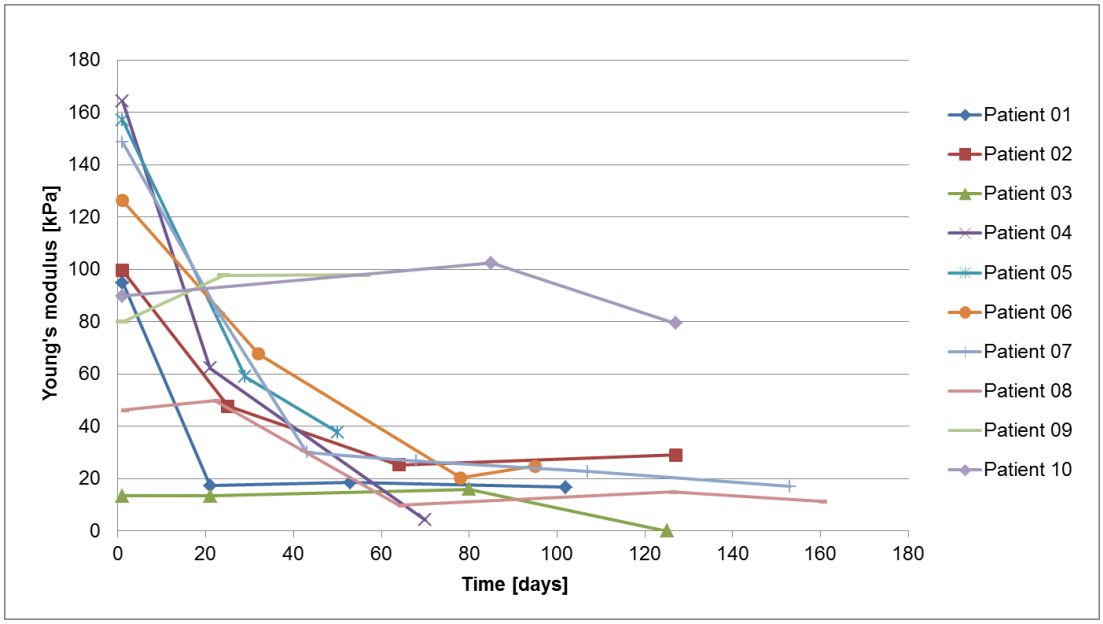

Fig 2.14. Tumour elasticity monitoring during chemotherapy treatment for the ten patients taking part in the Protocol II. Each point within the graph represents a measurement time point (M1 to M6). The graph shows a drastic tumour elasticity decreased caused by the neo-adjuvant chemotherapy treatment.

Fig 2.15 contains the elasticity evolution for the carcinoma present in Patient 07. The lesion elasticity decreased enormously during the chemotherapy, going from 148.5 ± 33.1 kPa at the beginning of the treatment to 17.0 ± 3.1 kPa in 153 days.

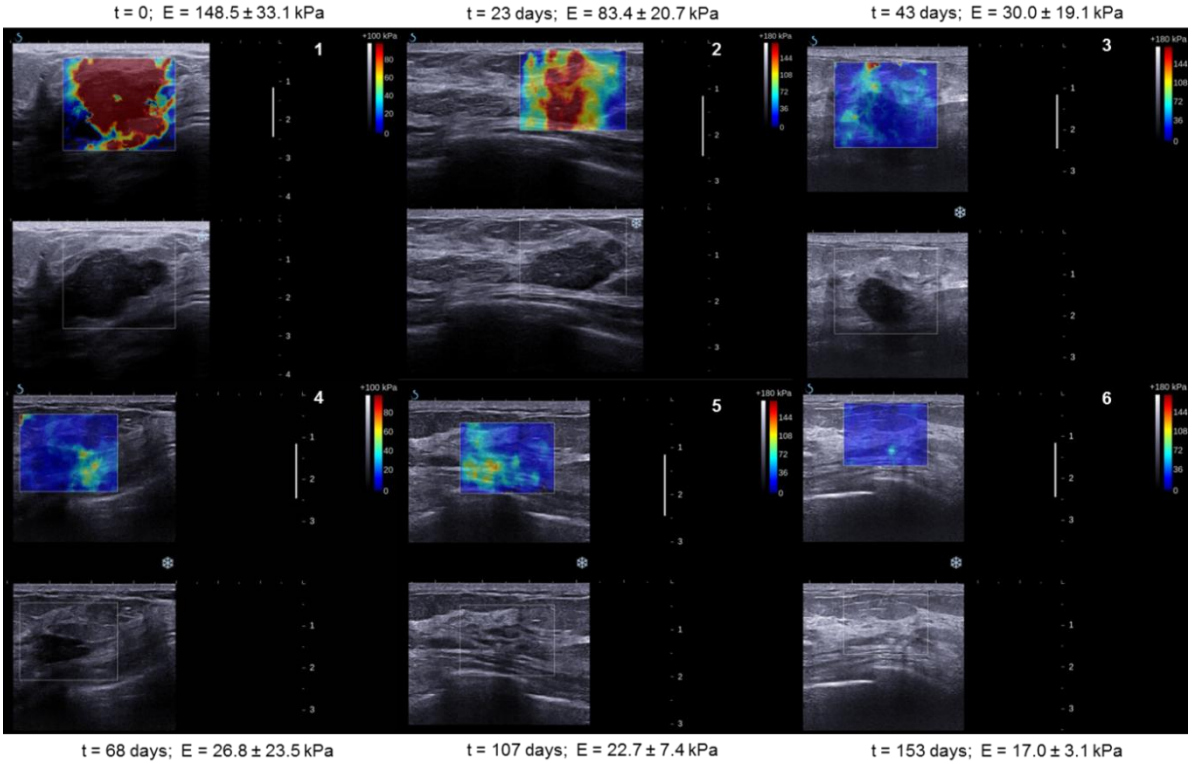

Fig 2.15. Tumour elasticity monitoring during chemotherapy. The elasticity of the carcinoma present in Patient 07 decreased dramatically during the treatment. The tumour elasticity went from 148.5 ± 33.1 kPa at the beginning of the treatment to 17.0 ± 3.1 kPa in 153 days.

2.4 Discussion

The volume measurements performed by 3D-US and MRI in Protocol I showed good accordance. However, in most of the studied cases, The volumes measured by 3D-US were smaller than the ones measured by MRI. In only one patient, the tumour 3D-US volume was higher than the MRI one. The largest tumours presented the largest difference between the two volumes, due to being usually the most difficult tumours to measure since they highly attenuated the ultrasound waves. An additional error source when measuring the tumour maximal diameters by 3D-US may have been the impossibility to clearly distinguish the tumour contours. Therefore, assumptions had to be made on the lesions' contours in order to be able to measure the tumour maximal diameters and hence calculate the volumes. The fact that the volume measurements by MR strongly depend on the parameters the clinician introduces into the volume calculation software, may also constitute an additional source of error for the MRI volume calculations.

The box-plot shows that the 3D-US and MRI volumes presented similar value ranges and that the mean values of each dataset were also close. The Bland-Altman test sets a norm for future measurements, as the volumes estimations with both imaging techniques will have to be within the 95% limits of confidence obtained in this study to be validated. Nevertheless, a higher number of patients would be needed to conclude on the agreement of both imaging techniques when measuring tumour volume.

According to the experienced breast radiology at the *Institut Curie* with whom this work has been performed, the difference between the 3D-US and the MRI volume estimations should be not higher than 15%. However, differences between 15% and 30% may be acceptable, given the fact that the volume estimations with both imaging techniques are very operator-dependant. Thus, leading to the under or over estimation of the lesion volumes.

In Protocol II, the use of 3D-SWE elastography offered new and valuable information on the tumour elasticity distribution. Such information, along with the measurement of the tumour volume (which has long been used by radiologists as the most important indicator of chemotherapy efficiency), would permit better monitoring the effectiveness of chemotherapy treatments. By looking at Table 2.2 and Fig 2.11, one observe a decrease in the tumour volume during the chemotherapy, meaning that the patients were reacting positively to the treatment. Difficulties were encountered for the 3D-US volume calculations as the treatment took place. Firstly, because of the chemotherapy, it was very hard to distinguish the tumour contours. Secondly, even if very small metallic pieces were inserted right in the tumour to make it more visible during the examinations, sometimes it was very difficult to find the tumours as they had become smaller and were surrounded by other biological tissues. Hence, these two factors may have negatively influenced the 3D-US volume calculations.

Tumour elasticity seemed to have followed the decrease trend showed by tumour volume during chemotherapy. Nevertheless, not all patients had the same amount of measurement points, which would have permitted a better tumour monitoring. For instance, it would have been very useful to have additional measurement points in the case of Patient 10, in order to monitor the tumour evolution and conclude whether the volume and elasticity trends were representative of the patient's health condition, and if the chemotherapy was having any major effect on the tumour. In other words, a much higher number of patients would be needed, with measurement points as equally distributed in time as possible. As with the volume, the elasticity measurements may also have been affected by the impossibility to image the entire tumour. Nonetheless, 3D-SWE showed a clear elasticity contrast between the tumours and their surrounding tissues, allowing to identify the tumour contours. Another obstacle is the difficulty to image exactly the same tumour plane after a given amount of time, since the tumour shape and size may vary between a measurement and the next

One of the goals of this clinical study was to calculate tumour volume from the 3D elasticity maps and compare it with the 3D-US and MRI volumes, but the nature of some lesions made it difficult. It was hard to establish the tumour boundaries along the sagittal and transversal planes, as the elasticity contrast between the lesions and the surrounding healthy tissue was not strong enough in most of the studied cases. Nonetheless, a few tumour volumes which were retrieved from the elasticity maps were higher than the 3D-US and MRI ones.

2.5 Conclusion

This chapter introduced the concept of 3D-SWE and presented a new 3D-US imaging system. The feasibility of using 3D-SWE as a novel complementary technique to standard ultrasonography to evaluate breast lesions has been assessed. 3D-SWE permits a real-time multi-planar tumour examination by allowing the retrieval of the complete 3D volume of the lesion in a single acquisition. Moreover, 3D-SWE provides unprecedented clinical multi-planar information on the elasticity distribution inside and around the breast lesion. The coronal plane of the 3D-SWE multi-planar view offers additional information on the tumour nature (characteristics, magnitude and borders), which are difficult to detect during a standard examination. Future 3D-SWE versions will aim to extend the characterization benefits of the coronal plane to the axial and transversal planes of the lesions. The 3D-SWE technique is also able to generate the radiation force needed to excite the tissue and to image the shear wave propagation in real time in three dimensions and without the use of external components apart from the 3D probe. To summarize, acquired 3D volumetric Data together with 3D display features might deliver new and beneficial diagnostic information specially on the coronal

plane of breast pathology, contributing to a high-resolution morphological assessment free of magnification.

The reduced number of patients who took part in Protocol II (10) constitutes a limitation. A much higher population would be necessary in a next clinical study in order to be able draw more conclusions on the potential applicability of 3D-SWE in the monitoring of patients undergoing neo-adjuvant chemotherapy treatments. In addition to this, the development of a software tool for tumour segmentation would result in more accurate 3D ultrasound and elastography tumour volume calculation.

Even though it is clear that histological studies have been performed on each patient by the *Institute Curie*, the results of such studies were not accessible to us due to the private policy established by this medical institution..

In this chapter, 3D-US and 3D-SWE were used to measure tumour volume and elasticity respectively in order to monitor the response of patients to neo-adjuvant chemotherapy. However, in general, clinical studies have their limitations: the number of patients is often limited, not all the patients undergo the same type of chemotherapy treatment due to not having the same type of lesions, and the error in longitudinal measurements is often high. All this obstacles are not present in pre-clinical studies. The next chapter contains the results of a pre-clinical study, in which a human breast carcinoma was implanted in the flank of immune-deficient female mice. 2D-US and the SSI technique were used to monitor the response of the animals to a particular type of chemotherapy treatment.

References

[1] Jemal A., Bray F., Center M., Ferlay J., Ward E., Forman D., "Global Cancer Statistics".*CA CANCER J CLIN 2011*.
[2] Guerin S., Doyon F., Hill C., "The frequency of cancer in France in 2006, mortality trends since 1950, incidence trends since 1980 and analysis of the discrepancies between these trends", *Bull Cancer*, Vol. 96, no. 1, pp. 51-57.
[3] Mendelson E. B., Berg W.A., Merritt C.R., "Towards a standardized breast ultrasound lexicon, BI-RADS: ultrasound", *Semin Roentgenol*, 36(3), pp.217-225, 2001.
[4] Homer M.J., "Imaging features and management of characteristically benign and probably benign breast lesions", *Radiol Clin North Am*., 25(5), pp.939-951, 1987.
[5] Hall F.M., "Negative predictive value of breast imaging in patients with palpable lesions", *AJR Am J Roentgenol*. 179(4):1073-1074, 2002.
[6] Rosen E.L., Baker J.A., Soo M.S., "Malignant lesions initially subjected to short-term mammographic follow-up". *Radiology*,223(1), pp.221-228, 2002.
[7] Berg WA, Cosgrove DO, Doré CJ et al: Shear-wave Elastography Improves the Specificity of Breast US: The BE1 Multinational Study of 939 Masses. Radiology 2012, 262(2): 435-449.
[8] Cosgrove DO, Berg WA, Doré CJ et al: Shear wave elastography for breast masses is highly reproducible. Eur Radiol 2011 Dec 31.
[9] Athanasiou A., Tardivon A., Tanter M., Sigal-Zafrani B., Bercoff J., Deffieux T., et al. "Breast lesions: quantitative elastography with supersonic shear imaging-preliminary results", *Radiology*, 256(1), pp. 297-303, 2010.
[10] Lee J. H., Kim S. H., Kang B. J., Choi J. J., Jeong S. H., Yim H. W., et al., "Role and clinical usefulness of elastography in small breast masses", *Acad Radiol*, 18(1) pp.74-80, 2011.
[11] Chang J. M., Moon W. K., Cho N., Yi A., Koo H. R., Han W., et al., "Clinical application of shear wave elastography (SWE) in the diagnosis of benign and malignant breast diseases", *Breast Cancer Res Treat.*, 129(1), pp. 89-97, 2011.
[12] Itoh A., Ueno E., Tohno E., Kamma H., Takahashi H., Shiina T., et al., "Breast disease: clinical application of US elastography for diagnosis", Radiology, 239(2), pp. 341-350, 2006.
[13] J. E. Lindop, "2D and 3D Elasticity Imaging Using Freehand Ultrasound", A dissertation submitted to the University of Cambridge for the degree of Doctor of Philosophy, 2008.

[14] T. Chaunzwa and K. Nightingale, "3D Ultrasound Elastography (Remote palpation using acoustic radiation force)", Work posted on the *National Instruments Community website*, 2011.

3. Chapter 3. What is the pathology underlying stiffness?

Even though the clinical study presented in the previous chapter offered encouraging results as it allowed to monitor the response to chemotherapy of naturally grown tumours in real clinical scenarios, it possessed some limitations compared to a pre-clinical study. Firstly, it had a narrower degree of experimental flexibility due to the fact that the patient health was capital. Secondly, the study guidelines did not permit performing histo-pathological analysis on the entire tumours at different time points. Only tiny tumour samples were analysed after being taken by biopsy. For all the previously mentioned reasons and although clinical studies are vital in medical research, pre-clinical protocols are a good possibility to monitor tumour response to anti-cancerous therapies in the cases in which they might offer valuable information that could be employed to better understand the results of a subsequent clinical study.

The results of the clinical study presented in the previous chapter evaluated the efficiency of Ultrasound (US) and 3D-Shear Wave Elastography (3D-SWE) in the monitoring of tumour response to neo-adjuvant chemotherapy in patients presenting breast lesions. In fact, SSI has become an increasingly popular technique due to its efficacy in the detection of breast cancer abnormalities. Nevertheless, since the SSI is a relatively new technique, there are still some patterns which need to be clearly explained. Additionally, there is very little literature on the relationship between tissue pathology and stiffness. Therefore, the question raised is: what is the pathology underling stiffness? Which pathological parameters are responsible for tumour stiffness?

This chapter tries to partly answer this complex question and contains the results of a pre-clinical study performed on a human breast cancer model implanted in mice. The study is divided in two phases: growth and treatment. During the growth phase, the tumour size and elasticity are measured by conventional Ultrasound and the SSI technique respectively. Then, during the treatment phase, a different group of mice the animals carrying the same type of cancerous tumour undergo chemotherapy during 150 days. During this phase, tumour size and elasticity are again measured periodically by conventional Ultrasound and the SSI technique in order to assess the efficiency of the treatment. During both phases, some animals are sacrificed every week to perform histo-pathological measurements.

3.1 Materials and Methods

The project was divided in two phases: tumour growth and tumour treatment by neo-adjuvant chemotherapy. The materials and methods employed for both phases are identical except for a few small variations which will be clearly explained throughout this section.

3.1.1 Tumour growth phase

In this phase, small (a few millimeters) pieces of a human breast cancer tumour model were implanted in the flank of thirty immune deficient mice. Measurements of tumour size and global elasticity were performed periodically.

3.1.1.1 Tumour model

This protocol has the approval of the local ethics committee for animal research. A human tumour xenograft model called "HBCx-3" [1] (invasive ductal carcinoma; luminal B: Oestrogen Receptor positive; Progesteron Receptor positive; Her2 negative) was implanted subcutaneously in twenty-four 5 week-old athymic Swiss nude female mice (Janvier®, Saint Berthevin, France). One ml of an Estrogen solution (0,85mg/ml of β-oestradiol) was added to 100 ml of the drinking water. The animals were then monitored twice a week for signs of tumor growth. The tumours were collected from patients who underwent surgery at the *Institut Curie* (Paris, France) and then implanted subcutaneously in nude mice. Those that grew were removed after reaching between 1 mm^2 in size, fragmented and then re-implanted in different mice (Fig 3.1). Comparisons to validate these models were performed with human tumours and showed high pathological correlation [1]. Measurements of tumour size and elasticity started when the Maximal Tumour Diameter (MTD) reached approximately 3.0 mm. This period is called "latency phase", and for the growth part of this preclinical protocol, it ranged between 28 and 43 days from the tumour implantation (see Fig 3.3).

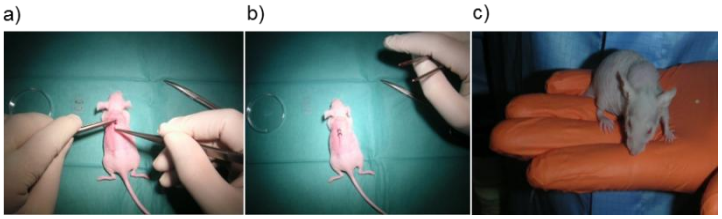

Fig 3.1. Xenograft implantation technique. After peritoneal anesthesia, a tiny (1 to 2 mm^2) piece of human breast tumour is implanted on the flank of the mouse. Measurements of tumour size and elasticity begun after the "latency phase" was over. Courtesy Laboratoire d'Investigation préclinique (LIP), Institut Curie, Paris-France.

The duration of the latency phase was chosen based on the growing pattern described in the literature [1]. The idea was to begin the measurements when the MTD had reached an approximate value of 3 mm, so the tumours could be distinguish from their surrounding tissue with ultrasound.

3.1.1.2 2D-Ultrasound and the Supersonic Shear Wave Imaging (SSI) technique

As said before, measurements of tumour size and elasticity started when the MTD reached approximately 3.0 mm (latency period). An ultrafast echographic imaging device (Aixplorer, *SuperSonic Imagine, France*) along with a 15 MHz linear array probe (256

elements, pitch 0.125 mm, elevation focus 8 mm, *Vermon, Tours, France*) were employed for both measurements. The animals were anesthetized by using isoflurane (*Aerrane®; Baxter S.A.S, France*) before being covered with coupling gel (Fig 3.2).

Fig 3.2. Mouse positioning. During the experiment, the animals were placed on a thermal-bed and covered with coupling gel after being anesthetized.

Ultrasound B-mode was used to measure the MTD on the tumours' central-sagittal and central-transversal plane. Before each acquisition, the probe was removed and repositioned in order to test the repeatability of the measurement.

The SSI technique was used to measure the mean tumour elasticity. Elastography images were acquired along the central-sagittal and central-transversal planes of the tumours. The colour-bar was fixed between 0 and 60 kPa, with the pixels in black and red representing the lowest and highest elasticity values respectively. A round Region of Interest (ROI) was manually positioned on the tumour. Its size was defined to be the biggest possible while entirely included within the tumour, avoiding obvious artefacts. ROI size, mean values of elasticity, and standard deviation within the ROI were collected.

Fig 3.3 presents the measurement planning. The study begun with 30 mice. Their latency period varied from 28 to 43 days from the tumour graft. The median interquartile range (IQR) time of each measurement is presented in brackets. N represents the number of mice monitored at each time point. Some animals died accidentally during the study (Death) whereas some others were sacrificed to perform pathological analysis.

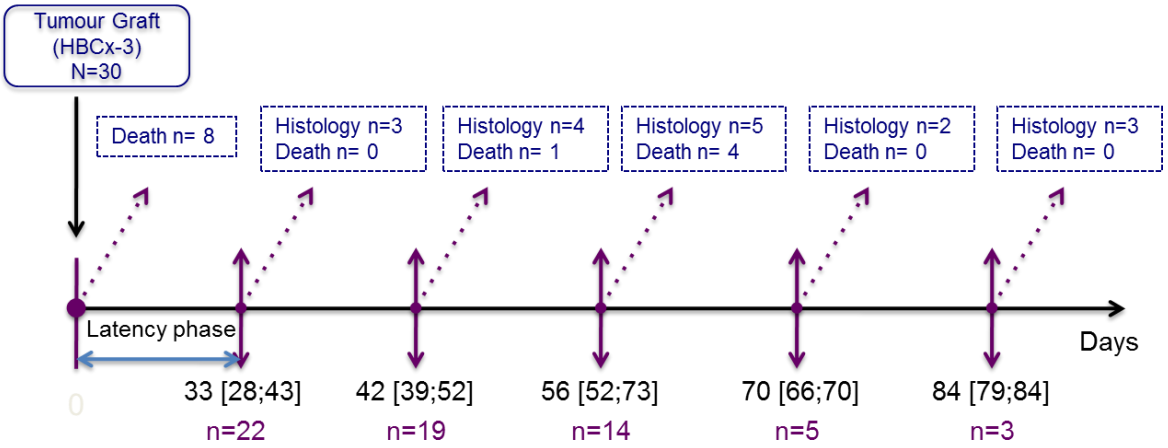

Fig 3.3. Tumour size and elasticity measurement planning. The masses were measured from 1 to 5 times, starting from the day on which the Maximal Tumour Diameters (MTD) reached about 3.0 mm. This period is called the "latency phase". N represents the number of mice monitored at each time point in days. The median interquartile range [IQR] time of each measurement is shown in brackets. At each time point, some animals died due to the implanted tumours (Death) whereas some others were sacrificed for histo-pathological analysis (Pathology).

3.1.1.3 *In vivo/ex vivo* comparison of elasticity values

Seven mice were sacrificed the same day right after performing elasticity measurements. The tumours were then removed from the mice and placed in agar-gelatin solutions. The tumour elasticity values were subsequently measured *ex vivo*. This experiment was meant to test the influence of tissue interfaces on the *in vivo* elasticity measurements. After the experiment, the tumours were submerged in paraffin to preserve them for the subsequent pathological studies.

3.1.1.4 Pathological analysis

The pathological analysis was performed on all the tumour samples in collaboration with the Pathology Department from *l'Hôpital Européen Georges Pompidou* (HEGP) in Paris-France. At each time point, 2 to 5 mice were sacrificed after performing the elastography measurements in order to have tumours of different sizes and ages. The samples were submerged in a formalin solution during from 24 to 48 hours. Then, they were removed and cut along the central-transversal plane, embedded in paraffin and stained with HES (Hematoxylin Eosin Safranin-1 slice) and Masson's trichrome (1 slice). Immuno-staining of vessels was performed with a mouse CD31 antibody. All the slides were digitally scanned by using a digitizer from HEGP (Hamamatsu Photonics). Staining and digitalization were performed at different times.

The 'HBCx-3' model was composed of three different areas: a cellular area containing viable tumor cells, a fibrotic area mostly composed of collagen fibers, and a necrotic area containing non-viable tumor cells and a few collagen fibers. The proportion of each of these three areas was quantified blinded to elastography results in collaboration with a pathologist

(twenty years of experience in breast pathology). The respective percentage of the surface occupied by each pathological feature was retrieved after manual delineation of the necrotic area on the HES stained slides (Fig 3.4) and the fibrotic area on the Masson's trichrome stained slides (Fig 3.5). The proportion of cellular tissue was calculated as the remaining percentage.

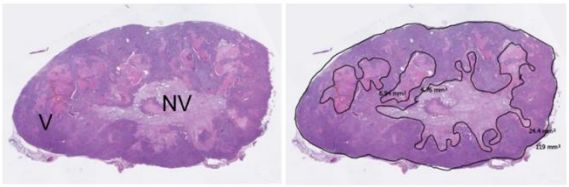

Fig 3.4. Examples of the BC52 human tumour models. Magnification (x10) after HES staining. Viable (V) and non-viable (NV) areas were obtained after manual delineation.

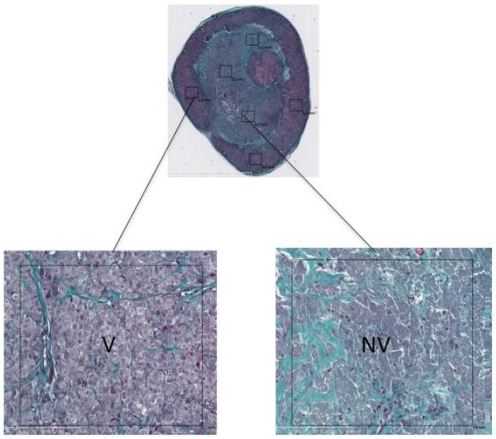

Fig 3.5. Masson's trichrome staining. The viable (V) and non-viable (NV) tumour areas were manually delineated by experienced pathologists. The fibrosis(coloured in green) rate was calculated by colour thresholding with the software tool Image J®.

3.1.1.5 Statistical analysis

Mean tumour diameter values are given as median and interquartile range [IQR]. The elasticity values are given as the mean ± standard deviation of the pixels within the ROI and the pathological parameter values are expressed as the mean ± standard deviation.

Correlation coefficients between the elasticity values and the pathological scores were calculated by using the *Spearman correlation test*. *In vivo* and *ex vivo* elasticity values were compared by using a *Paired Student t-test*.

For the sake of the comparison between elasticity and pathological features, the removed tumours were classified into three groups corresponding to tertiles of elasticity values: group 1 *(soft tumours, n = 6)*, group 2 *(intermediate tumours, n = 6)* and group 3 *(stiff tumours, n = 5)*.

Repeatability of the elastography measurements was calculated by retrieving the mean value (m), the standard deviation (σ) and the variation coefficient (σ/m) of three repeated measurements performed by the same examiner on each tumour.

The calculated *P* values were two-sided and values of $P < 0.05$ were considered to be statistically significantly different.

3.1.2 Tumour treatment by chemotherapy

For this part of the animal study, a different group of mice was used. The same human cancerous tumour model was implanted in the flank of eight nude immune-deficient female mice. Fig 3.6 describes the planning structure. Aiming to be able to monitor the tumour reaction to the chemotherapy over the time, and based on the xenograft growth pattern observed during the growth phase, the latency period of the chemotherapy phase of the study was set to 60 days after implantation. This was done to allow the tumours to reach a size approximately twice as big as the one reached after the latency period of the growth phase of the study,. Once the latency period ended, 2D ultrasound and 2D Shear Wave elastography measurements were performed and the anti-tumour drug called *Xeloda*® (540 mg/kg) administered (tube-feeding) to the mice on weekly basis. This part of the study is still in progress, with pathological measurements due to be performed (by using the same techniques employed in the tumour growth phase) when a change in elasticity becomes visible. The protocol was set to have a duration of 150 days. However, the mice had to be sacrificed five weeks after the beginning of the treatment since their health had deteriorated enormously. Hence, another group of animals will be needed to complete this phase of the study.

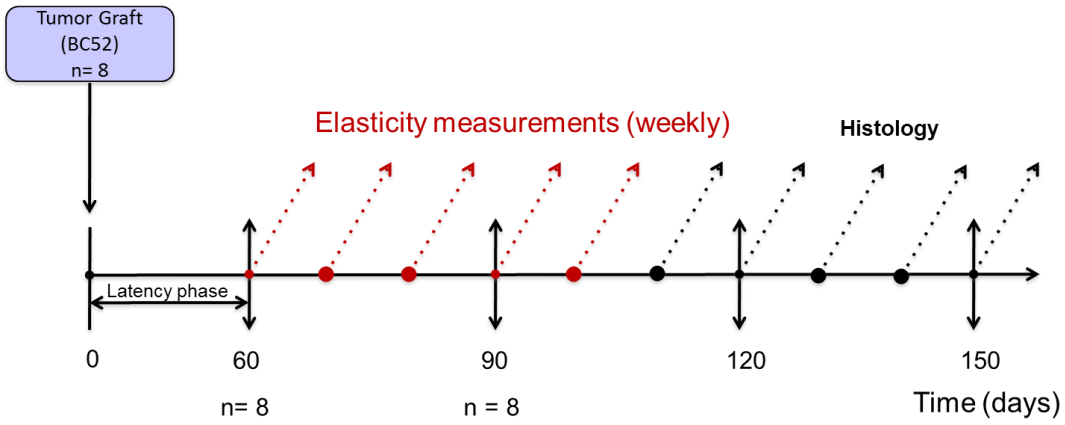

Fig 3.6. Planning structure for the chemotherapy treatment phase. Elasticity measurements are performed on a weekly basis and begun right after the latency phase (sixty days approximately). Histology measurements are scheduled to be performed when an important change in elasticity takes place. This phase is still in process.

3.2 Results

3.2.1 Tumour growth

3.2.1.1 Tumour model

At the beginning of the study, 30 tumours had been ectopically implanted in nude female mice. Eight of them died after the implantation. The animals started to be monitored

immediately after the latency phase was over (between 28 and 43 days after the implantation for the growth part of the study). Therefore, tumour measurements begun at different dates for each mouse. The duration of the latency periods ranged from 17 to 56 days. Table 3.1 presents the tumour's maximum diameters during the growth phase measured at each measurement time point. The number of mice at each measurement point varied since some animals were sacrificed for pathology whereas some others died due to the implanted tumours. Three tumours were measured longitudinally five times, two tumours were measured four times, nine tumours were measured three times, five tumours were measured twice and three tumours were measured only once.

3.2.1.2 The Supersonic Shear Wave Imaging (SSI) technique

Sixty-three measurements were performed with a median value for the ROI (area engulfed by the white circles on the tumour elasticity maps presented in Fig 3.8, Fig 3.11, and Fig 3.13) of 5 mm. The intra-observer measurement average standard deviation and variation coefficient was 3.3 and 12.5% respectively, showing the good accuracy of the technique. Longitudinal measurements showed that the mean tumour elasticity values increased with time. The mean elasticity values were respectively 10 [8;14], 24 [20;29], 43 [30;65], 50 [41;56] and 74 [66;91] kPa for measures 1 to 5 (Fig 3.7 and Table 3.1).

The shear elasticity map heterogeneity increased with tumour stiffness. The mean Standard Deviation (SD) for the elasticity values within the entire ROI over time were 1.3 [0.8;2.2], 2.5 [1.4;3.7], 5.6 [2.7;8.7], 5 [2.2;2.8] and 9.4 [6.7;17] kPa for the measurements 1 to 5 respectively (Table 3.1).

The elasticity maps placed at each measurement time point on Fig 3.7 correspond to the mouse monitored five times, and are the same illustrated in Fig 3.8. Tumour heterogeneity increased with tumour size.

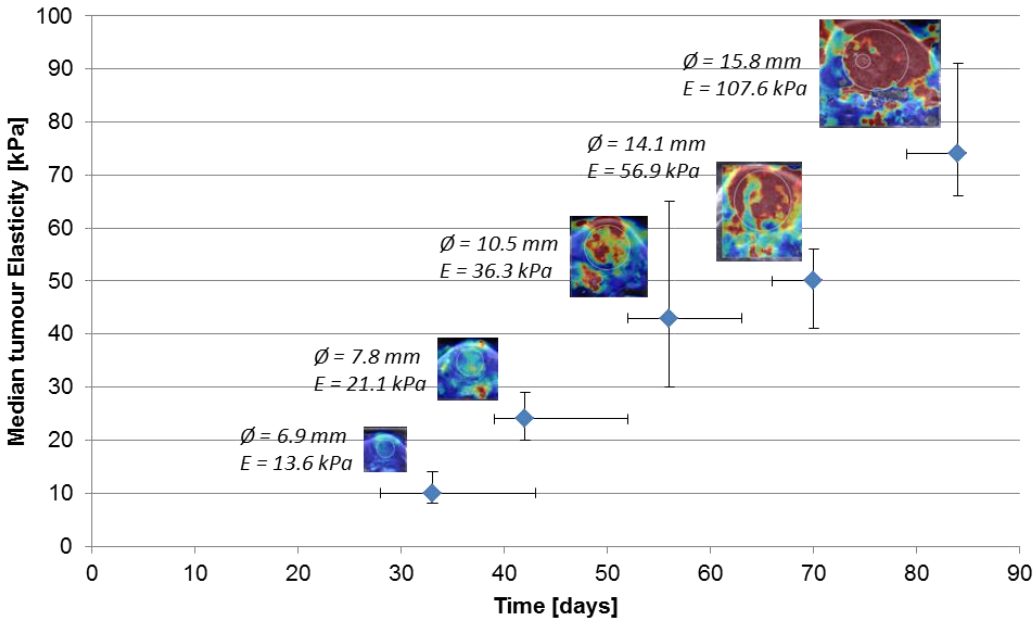

Fig 3.7. Median tumour elasticity over time during the growth phase. The vertical and horizontal error bars represent the IQR of the elasticity value and measurement time point respectively (as the growth rate was different for each tumour). The elasticity maps for one of the tumours measured five times are showed at each measurement point. The elasticity maps are colour-coded to represent elasticity values for each pixel within the region enclosed by the white circles (ROI) within which the mean elasticity values were measured. The elasticity colour-bar was fixed between 0 (black) and 60 kPa (red). The tumour mean elasticity, mean maximum diameter and heterogeneity increased over time within the ROI.

Table 3.1. Mean values for the parameters measured during the tumour growth phase. The number of tumours varied at every measurement point since some animals were sacrificed for pathology and others died because of the tumour graft.

	Measure 1	*Measure 2*	*Measure 3*	*Measure 4*	*Measure 5*
Time from tumour graft (days)	33 [28;43]	42 [39;52]	56 [52;73]	70 [66;70]	84 [79;84]
Total number of mice (N)	22	19	14	5	3
Removal for pathology (N)	3	4	5	2	3
Death	0	1	4	0	0
MTD (mm)	5.7 [4.5;6.4]	7.6 [6.6;8.6]	10.2 [8.1;12.3]	12.2 [11.6;12.8]	15.8 [14.6;15.9]
Median ROI Diameter (mm)	4.0 [2.0;4.7]	5.0 [4.0;6.0]	6.0 [5.0;8.0]	7.0 [6.0;8.5]	9.0 [9.0;9.5]
Mean ROI Elasticity (kPa)	10.3 [7.8;13.5]	23.5 [19.7;28.9]	42.6 [29.9;64.5]	49.6 [41.1;55.6]	74.0 [66;90.8]
Elasticity Standard Deviation (STD) within ROI	1.3 [0.8;2.2]	2.5 [1.4;3.7]	5.6 [2.7;8.7]	5.0 [2.2;12.7]	9.4 [6.4;17]

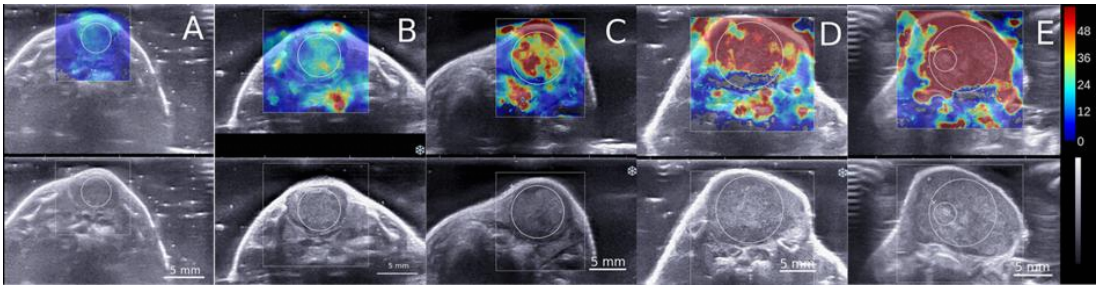

Fig 3.8. (Above) Elasticity color maps (0 to 60 kPa); (Below) Corresponding 2D-US axial plane view of the tumour depicted in Fig 3.7 at each of the five measurement points: A) day 35, diameter = 6.9 mm, mean elasticity = 13.6 kPa; B) day 42, 7.8 mm and 21.1 kPa; C) day 56, 10.5 mm and 36.3 kPa; D) day 70, 14.1 mm and 6.9 kPa; E) day 84, 15.8 mm and 107.6 kPa.

As shown by the results of the Spearman correlation test (Fig 3.9), there was a very good correlation between tumour elasticity and tumour size (MTD), with r = 0.94, $P < 0.0001$.

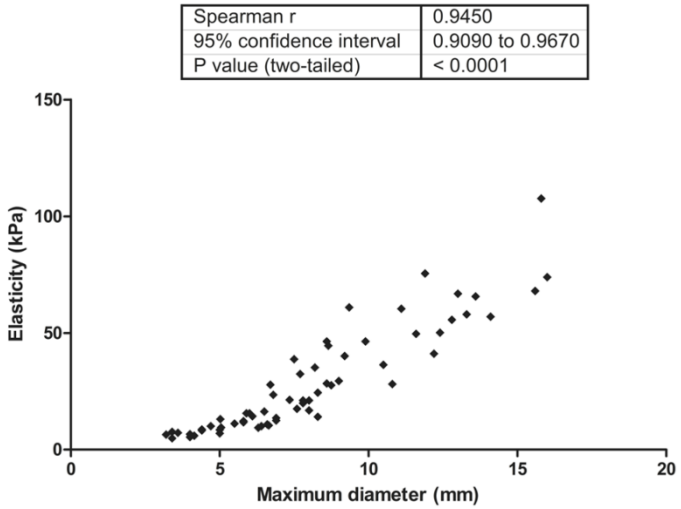

Fig 3.9. Spearman correlation test. Median elasticity value vs. tumour size (MTD). As tumours grew, the average elasticity values within the ROI increased, presenting an excellent correlation to size (r = 0.94; P < 0.0001).

3.2.1.3 *In vivo*/*ex vivo* comparison of elasticity values

The elasticity values measured *in vivo* and *ex vivo* did not show any significant difference ($P = 0.81$) according to the performed *Paired Student t-test*. Fig 3.10 presents the box-plot of the *in vivo* and *ex vivo* measured mean elasticity values. The maximal diameter of the tumours chosen for these measurements ranged from 6.1 to 13.9 mm, with an *in vivo* mean elasticity value ranging from 21.9 to 77.9 kPa respectively. Fig 3.11 depicts the *in vivo* and *ex vivo* measured elasticity maps for one of the tumours used for this experiment.

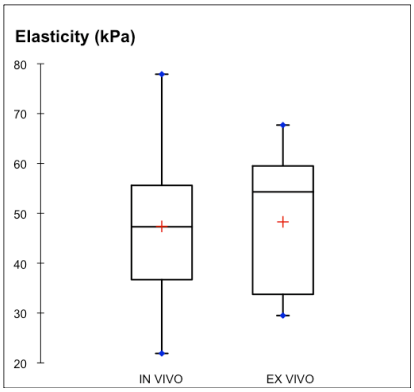

Fig 3.10. In vivo and ex vivo mean elasticity values. A Paired Student t-test showed no significant difference between both measurements (P = 0.81).

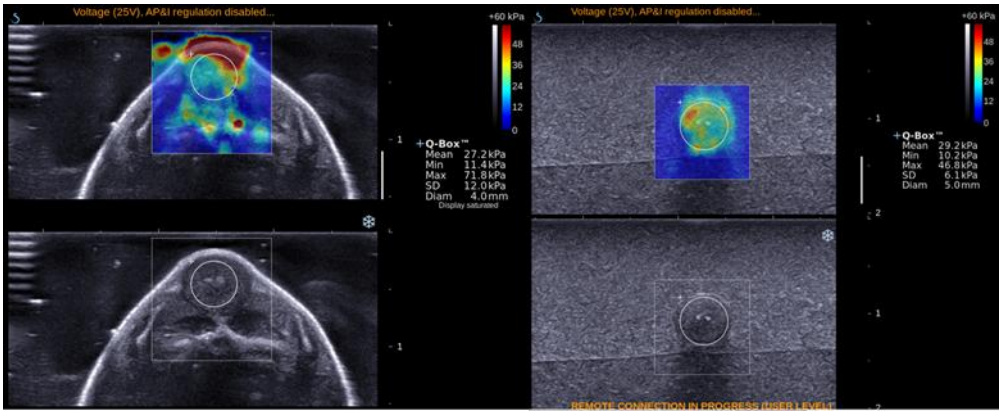

Fig 3.11. Elasicity maps for one of the tumours nine weeks after the implantation. (Left) in vivo and (right) ex vivo measurement. The images show there is very little difference between the in vivo and the ex vivo elasticity maps. The color-bar was fixed between 0 and 60 kPa for both measurements. The in vivo and ex vivo mean tumour elasticity was 27.2 kPa and 29.2 kPa respectively.

3.2.1.4 Pathology

In total, eighteen tumours were removed to perform pathological analysis. One of the removed tumours was excluded due to being technically inadequate. Therefore, only seventeen tumours were used for pathology. After staining, thirty-four slides were digitally scanned (one slide for HES and one for Masson's trichroma for each tumour).

Mean values and the corresponding standard deviations of each pathological parameter for each of the three elasticity groups (group 1 *(soft, n = 6)*, group 2 *(intermediate, n = 6)* and group 3 *(stiff, n = 5)* are presented in Table 3.2. Fig 3.12 contains the box-plots with the percentages of necrosis, cellularity and fibrosis for each elasticity group.

*Table 3.2. Proportion of 'necrosis', 'viable cellular tissue' and 'fibrosis' with the corresponding standard deviation for each elasticity tertile. † and * indicate a statistical significant difference between the groups.*

	Group 1 (Soft, n = 6) *(12.8 ± 5.4 kPa)*	*Group 2 (Intermediate, n = 6)* *(49.3 ± 12.1 kPa)*	*Group 3 (Stiff, n = 5)* *(78.6 ± 16.9 kPa)*
Necrosis proportion (%)	40.0 ± 9.9 †	25.9 ± 13.6	18.0 ± 11.1 †
Cellular tissue proportion (%)	57.8 ± 8.4	70.1 ± 13.3	65.9 ± 12.2
Fibrosis proportion (%)	2.1 ± 1.7 †	3.9 ± 3.8 *	16.0 ± 6.0 †*

It is observed that the proportion of necrosis decreases with the stiffness (P = 0.02). There was statistically significant difference in the necrosis percentage between the elasticity groups 3 and 1 (40% and 18% of necrosis respectively), but not with respect to the group 2. No statistically significant difference was found in the percentage of cellular tissue within the three groups (P = 0.2) in spite of a slight increase in group 2. The proportion of fibrosis increased with the stiffness (P < 0.0001). There was statistically significant difference in the fibrosis percentage between the elasticity groups 3 and 2 (16% and 3.9% of fibrosis respectively), but not between the groups 2 and 1. The stiffest tumours were much more fibrotic than the other two elasticity groups Regarding the elasticity in each of the seventeen tumours, there was a significant negative correlation with respect to the percentage of necrosis (r = -0.76, p = 0.0004), a high positive correlation with respect to the percentage of fibrosis(r = 0.83, p = 0.0001) and no significant correlation with respect to the percentage of cellular tissue (r = 0.4, p = 0.1). Fig 3.13 depicts tumours of different sizes after HES and Masson's trichrome staining and the respective elasticity maps.

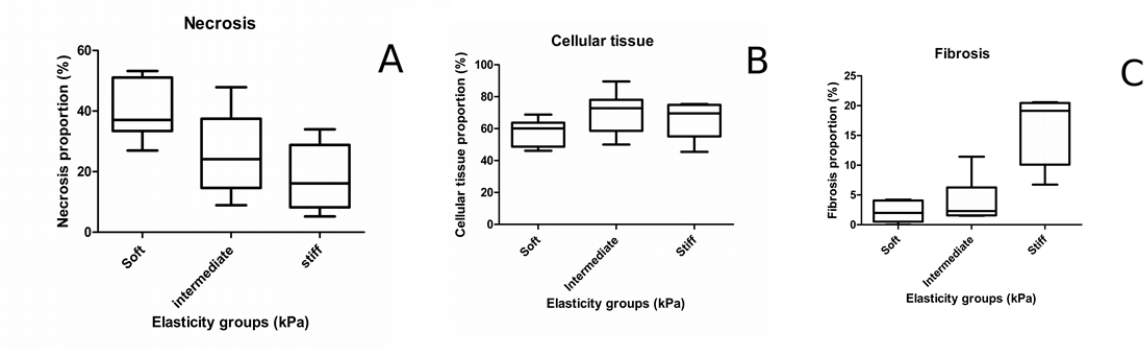

Fig 3.12. Percentage of necrosis (A), cellular tissue (B) and fibrosis (C) for each of the three elasticity groups. A) The proportion of necrosis decreased with the stiffness (p = 0.0004). B) No significant changes were found in the cellular tissue proportion (p = 0.1) although the intermediate tumours presented a slightly higher value. C) The proportion of fibrosis increased with the tumour stiffness (p = 0.0001), with the stiff group presenting much higher percentages of fibrosis than the other two groups.

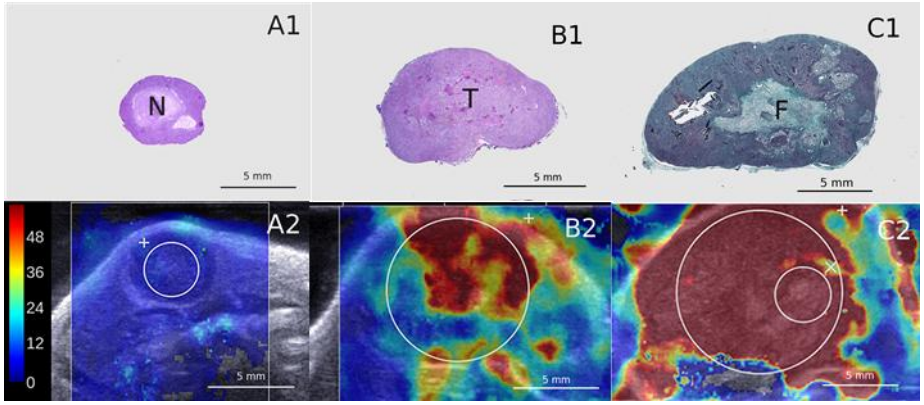

Fig 3.13. (Above) Tumours of different sizes after HES (A1, B1) and Masson's trichrome (C1) staining at low magnification (x10). (Below) Corresponding colour-coded elasticity maps with the color bar fixed between 0 and 60 kPa (A2, C2). A) A very small (5 mm) and a very soft (9 kPa) tumour showing a vast acellular necrotic center (N, stained light pink). B) The proportion of cellular tissue (T, dark pink) increased progressively in the

intermediate tumours of bigger size (50kPa – 11 mm). C) In the biggest and stiffest tumours (16 mm – 108 kPa), the proportion of fibrosis (light green) increased sharply.

3.2.2 Tumour treatment by chemotherapy

As said before, a different group of mice (n = 8) was used for the chemotherapy part of the study. Only preliminary results which include measurements of tumour diameter and mean elasticity are presented. As shown in Fig 3.14(a), the maximal tumour diameter (MTD) of the majority of the tumours (7 out of 8) tended to decrease during the five weeks of chemotherapy. Fig 3.14(b) shows the mean MTD over the entire mice population. The Mean MTD decreased from 16.3 mm at Week 1 to 11.9 mm at Week 5. A linear fitting of Fig 3.14(b) gave $y = -1.03x + 17.01$ as the best line equation and a correlation coefficient of 0.98 (R^2 = 0.97).

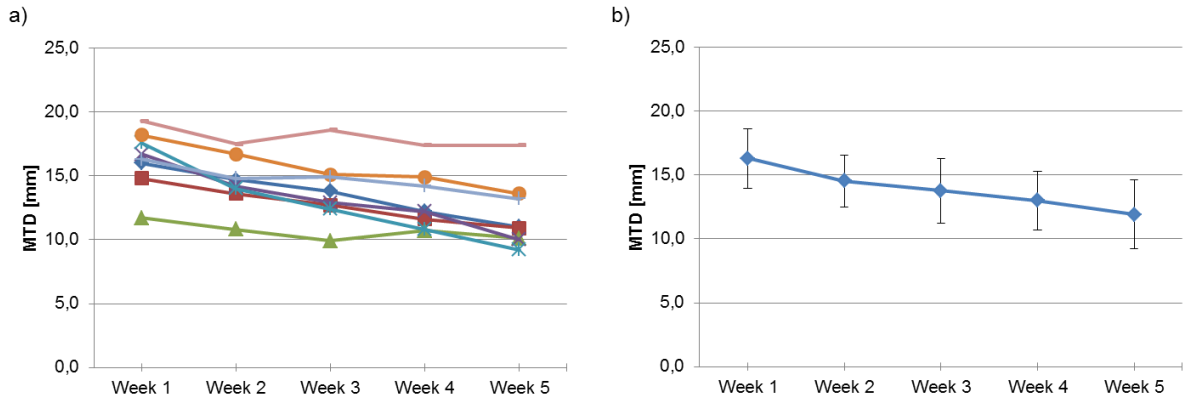

Fig 3.14. Tumour size measurement during chemotherapy. Measurements of MTD performed during four weeks after the end of the latency period. (a) In seven of the eight tumours, the MTD gradually decreased as they underwent chemotherapy. No error-bars were placed on the MTD plot since only one MTD was measured for each mouse; (b) The mean MTD over the entire mice population.

Fig 3.15(a) presents the preliminary results of the tumour global elasticity measurements for each mouse. Every tumour presented a different elasticity behavior, with some becoming stiffer and others softer as the mice underwent chemotherapy. Unlike the mean tumour diameter, the mean tumour elasticity decreased only after Week 4. This may be a scenario similar to one case presented in the clinical study of chapter 2 (Patient 03), where the tumour change in elasticity appeared at the third month of treatment, whereas a change in the tumour size was evident from the first month of treatment. The mean elasticity value over the entire population of mice went from 70.8 kPa to 44.1 kPa from Week 1 to Week 5 respectively. A linear fitting of Fig 3.15(b) gave $y = -5.43x + 80.00$ as the best line equation and a correlation coefficient of 0.77 (R^2 = 0.60).

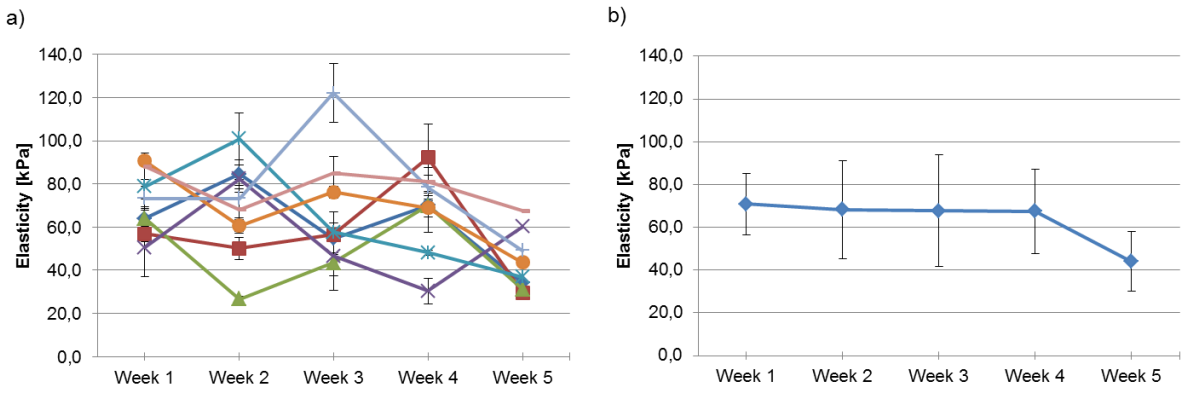

Fig 3.15. Global tumour elasticity measurement during chemotherapy after the end of the latency period. (a) The tumour elasticity did not show a clear tendency to increase or decrease as the tumours underwent chemotherapy; (b) The mean tumour elasticity over the entire population of mice shows no significant variations.

3.3 Discussion

This animal study showed that for the employed human breast invasive ductal carcinoma model (HBCx-3), tissue elasticity values increased with the Maximum Tumour Diamater (MTD), and that these two parameters were very well correlated. This is in very good accordance with clinical practice, where the biggest cancers are very often the hardest on palpation. It was also shown that stiffness changes were related to underlying pathological modifications. For instance, the softest and the hardest tumours presented the highest portions of necrosis and fibrosis respectively (see Fig 3.12).

The visual impression that tumour heterogeneity also increased with tumour size was confirmed by the increment in the standard deviation of the elasticity values within the ROI. No significant difference was observed between the measured *in vivo* and *ex vivo* (submerged in homogeneous gel) elasticity values; meaning that the elasticity measurements are not influenced by the tumour anatomical environment.

Since this work intended to study the relationship between pathology and stiffness, pathological slices were digitized to assess the proportion of the different histological elements, which allowed comparison among the tumours. Pathological changes related to stiffness throughout tumour growth are complex. The histo-pathological analysis showed that this particular tumour model could be described by three different characteristics: a cellular tissue area, often arranged as a peripheral ring and central fibrotic and/or necrotic areas. In the xenograft used in the study, the percentage of necrosis is the highest in small tumours, which are usually very soft. It seems that as tumours grow, cells proliferate, the proportion of necrosis decreases, the percentage of fibrosis increases and tumours become stiffer. In the largest tumours, the cellular tissue proportion slightly decreases, possibly because the vascular blood supply is not sufficient. The lost cellular tissue is not replaced by necrosis but rather by fibrosis, which may therefore be responsible for the highest values of stiffness. Indeed, this

study has shown the existence of a very significant correlation between stiffness and fibrosis. Historically, fibrosis has been known as being related to stiffness; the world 'scleros' (as in sclerotic) means 'hard' in ancient Greek. In liver diseases, it has also been shown that fibrosis, as quantified by the 'METAVIR' score, is related to increased stiffness [2]-[6].

To our knowledge, no studies have been published on the correlation between ultrasound elastography and pathology performed in a human breast cancer model implanted in small animals. Several studies have been conducted to assess the usefulness of elastography in clinical practice [7][8] as well as doing *in vitro* physics models [9]-[11], but very few have been performed *in vivo* in small animals. Such models have the advantage of permitting longitudinal monitoring during tumour growth to assess pathological changes over time. The large elasticity range obtained for different tumour sizes showed this xenograft model to be very useful to study the previously reported stiffness-size relationship, and to explore the histological parameters accounting for it. Furthermore, this breast carcinoma xenograft tumour has conserved the pathological morphological and molecular characteristics of the corresponding patient's tumour [1]. Therefore, the results, though not directly superimposable to *in situ* human cancers, provide cognitive data about the relationship between breast cancer and stiffness. This work shows that in further studies aiming to assess the pathology underlying stiffness in human breast lesions, tumour size must be taken into account as well as the pathological parameters.

In order to study the influence of the tumour anatomical environment (skin, spine and bones) on the elasticity measurements, *in vivo* and *ex vivo* experiences were performed in seven tumours. The results showed that for this particular xenograft implanted in the flank of nude mice, there was no significant difference between the *in vivo* and *ex vivo* elasticity measurements. Hence, the measured tumour elasticity values were not influenced by the tumour anatomical environment. The repeatability of three consecutive measurements performed by the same operator in each tumor was good. The average standard deviation and the intra-observer average variation coefficient were respectively 3.3 and 12.5% (for elasticity values ranging from 4.9 to 107.6 kPa). These results are in good accordance with a recent study by Wang *et al.*[12], who measured the shear modulus on spontaneously growing rat mammary tumours and demonstrated the *in vivo* reproducibility of the measurement.

During chemotherapy, tumour size seemed to have a tendency to decrease from the very beginning of the treatment. Nevertheless, the elasticity did not show the same marked tendency. Only between Weeks 4 and 5, the mean tumour elasticity over the entire population of mice decreased from 67.4 kPa to 44.1 kPa, respectively. However, one cannot not yet conclude that elasticity cannot be used as a chemotherapy treatment marker. The entire group of mice had to be sacrificed before the end of the study as their health conditions had

dramatically deteriorated. When comparing the results of this pre-clinical study with the ones of the clinical study presented in the previous chapter, one observes that in the clinical study, tumour size and elasticity decreased significantly during the chemotherapy treatment. Those tumours had grown naturally within the body of the patients, and no modification or alteration of their natural anatomical environment had been made. On the contrary, in this pre-clinical study, the mice anatomy was altered with the ectopically implanted grafts. Therefore, it would be necessary to monitor chemotherapy treatments in mice, varying some of the characteristics of the study such as type of chemotherapy drug, dose, and latency period duration, before concluding on the efficiency of elasticity as a biomarker for this this particularly type of neo-adjuvant chemotherapy treatment. Indeed, the latency period of the chemotherapy phase of the protocol should be shortened, as the 60 day period did not allow chemotherapy to counteract the tumor influence, probably because the tumour was too large and aggressive to be treated when the chemotherapy begun. Histo-pathological analysis should also help understand the tumour behavior during the treatment.

There are several limitations to this animal study. Firstly, only one tumour model was studied, which prevents comparison of pathological characteristics of two different models or between malignant and benign lesions. Nevertheless, this was not the aim of the study since the difference between breast cancers and benign lesions has already been shown [13].

The results of this study may not be directly transposable to human breast tumour tissues. Indeed, the selected xenograft was implanted under the skin. Chang et al. showed that in humans, the breast thickness at the location of the tumour may influence the elastography image quality of breast masses [14]. Peritumoural (around the tumour) inflammatory reaction may also distort elasticity image patterns. Furthermore, a central necrosis is also not commonly found in small human breast cancers [15] and is probably observed in our model due to being a xenograft.

3.4 Conclusion

The SSI technique was able to measure stiffness changes during tumour growth in a human breast cancer model implanted in mice, reflecting underlying pathological changes. Tumour elasticity values were very well correlated with the portion of necrosis and fibrosis during the growth phase.

The second phase of this study which intended to investigate the findings of the clinical study presented in Chapter 2 is still in process. Nonetheless, preliminary results showed that during the chemotherapy treatment, tumour size seemed to decrease and that median tumour elasticity over the entire population of mice did not show a marked trend before Week 4, when it started to decrease.

This *in vivo* pre-clinical study may set the basis for further pre-clinical studies in other tumour models, and clinical studies in humans aiming to correlate tissue elasticity to pathology.

The next chapter presents the outcome of another pre-clinical study in mice, whose aim was to use tumour elasticity and tumour size to evaluate the efficiency of an antivascular drug in ectopically and orthotopically implanted tumours.

References

[1] E. Marangoni, A. Vincent-Salomon, N. Auger, A. Degeorges, F. Assayag, P. de Cremoux et al., "A new model of patient tumour-derived breast cancer xenografts for preclinical assays", *Clin Cancer Res.*, Vol. 13, no. 13, pp. 3989-98, 2007.
[2] Nitta Y., Kawabe N., Hashimoto S., Harata M., Komura N., Kobayashi K., et al., "Liver stiffness measured by transient elastography correlates with fibrosis area in liver biopsy in patients with chronic hepatitis C", *Hepatol Res.*, 39(7), pp. 675-84, 2009.
[3] Bavu E, Gennisson JL, Couade M, et al. Noninvasive in vivo liver fibrosis evaluation using Supersonic Shear Imaging: a clinical study on 113 hepatitis c virus patients. Ultrasound in Med. & Biol., Vol. 37, No. 9, pp. 1361–1373, 2011.
[4] Mueller S., Millonig G., Sarovska L., Friedrich S., Reimann F. M., Pritsch M, et al., Increased liver stiffness in alcoholic liver disease: differentiating fibrosis from steatohepatitis. World J Gastroenterol. 2010 Feb 28;16(8):966-72.
[5] Palmeri M. L., Wang M. H., Rouze N. C., Abdelmalek M. F., Guy C. D., Moser B., et al., "Noninvasive evaluation of hepatic fibrosis using acoustic radiation force-based shear stiffness in patients with nonalcoholic fatty liver disease", *J Hepatol*, 55(3), pp. 666-672, 2011.
[6] Ziol M., Kettaneh A., Ganne-Carrie N., Barget N., Tengher-Barna I., Beaugrand M., "Relationships between fibrosis amounts assessed by morphometry and liver stiffness measurements in chronic hepatitis or steatohepatitis", *Eur. J. Gastroenterol Hepatol.*, 21(11), pp.1261-1268, 2009.
[7] Wojcinski S, Farrokh A., Weber S., Thomas A., Fischer T., Slowinski T, et al., " Multicenter study of ultrasound real-time tissue elastography in 779 cases for the assessment of breast lesions: improved diagnostic performance by combining the BI-RADS(R) - US classification system with sonoelastography". Ultraschall Med., 31(5), pp. 484-491, 2010.
[8] Leong L.C., Sim L.S., Lee Y.S., Ng F. C., Wan C. M., Fook-Chong S. M., et al., " A prospective study to compare the diagnostic performance of breast elastography versus conventional breast ultrasound", *Clin. Radiol.*, 65(11), pp. 887-894, 2010.
[9] J. Ophir, I. Cespedes, H. Ponnekanti, Y. Yazdi, X. Li. "Elastography: a quantitative method for imaging the elasticity of biological tissues". *Ultrasonic Imaging*, 13, pp. 111-134, 1991.
[10] Sandrin L., Catheline S., Tanter M., Hennequin X., Fink M., "Time-resolved pulsed elastography with ultrafast ultrasonic imaging", *Ultrason Imaging*. 21(4), pp. 259-721, 1999.
[11] Sandrin L., Tanter M., Catheline S., Fink M., " Shear modulus imaging with 2-D transient elastography", *IEEE Trans Ultrason Ferroelectr Freq Control*, 49(4), pp. 426-435, 2002.
[12] Wang Y., Orescanin M., Insana M. F., "In vivo measurement of the complex shear modulus of rat mammary tumors using shear wave imaging techniques", *Conf. Proc. IEEE Eng. Med. Biol. Soc*, pp. 29-32, 2010.
[13] Athanasiou A., Tardivon A., Tanter M., Sigal-Zafrani B., Bercoff J., Deffieux T., et al. "Breast lesions: quantitative elastography with supersonic shear imaging-preliminary results", Radiology, 256(1), pp. 297-303, 2010.
[14] Chang J. M., Moon W.K., Cho N., Kim S. J., "Breast mass evaluation: factors influencing the quality of US elastography", Radiology, 259(1), pp. 59-64, 2011.
[15] Yu L., Yang W., Cai X., Shi D., Fan Y., Lu H., "Centrally necrotizing carcinoma of the breast: clinicopathological analysis of 33 cases indicating its basal-like phenotype and poor prognosis", *Histopathology*. 57(2), pp.193-201, 2010.

4 Chapter 4. Characterization of ectopic and orthotopic colon carcinoma CT26 using Ultrasound and the Supersonic Shear Wave Imaging (SSI) technique.

4.1 Introduction

In Chapter 3, the feasibility of assessing the efficiency of a neo-adjuvant chemotherapy treatment by measuring the tumour volume and global elasticity by conventional Ultrasound (US) and the Supersonic Shear Wave Imaging (SSI) technique, respectively, was evaluated. In the present chapter, the idea was to evaluate the efficiency of a different type of anti-tumoural drug, one which attacks the tumour blood vessels called tumour-vascular disrupting agent or antivascular. Unlike the treatment by chemotherapy, whose efficiency can only be assessed after several weeks, antivascular drugs such as *combretastatin A4 phosphate (CA4P)*, cause an effect which becomes visible within a few days from the beginning of the treatment [1]. Hence, the question was raised as to whether tumour elasticity could be used to determine the efficiency of such an anti-angiogenic treatment earlier than tumour size does. Aiming to answer the question, a murine colon carcinoma model (CT26) that would better reflect the clinical colon carcinoma situation has been chosen. This model was selected based on recent histo-pathological studies which showed it to be very well vascularized (more strongly vascularized than the model used in Chapter 3) and express cellular adhesion molecules, important targets for anti-angiogenic therapies, due to being involved in the process of angiogenesis required for tumour growth, cell migration and metastasis [2]. Additionally, the architecture of the CT26 model makes the tumour difficult to treat [3]. The CT26 tumour fragments were ectopically (placed in the flank) and orthopically (placed in the colon) implanted in mice.

Colorectal cancer represents the third leading cancer in men and second in women worldwide with 1.2 million new cases identified in 2008, accounting for 608700 deaths in the same year, becoming the second cause of cancer mortality after lung cancer [4]. Therefore, it has become important to develop adapted models which could better reflect the human pathology in order to evaluate diagnostic methods and potential therapies.

While ectopically implanted models are frequently employed owing to the facility of their implantation, orthotopically implanted models are considered to better reflect the tumour physiological environment. In particular, significant differences between these two models have been found in the level of growth factors and nutrients available, and in the profile of tumour angiogenesis and metastasis [5]. Moreover, orthotopic tumours can metastasize into tissues, usually becoming spontaneously arising tumours [6]-[10]. Apart from the surgical

issue involved in the orthotopic implantation, the main inconvenient lies in the difficulty to measure the tumour volume by conventional measurement tools such as callipers. The volume is a key parameter when assessing the tumour response to experimental treatments. Moreover, an overestimation of the volume by calliper assessment in orthotopic models has been reported [11].

This chapter presents the results of an animal study, in which US and the SSI technique were employed to measure tumour volume and global elasticity, respectively. The goal was to monitor the evolution of the implanted CT26 carcinoma models from the 5^{th} day after the implantation until the end of the anti-angiogenic treatment.

4.2 Materials and Methods

4.2.1 CT26 tumour model

Wild type cells CT26 (CT26-wt) were employed. The CT26-wt cell line was originally obtained from an undifferentiated colon carcinoma chemically induced by N-nitroso-N-methylurethan [12], which was subsequently cloned to obtain the stable CT26 line. The cell line was purchased from American Type Culture Collection (ATCC, CRL-2638, LGC Standards, Molsheim-France) and cultured at 37 ºC in a 5% CO_2 humidified atmosphere in a Dulbecco's Modified Eagle Medium (DMEM, Gibco) containing 10% of bovine fetal serum (FBS, Gibco Life technologies), 100 µM of streptomycin and 100 U/ml of penicillin.

4.2.2 Histological tumour cellularity and Micro Vascular Density characterization

Histological analysis had been previously carried out on this particular type of human cancer tumour in order to quantify its cellularity and vascular density. In this previous study, six tumours were employed. Ten pictures were taken for each histological cut along the central-axial plane of the tumours. The masses were stained with PECAM-1 and hematoxylin as depicted in Fig 4.1(A) and Fig 4.1(B). the sections were similar for both models, with homogeneously dispersed cancer cells and vessels. Quantitative analysis of the histological sections allowed the determination of the microvascular density (MVD) Fig 4.1(C) and cellularity Fig 4.1(D) for both models. Ectopic models presented a quasi-stable MVD level ranging from 800 to 1100 vessels/mm^2 throughout the study. On the contrary, orthotopic models showed a very low MVD level compared to the ectopic ones following the implantation (476 ± 50 vessels/mm^2 on the fifth day), but increased rapidly thereafter to reach a MVD value of 968 ± 36 vessels/mm^2 on the eleventh day. Beyond day 11, ectopic and orthotopic tumours showed similar MVD values which did not vary significantly until the end of the twenty-first day of the study.

Cellularity decreased in both models between the fifth and the fifteenth day from 14.7 ± 1.0 x 10^3 to 13.6 ± 0.5 x 10^3 cells/mm^2 in the ectopic model and from 18.0 ± 1.3 x 10^3 to 12.6 ± 1.0 x 10^3 cells/mm^2 in the orthotopic model. Both models showed similar cellularity values which remained stable from the 11th to the 18th day. From the 18th day to the end of the study, cellularity drastically increased in both models.

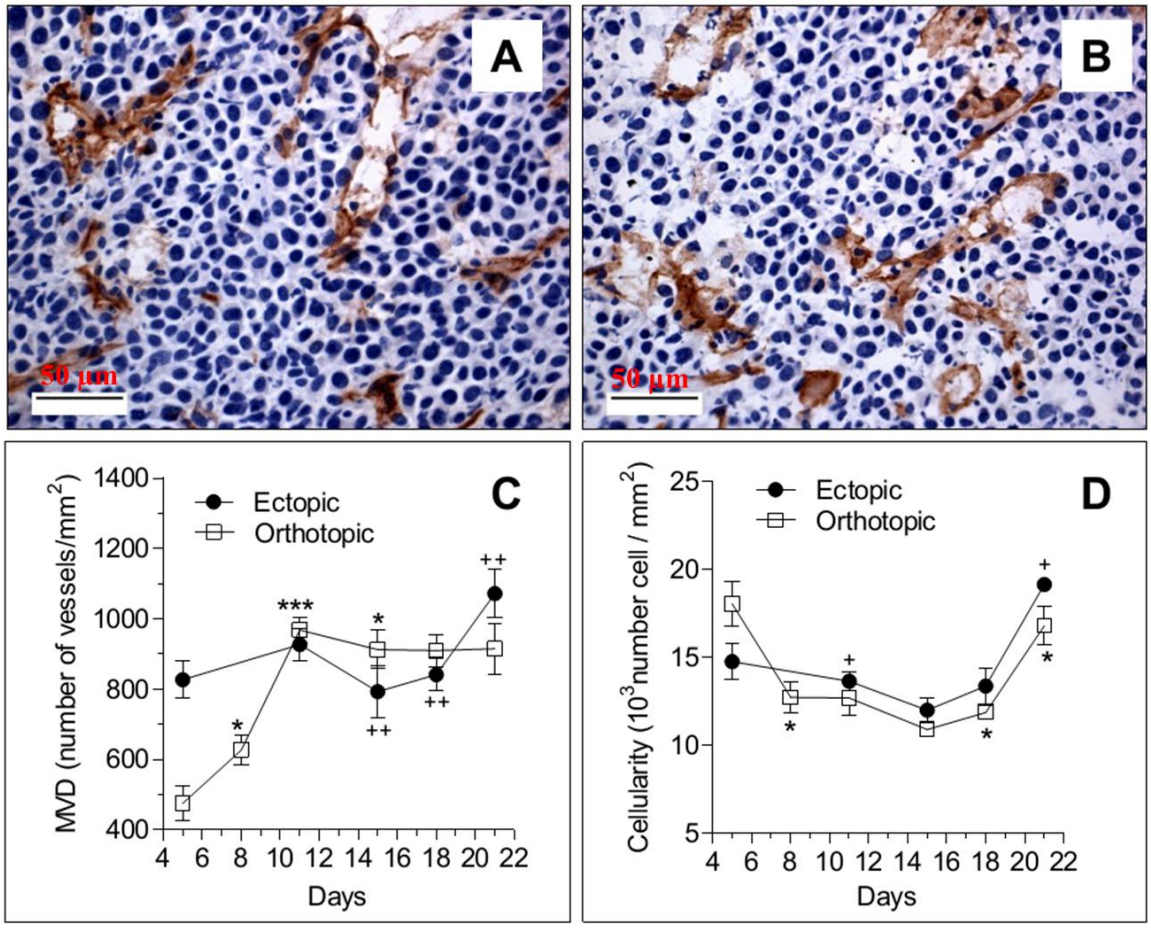

Fig 4.1. Histological characterization of cellularity and vascular density of CT26 tumours. Ten histological images obtained after immunohistochemistry of PECAM1 (positive staining in brown) and hematoxylin counterstain for ectopic (A) and orthotopic (B) masses 15 days after the implantation (x400 magnification). (C) Mean Microvascular density (MVD) (D) and mean cellularity are presented as a function of time.

4.2.3 Animals

The study was carried out on nude female mice (Janvier, St. Genest de Lisle-France) aged 6 to 7 weeks. The animal protocol was approved by the French Institutional ethics committee and the experiments were conducted according to French and European guidelines.

4.2.4 Ectopic tumour implantation

A mouse with a subcutaneous CT26 tumour was sacrificed. The mass was extracted, placed in a DMEM culture medium and cut into 20 to 30 mm^3 fragments. The fragments were placed in a sterile phosphate buffer saline and reinserted into the flank of six mice whose body had been previously disinfected with alcohol. For the CT26-wt line, the tumours were

implanted fortnightly with a 100% take rate. Fig 4.2 presents a representative ectopically and orthotopically implanted tumour fifteen days after the implantation. Thirty-eight (N = 38) tumours were ectopically implanted in the study.

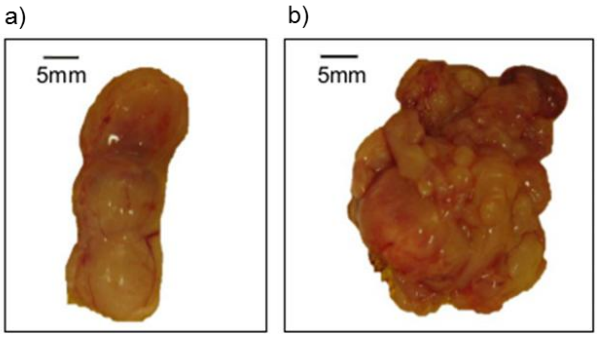

Fig 4.2. Photographs of representative CT26 tumours at the 15th day for the (a) ectopic and (b) orthotopic model.

4.2.5 Orthotopic tumour implantation

Allografts were prepared from ectopic tumours as explained above. Twenty (N = 20) tumours were orthotopically implanted as described by Tseng *et al.* [13]. Briefly, the animals were anesthetized and their abdomen shaved and disinfected with Betadine (Meda Pharma-France). Laparotomy was conducted to have access to the abdominal cavity. The tumour fragments were then sutured onto the caecum before the muscular tissue and the skin were stitched to finalize the implantation procedure (Fig 4.3).

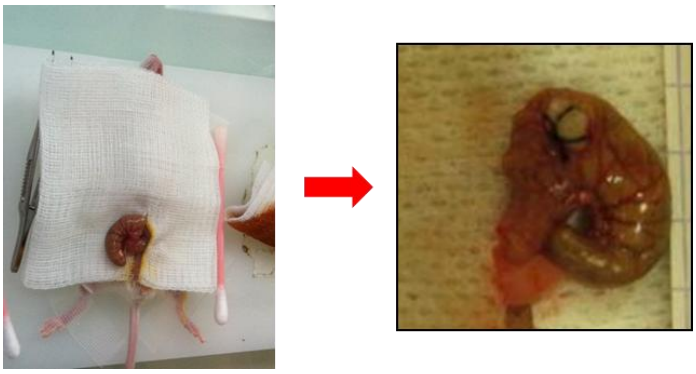

Fig 4.3. Orthotopic tumour implantation. The allografts were prepared as done for the ectopic implantation before being sutured onto the caecum.

4.2.6 Combretastatin A4 Phosfate treatment

Combretastatin A4 phosphate (CA4P) is a tumour vascular-targeting agent whose characteristics have been well documented [1][14] It attacks mainly the tumour blood vessels. From implantation, to the 12th post-implantation day, the entire group of mice were kept under the same conditions. As shown in Fig 4.1(C), the tumour vascularity reaches its peak eleven days after the implantation in both models. Thus, the antivascular treatment was intraperitoneally injected to eighteen (N=18) ectopically implanted tumours and thirteen (N=13) orthotopically implanted tumours in daily doses (100mg/kg) from the 12th to the 14th

day. Some of the ectopically (N=20) and orthotopically (N=7) implanted tumours were not treated in order to evaluate the evolution of the tumour elasticity and volume in untreated tumours. Therefore, the population of each model was classified into two different groups from the very beginning of the study: treated (Ca4P) and untreated (Control). Hence, four different group of mice were monitored: Ca4P Ectopic (Ca4P Ecto), Ca4P Orthotopic (Ca4P Ortho), Control Ectopic (Control Ecto) and Control Orthotopic (Control Ortho).

Fig 4.4 presents the complete planning of the study. US B-mode and elastography imaging were used to measure the tumour volume and their mean global elasticity, respectively. The aim was to study the feasibility of using elastography as a marker of the tumour development and tumour response to treatment. All the remaining animals were sacrificed once the study ended.

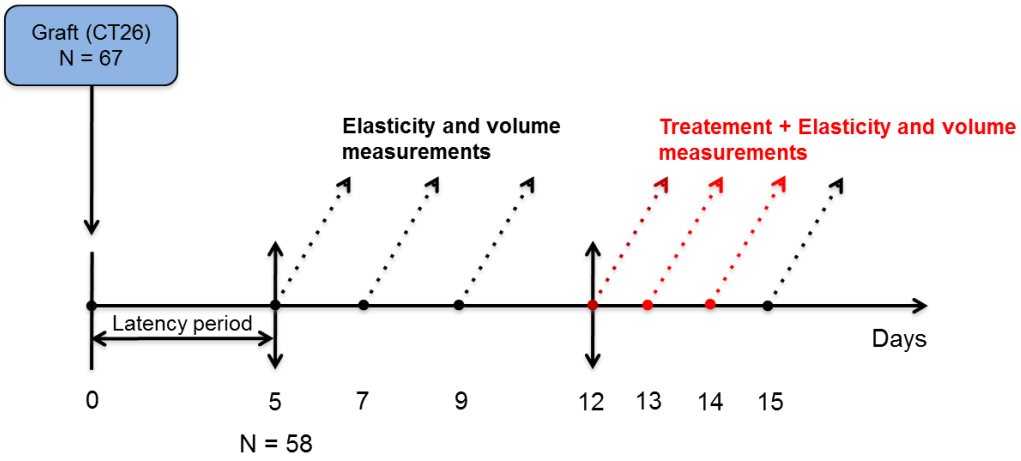

Fig 4.4. Protocol planning structure. After the end of the latency period, elasticity measurements were performed on the 5th, 7th, 9th, 12th,13th, 14th, and 15th day of the study. The antivascular treatment took place daily between the 12th to the 14th day . Initially, sixty-seven tumours (ectopic+orthotopic) were implanted. However, nine mice died before the end of the latency period because of the graft. Some additional mice died during the study or had to be sacrificed as their health had seriously deteriorated.

4.2.7 2D-US and the SSI technique

Measurements of the tumour volume and elasticity were performed every week once the five-day latency period ended (Fig 4.4). The duration of this period was chosen based on the histological tumour characterization presented in the Materials and Methods section of this chapter. B-mode and elastography images were acquired using a high frequency US probe (15 MHz, 256 elements, *Vermon, Tours-France*) driven by an ultrafast imaging device (*Aixplorer, Supersonic Imagine, Aix en Provence-France*). Before performing the acquisitions, the mice were shaved and anesthetized with a gas composed by 1.5% isoflurane (*Aerrane®; Baxter S.A.S, France*) and a mixture of oxygen (0.5 l/min) and air (1 l/min). Body temperature and breathing were controlled during the period that the animals remained sedated (Fig 4.5). B-mode images were acquired in the axial and sagittal imaging planes of the tumour in order to measure the tumour maximal diameters. Hence, three diameters (two in

the axial and one in the axial plane) were measured and the volume was calculated by using to the expression for the volume of an ellipsoid $v = \frac{\pi \times L \times W \times H}{3}$, where H, L and W stand for the lesion's height, length and width, respectively [11].

Fig 4.5. Mouse positioning. During the experiment, the animals were placed on a thermal-bed and covered with coupling gel after being anesthetized.

The SSI technique was used to measure the mean tumour elasticity. Elastography images were acquired along the central-sagittal and central-transversal planes of the tumours. The colour-bar was fixed between 0 and 40 kPa, with the pixels in black and red representing the lowest and highest elasticity values, respectively.

Fig 4.4 presents the measurement schedule. The volume and the elasticity measurements begun five days after the implantation (latency period) and were performed on the 5^{th}, 7^{th}, 9^{th}, 12^{th},13^{th}, 14^{th}, and 15^{th} day. The antivascular treatment took place daily between the 12^{th} to the 14^{th} day. The study was finalized on the 15^{th} day. Initially, sixty-seven grafts were performed in total (ectopic+orthotopic). Nevertheless, nine mice died before the end of the latency period because of the grafts. A few additional mice died during the study or had to be sacrificed as their health had seriously deteriorated.

4.2.8 *In vivo* calliper measurements

Measurement of the tumour dimensions were performed *in vivo* with a calliper to estimate the tumour volumes and compare them with the ones obtained by US. The tumour volumes were retrieved using the expression $v = \frac{L \times W^2}{2}$, where L and W represent the tumour length and width respectively [11][15]. The fact that the orthotopically implanted tumours were also palpable made it possible to use callipers to measure *in vivo* their maximal diameters. Nevertheless, the measurement errors in these kinds tumours were considerably higher than in the ectopically implanted ones, due to being located deeper within the body of the mice. Fig 4.6 depicts the mean tumour volumes measured *in vivo* with callipers and US imaging, on one group of mice composed by seven ectopically (*N=7*) and eight (*N=8*)

orthotopically implanted tumours. The mean values and their respective standard deviations (STD) were calculated over the population of both groups at each measurement time point.

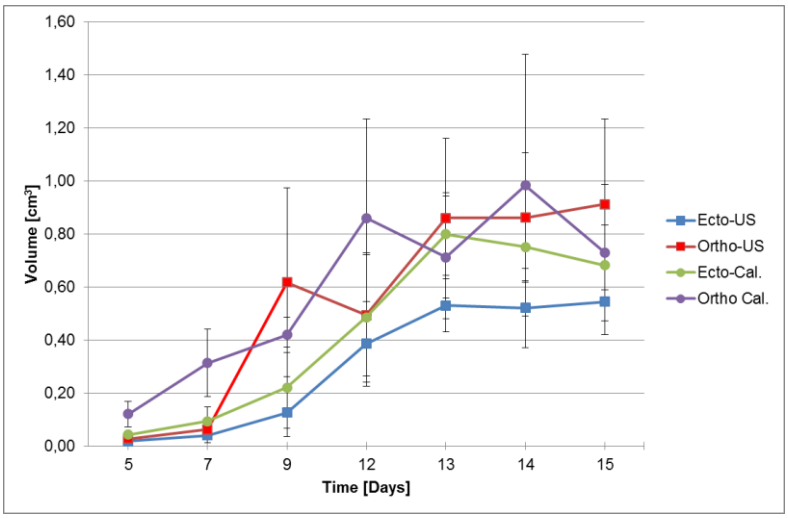

Fig 4.6. Mean tumour volumes for ectopically and orthotopically implanted tumours, calculated from the longitudinal in vivo measurements performed with two different methods: caliper and ultrasonic imaging. Measurement errors are much smaller in the US measurements than in the caliper ones as being stated in the literature [11].

4.2.9 Statistical analysis

Statistical Mann-Whitney tests were performed at each time measurement point in order to evaluate if the differences between the elasticity and the volume values of the treated and untreated groups were statistically significantly different. Mann-Whitney is a statistical test, which evaluates two data-sets assuming that they do not follow a Gaussian distribution (non-parametric test). The test gives a P value as a result. P values lower than 0.05 ($P < 0.05$) are considered as statistically significantly different.

4.3 Results

4.3.1 Measurement of the tumour volume and elasticity

4.3.1.1 Tumour volume

As depicted in Fig 4.6, the measurements of the tumour volume by conventional US are more accurate that the measurements with callipers. Therefore, only the measurements by US were employed to retrieve the volumes.

Three tumour maximal diameters (length, height and width) were measured by using conventional US imaging. Fig 4.7 depicts the measured diameters for one of the ectopic tumours at the 9^{th} day. The length and width were measured in the tumour axial plane (Fig 4.7(A)) whereas the width was measured in the sagittal plane (Fig 4.7(B)). The tumour volumes were subsequently assessed using these three measured diameters as stated in the Materials and Methods section.

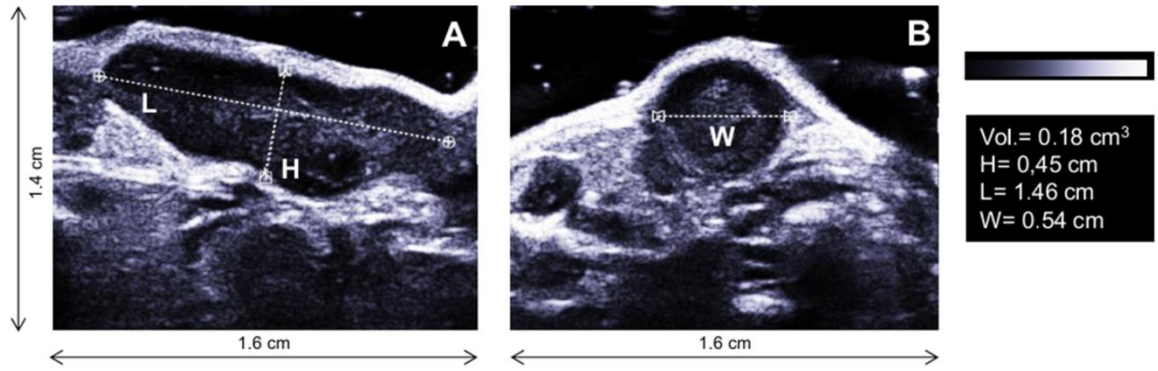

Fig 4.7. Tumour volume retrieval by conventional ultrasonic imaging. Tumour volume was calculated using the measured maximal diameters (length, height and width). The tumour length and height were measured in the axial plane of the tumour whereas the width was measured in the sagittal plane. The images correspond to one of the ectopic models on the 9th day.

Fig 4.8 contains representative images of the ectopic and orthotopic models at the 5th, 12th and 15th day. US imaging allowed the measurement of the lesion diameter as early as five days after the tumour implantation, with an average volume of 0.02 ± 0.01 cm^3 and 0.03 ± 0.02 cm^3 for the ectopic and orthotopic population at the 5th day, respectively. This allowed a rapid, accurate and non-invasive monitoring of the tumour volume.

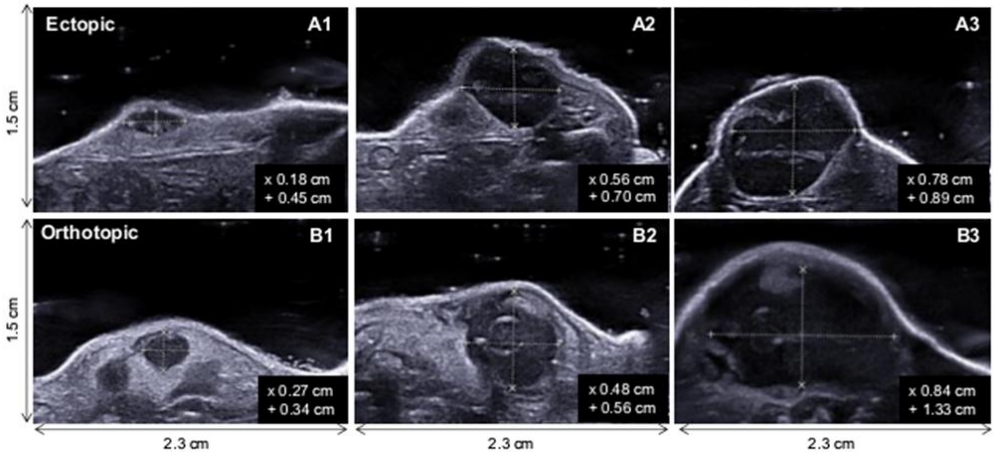

Fig 4.8. (Above) US longitudinal tumour volume monitoring. The tumour maximal diameters were measured in the axial and sagittal planes in order to retrieve the tumour volume. Representative images of one of the ectopic tumours on the 5th (A1), 12th (A2) and 15th (A3) day. (Below) Representative images of one of the orthotopic tumours on the 5th (B1), 12th (B2) and 15th (B3) day.

Table 4.1 and Fig 4.9 present the average volume for the entire population for both models from the 5th day until the end of the study (15th day). It is visible that from the implantation day, orthotopically implanted tumours grew more rapidly than the ectopically implanted ones, reaching higher volumes. For instance, at the 12th day (when the antivascular treatment begun) there was already an important size difference between the ectopically and orthopically implanted models: 0.34 ± 0.17 cm^3 (Ca4P Ecto), 0.28 ± 0.15 cm^3 (Control Ecto), 0.49 ± 0.19 cm^3 (Ca4P Ortho) and 0.75 ± 0.52 cm^3 (Control Ortho). The treated ectopic

tumour volumes (Fig 4.9(a)), which continuously increased from the implantation, slightly decreased between the 13th and the 14th day. Nevertheless, from the 14th day until the end of the study, the tumours went back to their growth trend, reaching an average volume of 0.47 ± 0.19 on the 15th day. Untreated ectopically implanted tumours showed a clear growth tendency throughout the entire study which became more marked from the 9th day, reaching an average volume of 1.65 ± 0.34 on the 15th day.

Table 4.1. Mean tumor volume values over the population of each of the four different mice groups (Ca4P Ecto, Control Ecto, Ca4P Ortho and Control Ortho) throughout the entire animal study. "N" under the column "Number of animals" represents the number of mice per group at the beginning of experiments. Nevertheless, some animals died or had to be sacrificed during the study. Thus, additional N were placed at some measurement days to indicate the number of animals present from that point of the study.

	Number of animals	*Volume [cm^3]*						
		Day 5	*Day 7*	*Day 9*	*Day 12*	*Day 13*	*Day 14*	*Day 15*
Ca4P Ecto	N=18	0.02 ± 0.01	0.04 ±0.02	0.12 ± 0.07	0.34 ± 0.17	0.43 ± 0.19 N = 17	0.38 ±0.18	0.47 ± 0.19
Control Ecto	N=20	0.02 ± 0.01	0.04 ± 0.02	0.07 ± 0.05	0.28 ± 0.15	0.43 ± 0.22	0.58 ± 0.23	1.65 ± 0.34 N = 17
Ca4P Ortho	N=13	0.04 ± 0.02	0.06 ± 0.03	0.41 ± 0.37	0.49 ± 0.19	0.73 ± 0.31	0.80 ± 0.25 N = 10	0.85 ± 0.32 N= 7
Control Ortho	N=7	0.02 ± 0.02	0.09 ± 0.06	0.12 ± 0.07	0.75 ± 0.52	1.04 ± 0.50	1.07 ± 0.50	1.19 ± 0.53

The volume of the treated and untreated orthotopically implanted tumours (Fig 4.9(b)), never stopped increasing from the implantation day, with the untreated tumours presenting a stronger growth tendency than the treated ones. On the 15th day, treated and untreated orthotopic models reached volumes of 0.85 ± 0.32 cm^3 and 1.19 ± 0.53 cm^3 respectively.

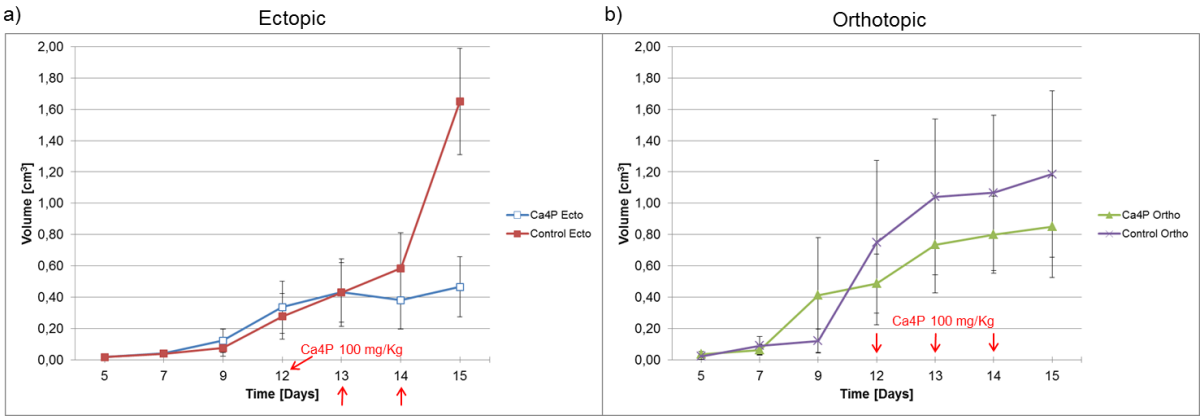

Fig 4.9. Tumour volume monitoring. Average volume of the entire the ectopic and orthotopic mouse population. The treatment by the antivascular took place on the days 12, 13 and 14 for both models. (a) In the treated ectopic models (Ca4P Ecto), the volumes grew continuously until the 15th day of the study. Only between the 13th and the 14th day, the volumes slightly decreased. The untreated ectopic tumours (Control Ecto) always presented a clear growth tendency, which became more evident from the 9th day until the end of the study. These tumours reached much higher values than the treated ones; (b) The treated (Ca4P Ortho) and untreated (Control Ortho) orthotopic tumours showed similar behaviors, growing continuously and reaching usually higher volumes than the ectopic ones. The untreated models became considerable larger than the treated ones.

4.3.1.2 Tumour elasticity

The SSI technique was employed to measure the tumours global elasticity from the 5th post-implantation day until the end of the study (15th day). Fig 4.10 depicts the tumour size and elasticity measurements for one of the ectopically implanted models. The mean tumour elasticity values for this particular tumour at the 5th, 9th and 12th day were 6.9 ± 3.1 kPa, 14.3 ± 5.1 kPa and 22.0 ± 13.6 kPa respectively.

Table 4.2 and Fig 4.11 present the mean elasticity values from the 5th day onwards for the entire ectopic (Fig 4.11(a)) and orthotopic (Fig 4.11(b)) population. The mean elasticity values of the treated and untreated ectopically implanted tumours increased continuously from the implantation until the 13th day, reaching mean elasticity values of 16.06 ± 5.39 kPa and 14.44 ± 6.80 kPa for the treated and untreated tumours respectively. Between the 13th and the 14th day, the elasticity of these tumours presented a slight decrement. However, from the 14th to the 15th day, the tumours became slightly harder, with mean elasticity values of 14.96 ± 4.24 kPa and 12.59 ± 8.67 kPa for the treated and untreated tumours respectively.

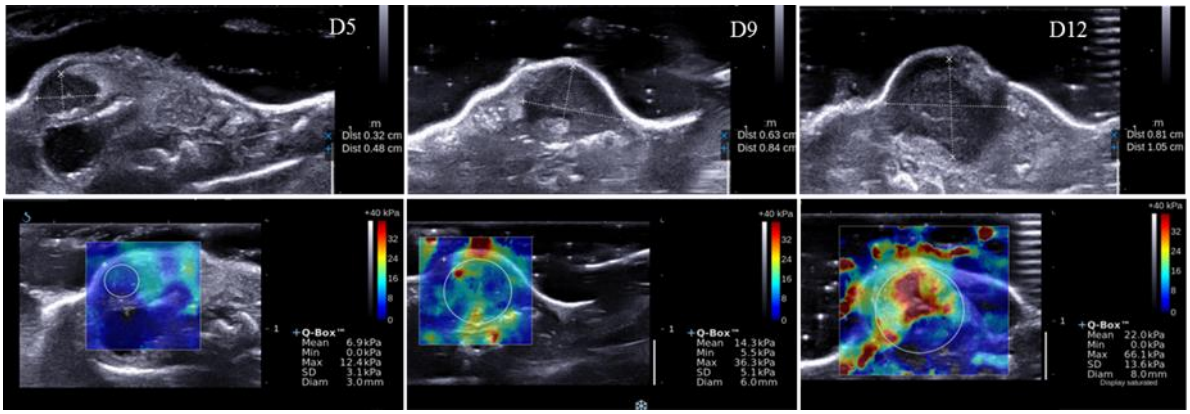

Fig 4.10. Tumour diameter measurement and the corresponding elastography image at the 5th, 9th and 12th day for one of the ectopic models. In this particular tumour, the global elasticity and the volume increased with time. As the tumour grew, it became more heterogeneous.

The orthotopically implanted tumours also presented a continuous elasticity increase which stopped between the 12th and the 13th day. On the 12th day, the tumours had mean global elasticity values of 19.07 ± 4.33 kPa and 18.57 ± 3.25 kPa for the treated and untreated tumours, respectively. The elasticity of the orthopically implanted tumours did not vary much between the 13th and the 15th day, with mean global elasticity values of 17.86 ±.4.18 kPa and 16.35 ± 2.42 kPa for the treated and untreated tumours. The treated and untreated orthotopically implanted tumours showed a similar growth trend and always had higher elasticity values than the ectopically implanted ones.

Table 4.2. Mean tumor elasticity values over the population of each of the four different mice groups (Ca4P Ecto, Control Ecto, Ca4P Ortho and Control Ortho) throughout the entire animal study.

	Elasticity [kPa]						
	Day 5	*Day 7*	*Day 9*	*Day 12*	*Day 13*	*Day 14*	*Day 15*
Ca4P Ecto	5.08 ± 1.78	8.87 ± 3.04	10.84 ± 2.85	14.30 ± 6.67	16.06 ± 5.39	14.23 ± 3.76	14.96 ± 4.24
Control Ecto	6.06 ± 1.92	8.77 ± 2.26	10.80 ± 3.53	12.42 ± 4.71	14.44 ± 6.80	12.14 ± 6.11	12.59 ± 8.67
Ca4P Ortho	7.11 ± 1.92	9.92 ± 2.15	13.27 ± 3.55	19.07 ± 4.33	17.05 ± 4.77	16.73 ± 5.09	17.86 ± 4.18
Control Ortho	8.89 ± 3.32	13.49 ± 3.23	16.75 ± 3.87	18.57 ± 3.25	15.12 ± 4.18	16.48 ± 2.50	16.35 ± 2.42

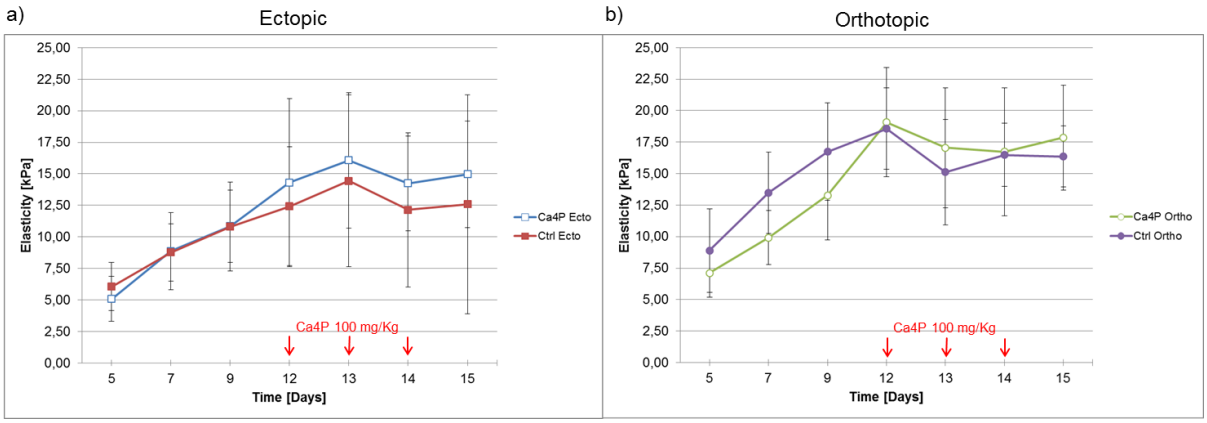

Fig 4.11. Tumour elasticity monitoring. Average tumour elasticity of the entire the ectopic and orthotopic mouse population. (a) In the treated (Ca4P Ecto) and untreated (Control Ecto) ectopic model, the elasticity increased continuously until the day 13. Between the 13th and the 14th day, the elasticity slightly decreased. However, from the 14th to the 15th day, the mean global elasticity values increased slightly in the treated and untreated tumours; (b) The treated (Ca4P Ortho) and untreated (Control Ortho) orthotopic tumours reached much higher elasticity values than the ectopic ones, presenting similar behaviors. The tumours grew continuously from the 5th until the 12th day. The mean global elasticity value at the 15th day did not differ much from that on the 12th day for both the treated and the untreated models.

Fig 4.12 shows the elasticity maps of two ectopically implanted tumours on the 14th day. Both untreated (a) and treated (b) tumours presented what a large necrotic center. The viable tissue (non-necrotic) was present only along the peripheral tumour ring. Histological analyses had not been yet performed on the mouse tissue samples when this manuscript was submitted for revision. However, the conclusion that treated and untreated tumours presented a vast central necrosis was based on the bibliography [16] and on previous histological studies performed on this xenograft by the researchers at the faculty of Pharmacy of *L'Universite Paris V Descartes.*

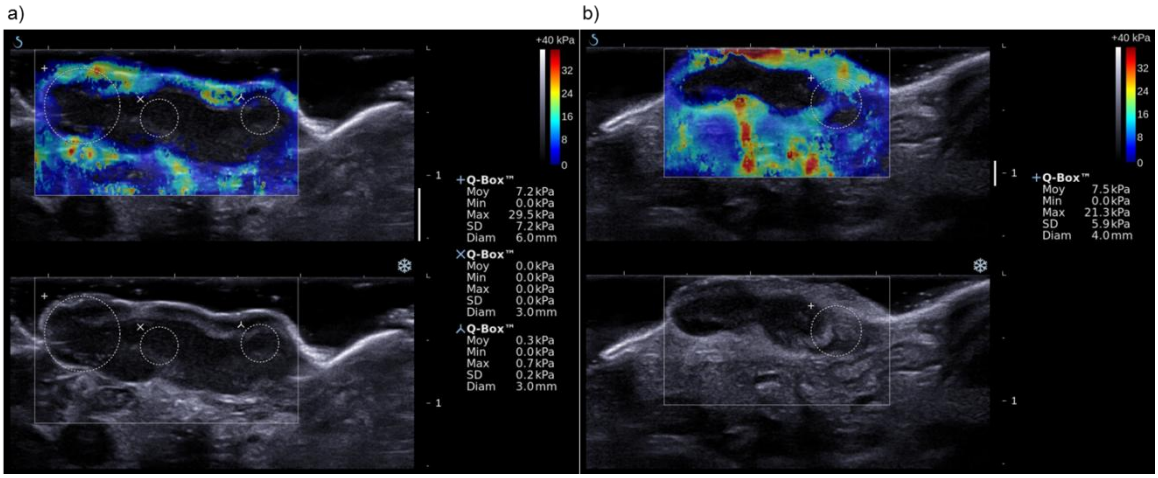

Fig 4.12. Elasticity measurement of two ectopically implanted tumours on the 14th day of the study; a) untreated and b) treated. Both tumours presented a vast central necrotic center. Viable tissue (non-necrotic) was only present along the peripheral ring.

Aiming to observe how the tumour elasticity and its vascular network reacted to the antivascular treatment, Doppler (standard Doppler fixed between 0 and 2 m/s) and elasticity measurements were performed on several mice on the 12th day after injecting the drug. The measurements were performed on the tumour immediately after the antivascular injection (t = 0) and 20 (t = 20), 40 (t = 40) and 60 (t = 60) minutes after the injection. Fig 4.13 depicts the evolution of the tumour elasticity (a) and of its vascular network (b) of a time scale in minutes. The elasticity within the tumour remained quasi-constant throughout the experience. The differences between the elasticity images taken at different times was negligible. On the contrary, a big difference could be appreciated on the Doppler images, which showed a gradual disappearance of the tumour blood vessels as time passed. Sixty minutes after the injection, almost all the blood vessels had been attacked and the blood flow stopped. The shear wave and the blood velocity were color-coded in scales ranging from 0 to 50 kPa and 0 to 2 m/s respectively.

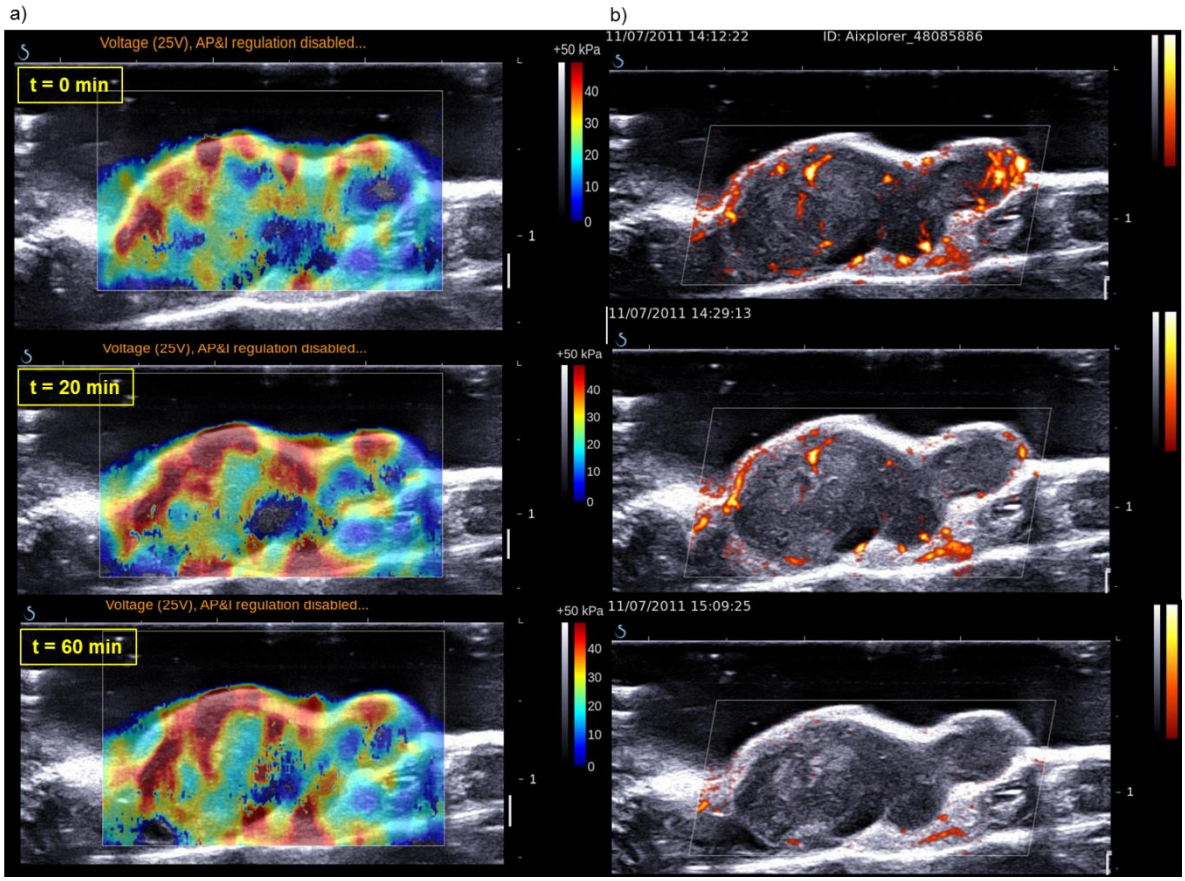

Fig 4.13. Evolution of the tumour elasticity and of the vascular network after the antivascular injection took place on the 12th day for a representative ectopic tumour. The shear wave and the blood velocity were color-coded in scales ranging from 0 to 50 kPa and 0 to 2 m/s respectively. (a) The tumour global elasticity remained almost constant throughout the experience, with no significant changes between t=0 and t=60 minutes; (b) The Doppler images show how the tumour blood vessels were attacked by the drug, cutting the blood flood within some minutes after the injection.

Table 4.3 contains the P values given by the Mann-Whitney test performed on the elasticity and volume data-sets, between the treated and untreated ectopically and orthotopically implanted tumours at each measurement time point. The test assumed a non-Gaussian data distribution. The confidence interval was set to 95%. Only the ectopic volumes at day 9, 14, and 15, the orthotopic volumes at day 9 and the orthotopic elasticity values at day 7 were found to be statistically significantly different.

Table 4.3. Mann-Whitney test at every measurement point. Comparisons were performed on the elasticity and volume datasets between the treated and untreated ectopically (Volume Ecto; Elasticity Ecto) and orthotopically (Volume Ortho; Elasticity Ortho) implanted tumors at each time measurement point. P values lower than 0.05 (*) indicate that the two compared groups of data are statistically significantly different.

	Day 5	*Day 7*	*Day 9*	*Day 12*	*Day 13*	*Day 14*	*Day 15*
Volume Ecto	0.98	0.80	0.03*	0.25	0.56	0.01*	0.03*
Volume Ortho	0.09	0.19	0.04*	0.47	0.25	0.09	0.13
Elasticity Ecto	0.18	0.66	0.75	0.55	0.33	0.19	0.12
Elasticity Ortho	0.40	0.02*	0.10	0.70	0.29	0.86	0.62

4.4 Discussion

Even though the orthotopic model has previously been described [17][18], the combination of US imaging techniques (conventional B-mode and SSI) for the tumour characterization had never been reported. US B-mode and the SSI technique allowed to follow-up the tumour changes in size and elasticity respectively from the 5th post-implantation day until the end of this preclinical study (15th day).

A difference between the tumour growth of the ectopic and orthotopic models was observed. Orthotopically implanted tumours grew faster than the ectopically implanted ones; a behaviour that has previously been described for human colon tumours implanted in nude mice [19] and for CT26 tumours [17]. Although there is some information on the tumour growth rate in the literature [20], very few attempts had been devoted to the precise characterization of these tumours.

The results of the experiments performed throughout this study, showed that treated ectopically and orthotopically implanted tumours presented a vast central necrosis which generally began from the 12th day. This effect, which has already been described in the literature [16], is typical of tumours treated with vascular disrupting agents (antivasculars) since they attack the blood vessels located in the core of the tumour. The vascular damage prevents the tumours from receiving all the oxygen and the nutrients necessary for growth and survival, and leads to an extensive necrosis, mainly within the core of the tumour, leaving viable tissue (non-necrotized) only at the peripheral rim. Nonetheless, the fact that the untreated ectopically and orthotopically implanted tumours also presented important necrotic areas (usually less extensive than those ones in the treated tumours), raised the question as to what caused the necrosis in the untreated tumours. It would be necessary to perform experiences with a higher number of untreated mice to be able to draw conclusions on that. It is not certain whether the necrosis was a consequence of the procedure followed during the tumour implantation or if was caused by the tumour internal architecture.

For the reasons just mentioned, the antivascular treatment dramatically affected the development of treated ectopically implanted tumours. Their slight shrinkage between the 13th and the 14th day was caused by the vascular damage which led to the central tumour necrosis. However, the fact that the blood vessels at the peripheral rim (which is usually the most vascularized part of the tumour) were not much affected by the treatment, allowed the transit towards the tumour core of the elements needed to regenerate the damaged central vascular network in order to continue growing. This phenomenon explains the growth between the 14th and the 15th day of the ectopically implanted tumours. The untreated ectopic tumours could grow freely as nothing prevented them from becoming larger, reaching an average volume which was four times larger than the average treated tumour volume at day 15. Unlike the

ectopic models, the orthotopic implanted tumours did not stop growing at any point in the study. It seems that the fact of being in their natural anatomical environment gave them higher resistance against the treatment, permitting them to be regularly fed and in constant growth. However, the growth of treated orthotopically implanted tumours was also affected by the antivascular as they showed a much smaller growth rate then the untreated tumours (Fig 4.9(b)).

The error-bars in the orthotopic volumes were higher than those of the ectopic volumes, reflecting the difficulty encountered when measuring the size of the orthotopically implanted tumours, as they are much more complicated to reach due to being localized within the abdominal cavity of the mice and be surrounded by other biological tissues. The size of the error-bars in all the presented measurements also show that although the study was performed on the same type of mice, which were kept under exactly the same conditions, their tumoural response could vary significantly from one to another.

Treated and untreated ectopic and orthotopic tumours presented a similar elasticity behaviour which was not much influenced by the treatment. The elasticity decrease between the 12^{th} and the 13^{th} day in the orthotopic model and between the 13^{th} and the 14^{th} day in the ectopic model may have been probably caused by the inner tumour necrosis. The slight elasticity increment from the 13^{th} and the 14^{th} day for orthotopic and ectopic tumours respectively, may have been a consequence of a minor elastic increment of the peripheral tumour ring, which contrary to the central tumour zone, did not necrotize. Moreover, histological analyses on the tissue samples will be needed to support such assumptions. Due to the localization of the orthotopically implanted tumours and the central necrosis, the elasticity measurements became more difficult to perform as in some cases the shear waves were not able to penetrate the tumour to cover the entire tumour area.

According to previous histological results, the MVD values were significantly lower for the orthotopic model in the early time points as compared to the ectopic model. These data may indicate that the orthotopically implanted CT26 tumour fragments probably needed some time to adapt to their new caecal microenvironment. This information could be of great importance considering that the angiogenic phase of orthotopic tumours requires more time to develop as compared to the ectopic model, which indicates that orthotopic implantation would be more appropriate for evaluating the efficiency of antiangiogenic experimental therapies. In addition to this, data from the previous studies showed that in both models, the MVD value seemed to reach its maximum at the 11^{th} day.

US imaging allowed tumour volume estimation for both implantation models. It has been previously shown that US imaging yield more precise volume measurement data as compared to calliper measurements [11], due to the latter being very operator dependant and

measurement errors (which are frequently in the range of 27% [21]) may bias the volume calculations.

The fact that two data-sets are found to be non-statistically significantly different does not mean they are equal. It means there is not enough basis to affirm whether they are significantly different or not. In some cases, by looking at Fig 4.9 and Fig 4.11, one could have had the visual impression that two volume or elasticity data-sets were significantly different. However, the exhaustive analysis performed by Mann-Whitney test was not able to conclude on it.

4.5 Conclusion

This study evaluated the feasibility of using 2D-US and the SSI technique to monitor the evolution of tumour growth and global elasticity, in response to antivascular treatment of orthotopically and ectopically implanted CT26 colon carcinomas in mice. Apparently, the antivascular treatment caused an effect on tumour growth and on the tumours' vascular network. Nonetheless, its impact on the tumour global elasticity was not strong. Nevertheless, in order to be able to draw solid conclusions on the effects of antivascular therapy on tumour size and elasticity, it would be necessary to perform histological analyses on the tumour tissue samples and additional animal studies with different drug types and doses. In addition to this, the study should last longer and the treatment should begin earlier. Performing histo-pathological measurements and Doppler imaging could be of great utility to better understand the impact on the antivascular treatment on the tumour elasticity.

It was easier to monitor the ectopically implanted tumours than the orthopically implanted ones, since the latter were localized within the mice abdominal cavity and surrounded by other biological tissues.

From the beginning of this report, only elasticity and tumour volume have been the parameters used for tumour characterization. However, there exist other parameters such as nonlinearity, which would offer new and valuable information on tumour characteristics. The next chapter shows the potential of a third order nonlinearity parameter for tumour characterization.

References

[1] E. El-Emir, G. M. Boxer, I. A. Petrie *et al.*, "Tumour parameters affected by combretastatin A-4 phosphate therapy in a human colorectal xenograft model in nude mice", *Eur. J. Cancer*, 41(5), pp. 799-806, 2005.
[2] J. Seguin, C. Nicolazzi, N. Mignet, D. Scherman, and G. G. Chabot, "Vascular density and endothelial cell expression of integrin alpha v beta 3 and E-selectin in murine tumours", Tumor Biol., May 2012.
[3] L. Polin, T.H. Corbett, B.J. Roberts, *et al*., "Transplantable syngeneic rodent tumors: Solid tumors of mice. In Teicher BA, ed. Tumors models in cancer research, Cancer Drugs Discovery and Development", *Second ed.New York, Springer Science & Business Media LLC*, pp. 43-78, 2011.
[4] Jatistics. *CA Cancer J Clin*, 61, pp.69-90, 2011.
[5] M. W. Heijstek, O. Kranenburg, I. H. Borel Rinkes, "Mouse models of colorectal cancer and liver metastases", *Dig Surg*; 22**,** pp. 16-25, 2005.

[6] H. Kashtan, M. Rabau, J.B. Mullen *et al.*, "Intra-rectal injection of tumour cells: a novel animal model of rectal cancer", *Surg Oncol*, 1, pp. 251-256, 1992.
[7] R. Giavazzi, D.E. Campbell, J.M. Jessup, K. Cleary, I.J. Fidler, "Metastatic behaviour of tumour cells isolated from primary and metastatic human colorectal carcinomas implanted into different sites in nude mice", *Cancer Res*., 46, pp. 1928-1933, 1986.
[8] T. Kubota, "Metastatic models of human cancer xenografted in the nude mouse: the importance of orthotopic transplantation", *J Cell Biochem*, 56, pp. 4-8, 1994.
[9] R. S Bresalier, E. S. Hujanen, S. E. Raper *et al*., "An animal model for colon cancer metastasis: establishment and characterization of murine cell lines with enhanced liver-metastasizing ability", *Cancer Res.*,47, pp. 1398-1406, 1987.
[10] M. Pocard, H. Tsukui, R. J. Salmon, B. Dutrillaux, M. F. Poupon, "Efficiency of orthotopic xenograft models for human colon cancers i*n vivo",* 10, pp. 463-469, 1996.
[11] A. M. Cheung, A. S. Brown, L. A. Hastie *et al.*, "Three-dimensional ultrasound biomicroscopy for xenograft growth analysis", *Ultrasound Med Biol*, 31, pp. 865-870, 2005.
[12] T. H. Corbett, D. P. Griswold, B. J. Roberts, J. C. Peckham, F. M. Schabel, "Jr. Tumor induction relationships in development of transplantable cancers of the colon in mice for chemotherapy assays, with a note on carcinogen structure", *Cancer Res.*,35, pp. 2434-2439, 1975.
[13] W. Tseng, X. Leong, E. Engleman, "Orthotopic mouse model of colorectal cancer", 484, *J Vis Exp* 2007.
[14] G. M. Tozer, C. Kathou ,B. C. Baguley, "Disrupting tumour blood vessels", *Nat. Rev. Cancer*, 5(6), pp. 423-435, 2005.
[15] M.M Tomayko, C.P Reynolds, "Determination of subcutaneous tumor size in athymic (nude) mice". *Cancer Chemother Pharmacol*, 24, pp. 148-154, 1989.
[16] M. J. McKeage, and B. C. Baguley, "Disrupting Established Tumor Blood Vessels-Review Article", *Cancer*, 116, pp. 1859-1871, 2010.
[17] Y. Chen, K. J. Chang, L. H. Hwang, C. N. Chen, S. H. Tseng, "Establishment and characterization of a rectal cancer model in mice: application to cytokine gene therapy", *Int J Colorectal Dis*, 17, pp. 388-395, 2002.
[18] J. Dong, J. Yang, M.Q. Chen *et al*., "A comparative study of gene vaccines encoding different extracellular domains of the vascular endothelial growth factor receptor 2 in the mouse model of colon adenocarcinoma CT-26", *Cancer Biol Ther*;.7, pp. 502-509, 2008.
[19] M. Pocard, H. Tsukui, R. J. Salmon, B. Dutrillaux, M. F. Poupon, "Efficiency of orthotopic xenograft models for human colon cancers i*n vivo",* 10, pp. 463-469, 1996.
[20] M. G. Brattain, J. Strobel-Stevens, D. Fine, M. Webb, A. M. Sarrif, "Establishment of mouse colonic carcinoma cell lines with different metastatic properties", *Cancer Res.*,40, pp. 2142-2146, 1980.
[21] D.M. Euhus, C. Hudd, M.C. LaRegina, F.E. Johnson, "Tumor measurement in the nude mouse", *J Surg. Oncol.*, 31, pp. 229-234, 1986.

5. Chapter 5. Nonlinear shear elastic parameter quantification

5.1 Introduction

As it has been shown throughout this report, the measurement of the tissue elasticity may not be sufficient to monitor the effects of an anti-cancerous treatments such as chemotherapy and antivascular therapy for breast and colon carcinomas. Therefore, it becomes vital to study new additional parameters which allow a better characterization of therapeutic changes. This chapter presents a method employed to quantify a third-order tissue nonlinearity parameter. Such a parameter, which could play a key role in monitoring of tumour growth, would be of great utility to understand the processes involved in the development of cancerous tumours. This section contains the theoretical development of this new tissue parameter and presents its potential for *in vivo* clinical application.

For almost two decades, several dynamic elastography techniques have been developed based upon ultrasound (US) methods [1]-[6] to excite tissue and measure its response to the mechanical stress. Methods such as sonoelastography [1], vibroacoustography [4], acoustic radiation force [5], supersonic shear wave imaging[6] and transient elastography [7] have shown their efficiency to determine elastic properties of biological soft tissues. Nevertheless, most of these techniques have been concentrated on the estimation of the second order elastic modulus (μ). In order to better understand pathologies, since the knowledge of the shear elasticity may not be sufficient in all cases to emit a accurate clinical diagnosis, new refinements were developed to study other tissue mechanical properties such as viscosity [4][8], anisotropy [9] and shear nonlinearity [10].The relevancy of these parameters is currently studied in pre-clinical and clinical studies, ranging from musculoskeletal imaging [9][11], cardiac [12][13] and vascular [13] applications to liver fibrosis staging [14].

Several research groups are currently working on nonlinear elasticity imaging. Indeed, recent data from *ex vivo* measurements of breast and prostate tissue indicate that in addition to the linear properties, nonlinear elastic properties may be useful for differentiating benign from malignant tumors [15][16]. The most advanced nonlinear elastic imaging, which utilizes the strain/stress relationship to retrieve the nonlinear shear modulus is the quasi-static US based elastography [17]-[19]. However, this approach represents a major challenge as it may require compressive strains greater than 10% [20]. The key idea is based on *ex vivo* tests conducted by Krouskop *et al.*[15] , which pointed out that at smaller strains, the departure from linearity for most tissue types is minimal [15]. Once the displacements at these large strains have been measured, an inverse problem must be solved in order to determine the tissue nonlinear elastic parameters. However, both issues, i.e. the estimation of tissue displacements at large strains

and the solving of the nonlinear elastic inverse problem, remain challenging problems today [20][21]. Oberai *et al.* [20] proposed interesting solutions to these complex issues in 2009 and provided the first clinical images of the nonlinear elastic parameter. Nonetheless, the low qualities of the images emphasize the high complexity of solving this nonlinear inverse problem.

In this chapter, we propose to use a completely different approach based on the combination of the acoustoelasticity theory with Transient Elastography. Transient elastography is one of the most efficient techniques as it allows to image the shear wave propagation in soft media by using ultrafast US scanners and to quantify the medium shear modulus in real time. Based on this method, there are at least three possible ways to quantify shear non linearity: nonlinear interaction between shear waves of different frequencies [22], finite amplitude shear wave propagation [23] and acoustoelasticity [24]. Experimentally, acoustoelasticity consists in measuring the speed of acoustic waves in stressed solids. The third order elastic modulus is deduced from the slope of the ultrasonic wave velocities as a function of the uniaxial stress applied to the sample [24].

The first acoustoelasticity theory in solids was developed by Hugues and Kelly [25] using the second and third order elastic coefficients. Recently, combining the new ideas of shear wave propagation in quasi incompressible soft solids [26][27] and the acoustoelasticity theory, new expressions for the shear wave propagation in uniaxial stressed media have been defined [24]. Gennisson *et al.* [24] proposed to use the shear imaging technique [6] to estimate the third order elastic modulus (A) by measuring the shear wave speed along different directions in a medium submitted to an uniaxial stress. In these experiments, the main difficulty was to control the uniaxial stress within the medium. The local stress was approximated to the applied stress on the surface, which was easily quantifiable in the proposed setup. Unfortunately, as shear wave propagation had to be imaged along the three different axis of the referential frame, this technique was not applicable in clinical practice.

This chapter proposes a much more reliable approach as it provides a way to quantify the locally applied uniaxial stress deep in tissues, and to perform the entire experiment using a conventional ultrasonic probe located at the surface of the investigated organ, thus enabling *in vivo* investigations. The key idea consists in combining the supersonic shear imaging (SSI) technique to quantify the shear modulus and Static Elastography (SE) to quantify the locally applied uniaxial strain in the imaging plane. From both estimates, one can derive the local uniaxial stress at each compression step. Static elastography has been developed over the past two decades [28]-[34]. This technique allows to estimate the strain (ε) linked to the elasticity via Hooke's law ($\sigma = E.\varepsilon$, where σ is the applied stress and E is the Young's modulus) in a medium submitted to a small uniaxial compression. Local strains are derived from the

ultrasonic backscattered signals before and after compression by using cross-correlation analysis. Then, knowing the elastic modulus estimated through dynamic elastography (SSI) and the strain through static elastography, a quantitative map of the local stress is recovered. Finally, a quantitative map of the nonlinear shear modulus (*A*) is calculated by applying the acoustoelasticity theory in quasi-incompressible soft solids, correlating the stress to the shear wave speed.

In this chapter, the acoustoelasticity theory in quasi-incompressible soft solids is presented in the first section to deduce the nonlinear shear coefficient *A*. Then, the experimental set-up for both the SSI and the static elastography techniques is depicted and explained. In the next section, the experimental results are described and compared with the simulation results. Several agar-gelatin (AG) tissue mimicking phantoms often used in medical imaging and *ex vivo* beef liver samples were tested. One of the phantoms contained an inclusion softer than the surrounding media, whereas the second phantom an inclusion harder than its surrounding material. The liver samples came from the same animal liver and were randomly chosen within the organ. Finally, the experimental assessments of the nonlinear shear coefficient are discussed.

5.2 Materials and Methods

5.2.1 Acoustoelasticity theory

The general principle of acoustoelasticity is based on the expression of the elastic wave speed in uniaxially stressed lossless solids. Basic equations are summarized as follows: in "Lagrangian" coordinates (*a*, *t*), where *a* is the equilibrium position of the particle and *t* is the time; the equation of motion is given by:

$$\rho_0 \frac{\partial^2 u_i}{\partial t^2} = \frac{\partial^2 e}{\partial a_j \partial (\frac{\partial u_i}{\partial a_j})} \qquad \text{Eq. 1}$$

where ρ_0, u, e designate respectively the density, the total displacement and the strain energy density which can be developed up to the third order in quasi-incompressible soft solid as follows [26]:

$$e = \mu I_2 + \frac{A}{3} I_3 + D I_2^2 \qquad \text{Eq. 2}$$

with μ the shear modulus (Lamé coefficient) involved in the linear behavior of the solid, *A* the third order elastic coefficient describing the quadratic nonlinear shear response of the deformed solid and *D* the fourth order elastic constant. I_2, I_3 are invariants of the Lagrangian

strain tensor defined by Landau and Lifshitz [35]. To simplify the calculations, only the propagation of shear waves of small amplitude (*i.e.* in the linear regime) is considered, thus enabling to neglect the fourth order terms.

Due to the nature of the applied uniaxial stress and the elasticity imaging technique, two kinds of displacements are involved in the calculation of the equation of motion: the displacement due to the quasi-static compressions (u^S) and the displacement due to the shear wave propagation (or induced by the acoustic radiation force) (u^D). Moreover, the magnitude of the shear displacements (µm) are of very small magnitude compared to the displacement due to the uni-axial stress (σ). Hence, the total displacement can be expressed as the sum of u^D and u^S as follows:

$$u^{Tot} = u^D + u^S \qquad \text{Eq. 3}$$

The entire calculation process of the nonlinear elastodynamic equation was carried out in Gennisson *et al.* [24]. Here, depending on the axis of polarization and the axis of the shear wave propagation, a nonlinear elastodynamic equation was deduced for each of the three possible scenarios (Fig 5.1):

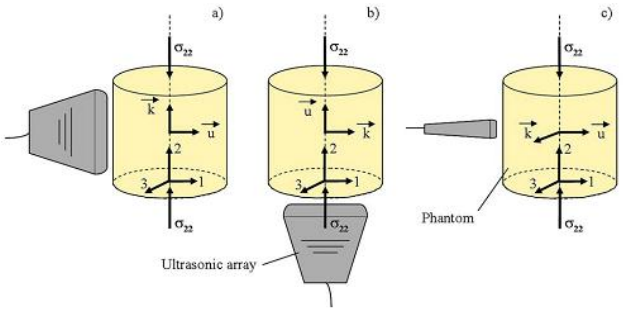

Fig 5.1. The three possible configurations for the generation (by acoustic radiation force) and detection (with an ultrafast scanner) of polarized shear waves in a medium submitted to uniaxial stress (σ). a) scenario governed by Eq. 4; b) scenario governed by Eq. 5; c) scenario governed by Eq. 6 [24]. The vectors u and k represent respectively, the axis of polarization and the axis of propagation of the generated shear wave.

For the sake of simplicity, the plane shear wave is denoted by two indices (12, 21 and 13). The first and the second index correspond to the axes of the shear wave polarization and the axis of the shear wave propagation, respectively. V_S represents the shear wave velocity, µ the medium shear modulus at a given compression, ρ_0 the medium density under zero stress (σ_{22} = 0) and *A* the third order nonlinear parameter, which is retrieved by experimentally measuring the shear wave speed (using the SSI technique) as a function of the stress applied (using the SE technique) at each compression step.

It is to observe that Eq. 4, Eq. 5 and Eq.6 correspond to the classical shear wave propagation equation in an isotropic media if the medium is unstressed (σ_{22} = 0) (Eq. 7).

$$\rho_0 V_{S12}^2 = \mu - \sigma_{22}\left(1 + \frac{A}{12\mu}\right) \quad \text{Eq. 4}$$

$$\rho_0 V_{S21}^2 = \mu - \sigma_{22}\left(\frac{A}{12\mu}\right) \quad \text{Eq. 5}$$

$$\rho_0 V_{S13}^2 = \mu - \sigma_{22}\left(1 + \frac{A}{6\mu}\right) \quad \text{Eq. 6}$$

$$\mu = \rho . V_s^2 \quad \text{Eq. 7}$$

Taking into account that the axis of polarization and the shear wave propagation are, respectively, parallel and perpendicular to the axis of compression (uniaxial stress (σ)), the nonlinear shear coefficient was retrieved by using Eq. 5.

5.2.2 Experimental Setup

All the experiments presented in this paper were carried out using the same setup presented in Fig 5.2, which includes a conventional ultrasound probe (SL15-4, 256 elements, 8 MHz central frequency, *Supersonic Imagine*, Aix en Provence, France) driven by a fully programmable ultrafast imaging device comprising 256 transmit/receive channels (*Aixplorer, Supersonic Imagine*, Aix en provence, France). A mechanical actuator was used to axially displace the probe and the compressor plate attached to it. The measurements were performed on agar-gelatin (AG) tissue mimicking phantoms which were prepared following the procedure presented in [36]. Each phantom contained a cylindrical inclusion with a diameter of 10 mm. The medium surrounding the inclusions had 2% by weight of agar and 5% by weight of gelatin. The Soft inclusions had a concentration of 2% by weight of agar and 3% by weight of gelatin whereas the hard inclusions had a concentration of 2% by weight of agar and 8% by weight of gelatin. Throughout this chapter we will refer to the media surrounding the inclusions as “the medium” and the inner part of the inclusions as “the inclusion”. The phantoms were placed over a still and uniform plane surface. The quasi-static stress was applied at the top of the phantoms by axially displacing the probe and the compressor plate in steps of 0.1 mm (≈ 0.33% with each step lasting less than 30s). The stress distribution within the phantoms at each compression step was quasi-constant and did not vary with time (measurements were also performed at 1 min, 2 min and 3 min to confirm this hypothesis). Neither displacements nor the strains changed at any time after the compression steps. Before beginning the experiments, a certain amount of compression was applied in order to ensure all the probe elements were in full contact with the phantom surface and therefore have an optimal probe-phantom coupling. Nevertheless, it was not possible to have exactly the same

amount of pre-compression for each phantom since they were not geometrically identical although they were made using the same mold.

The imaging plane was placed perpendicularly to the inclusions' axis in the middle of the phantom. The phantoms (103 x 31 x 74 mm^3) were considered axially-symmetric (along the central axis of the cylindrical inclusion (y-axis)), which allowed us to neglect the non-axial (lateral and out of plane) components of the displacement due to compression. At each compression step, the medium displacement and the shear wave speed were quantified by using the SE and the SSI technique respectively. This procedure allowed to quantify displacements, strains, stresses and nonlinear shear modulus maps.

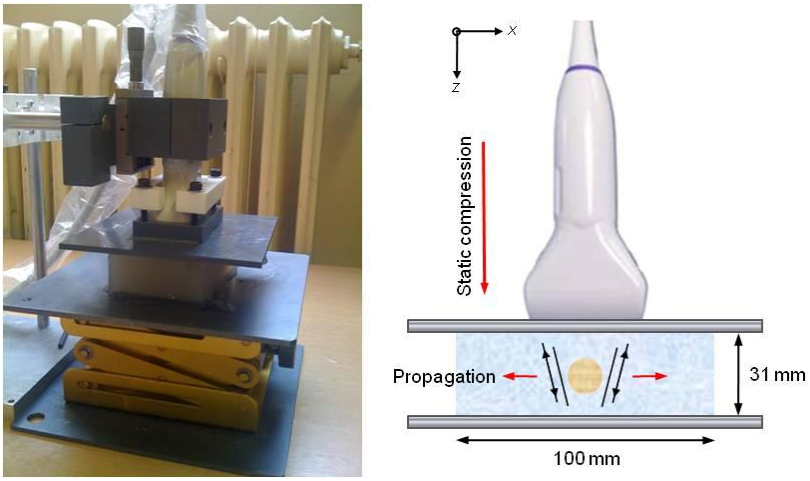

Fig 5.2. Measurement setup. The ultrasonic probe, a compressor plate and an actuator were held perpendicularly to the phantom by a support.

5.2.3 Imaging techniques and finite element simulation

The dynamic and static elastography experiments were performed simultaneously. The entire procedure can be summarized as follows (Fig 5.3):

1. A conventional US image of the phantom is acquired before compression (pre-compression image), which is later used as a reference to calculate the medium displacement when compared with a second US image acquired after compression (post-compression image).
2. The SSI technique is used to retrieve the complete shear velocity map and therefore the 2D shear modulus map of the medium.
3. A 0.1 mm displacement is applied to the phantom along the axial plane, corresponding to a strain step ($\Delta\varepsilon$).
4. A conventional US image is acquired (post-compression image) which is cross-correlated with the one obtained at 1.

The previous procedure was followed at each compression step. The axial displacements were small enough to minimize the negative effects of signal decorrelation

caused by larger compressions. The total static strain (ε_{SE}) corresponds to the summation of the static strain at each static compression step ($\Delta\varepsilon$) (Eq. 8), where *N* represents the number of compression steps.

$$\varepsilon_{SE} = \sum_{i=1}^{N} \Delta\varepsilon \qquad \text{Eq. 8}$$

Coupling gel was placed on the bottom and the top of the phantoms to minimize the friction effects between the phantoms and their supports.

5.2.3.1 Shear modulus computation using the Supersonic Shear Imaging technique

The SSI technique, which was explained in the first chapter, allows the retrieval of the local shear wave velocity and therefore the calculation of the medium shear modulus through Eq. 7 at each compression step.

5.2.3.2 Displacement and Strain maps computation using the static elastography technique

In order to retrieve the displacement induced by the compression, the static elastography technique developed by Ophir *et al.* [28] was used. As mentioned before, the probe and the compression plate were placed on the top of each phantom to apply quasi-static compression steps of 0.1 mm along the axial plane up to 6 mm of absolute axial displacement for the soft and hard inclusion phantoms. The changes in the ultrasonic pre and post compression echo signals correlates with local tissue axial displacements through the cross-correlation between successive B-scans. The 2D strain field (ε) was computed as the first derivative of the displacement field *D* along the axial plane (z-axis) (Eq. 5).

$$\Delta\varepsilon = \frac{dD}{dZ} \qquad \text{Eq. 9}$$

5.2.3.3 Stress computation combining static elastography and SSI measurements

The differentially applied stress Δσ was retrieved through the simplified form of Hooke's equation (Eq. 10). This allowed the direct computation of the stress from the measurement of the material's Young's modulus $E(\sigma)$ and strain $\Delta\varepsilon$ at each compression step by means of dynamic and static elastography respectively.

$$\Delta\sigma = E(\sigma).\Delta\varepsilon \qquad \text{Eq. 10}$$

Then, the cumulative stress was calculated by applying a simple integral over *N* acquisition steps (Eq.7).

$$\sigma = \sum_{i=1}^{N} \Delta\sigma \qquad \text{Eq. 11}$$

5.2.3.4 Nonlinear shear modulus (A) calculation

Due to the combination of the SE and the SSI techniques, the evolution of the local shear wave speed $Vs(\varepsilon_{SE})$ as a function of the uniaxial stress could be estimated for each pixel on the imaging plane. Then, using (Eq. 5), the slope of the linear behavior of the shear modulus as a function of the applied stress gives directly the nonlinear shear modulus *A*. At last, a 2D map of *A* was obtained by linearly fitting all the pixels at the same position on the images acquired at each compression step.

Fig 5.3 summarizes the procedure followed to retrieve the nonlinear shear coefficient from the initial position when no stress has been applied ($\sigma = 0$).

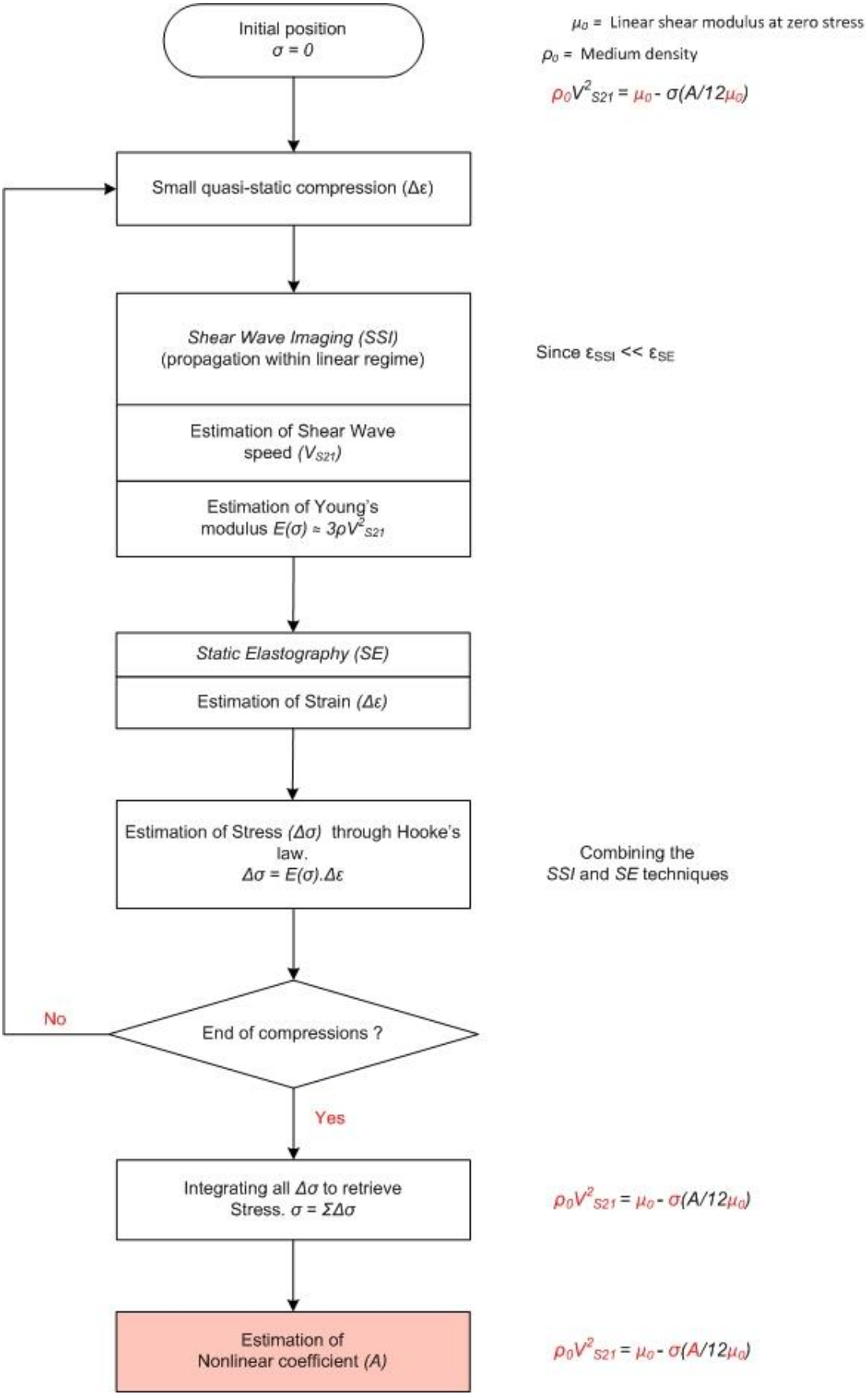

Fig 5.3. Calculation of the third order nonlinear shear coefficient by combining the SSI and SE techniques.

5.2.4 Finite element simulation

Simulations with a finite element model (FEM) of the sample were performed using the ANSYS 11.0 software (ANSYS Inc) in order to compute the theoretical vertical (z-axis) strain and stress fields at different compression steps. Half of the samples were meshed using 8 nodes hexahedral-shaped elements. The mesh density was controlled to generate an accurate mesh with a limited computing time (about 20 min) resulting in a FEM with 15.540 elements. The mesh was refined to 2 mm around the inclusions with an element size of 0.5 x 0.5 x 0.5 mm^3. The materials were considered as linear elastic isotropic. The assumed Young's moduli corresponded to the values measured at zero stress. The Poisson's ratio was set to 0.499 (quasi-incompressible soft media). The boundary conditions were chosen to mimic the experimental conditions. The boundaries between the inclusions and the surrounding material were frictionless. The displacements of the lower face of the samples were constrained along the vertical axis (*y*-axis). Constraining the nodes on the lower boundary from moving in the y-direction, while allowing them to move freely in the x-direction simulated perfect slip boundary conditions. The radial of the sample expansion in the (*xz*) plane was allowed. The displacement was blocked along the *x*-axis for the plane $x = 0$ (middle of the width) as well as the displacement along the *z*-axis for the plane $z = 0$ (middle of the depth). Thus, a quarter-symmetry in the *xz*-plane was assumed to reduce the simulation time. A vertical displacement of 1 mm (compression) was imposed to the nodes of the upper face and the resulting nodal vertical compression strains and stresses were computed.

5.3 Results

Three phantoms containing a soft inclusion and three containing a hard inclusion were built to perform the experiments. Those phantoms were numbered from 1 to 3 for each time of inclusion. Fig 5.4 contains the B-mode images and the shear velocity maps for a hard (#1) and a soft phantom (#2) obtained with the SSI technique before compression ($\sigma = 0$). Fig 5.5 presents the shear modulus maps for a hard phantom at the initial position and after 0.1 mm, 5% and 10% compression. The color scales depict the highest and lowest shear modulus values in red and blue respectively. On the maps, the hard inclusion can be clearly distinguished from its surrounding material due the high contrast in the shear modulus.

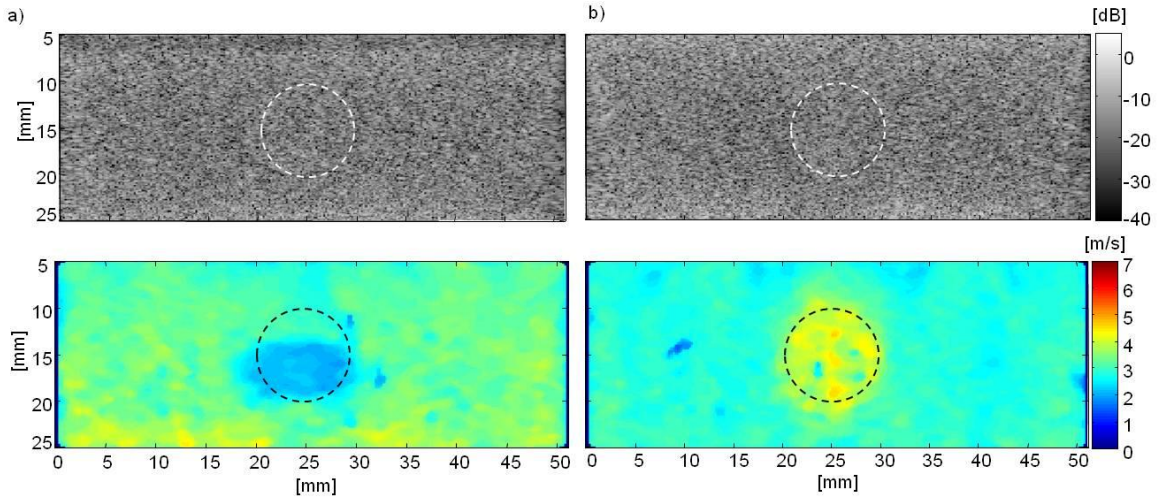

Fig 5.4. B-mode images (top) and shear velocity maps (bottom) at zero stress (σ = 0). a) soft phantom #2, b) hard phantom #1. The contrast in the shear velocity between the inclusions and the media is evident on the shear velocity maps.

Fig 5.6 contains the shear modulus values at each compression step for the hard phantom #1 presented in Fig 5.5 and for the soft phantom #1. These values were obtained by calculating the mean value within a window with an area of 2.5 x 5 mm^2 for the inclusions and 7 x 10 mm^2 for the media. The Fig 5.5 and Fig 5.6 show a decrease in the shear modulus within the hard inclusion and its surrounding medium due to the applied compression. The opposite occurred within the soft inclusion, whose shear modulus begun to sharply increase once the compression reached 1.5 mm (≈ 5%). Intuitively, one may have thought that the medium surrounding the soft inclusion would become stiffer with the compressions. Nonetheless, it seems that even a small difference in the shear modulus affects the medium response to the stress, as the medium elasticity increased with the compressions whereas the soft inclusion elasticity decreased. The shear moduli at zero stress for the soft inclusion and its surrounding medium were 4.2 kPa and 8.0 kPa, respectively.

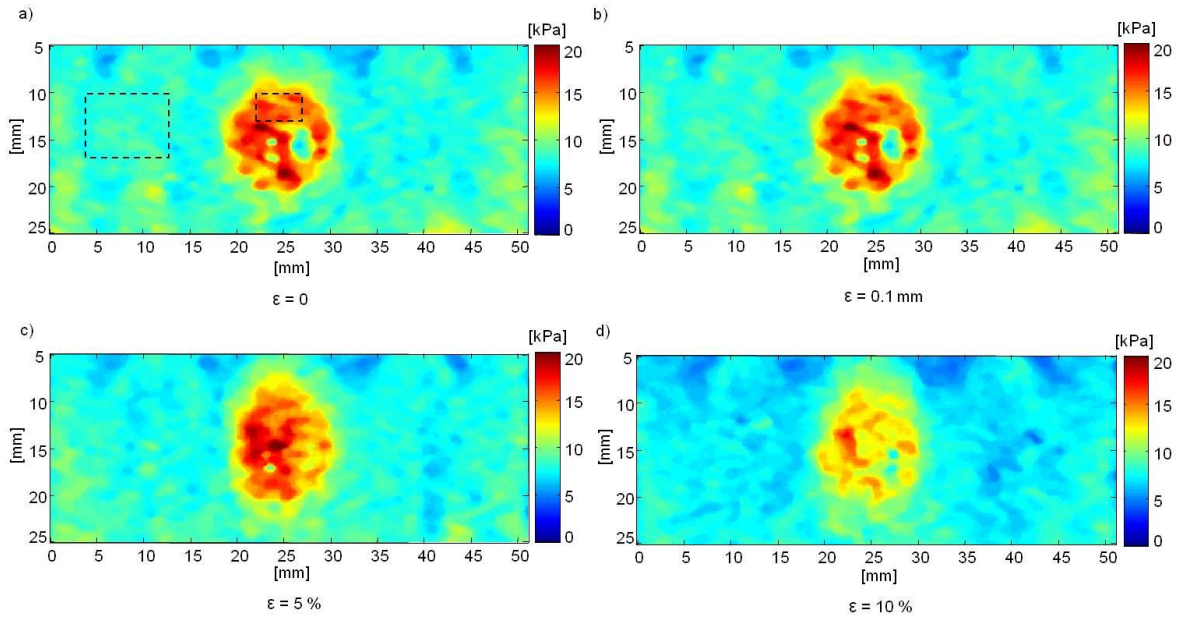

Fig 5.5. Shear Modulus maps at different compression steps for the hard phantom #1: a) ε = 0, b) ε = 0.01 mm, c) ε = 5% and d) ε = 10%. The compression causes a change in the shear modulus for the hard inclusion and the surrounding material.

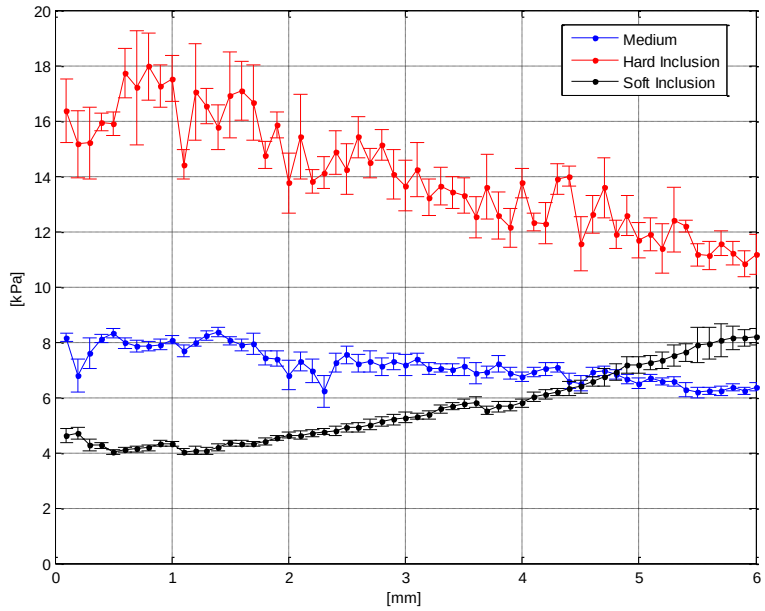

Fig 5.6. Shear Modulus values at different compression steps for the hard phantom #1 (inclusion), soft phantom #2 (inclusion) and hard phantom #1(medium). The mean values and standard deviations were calculated on a window of 10 mm^2. The shear modulus behaves differently for the hard and soft inclusion, as it decreases and increases respectively with the compression.

5.3.1 Experimental and simulated cumulative Strain maps

Fig 5.7 presents the experimental and simulated cumulative strain maps for both phantoms after 1 mm (3.3%) axial compression.

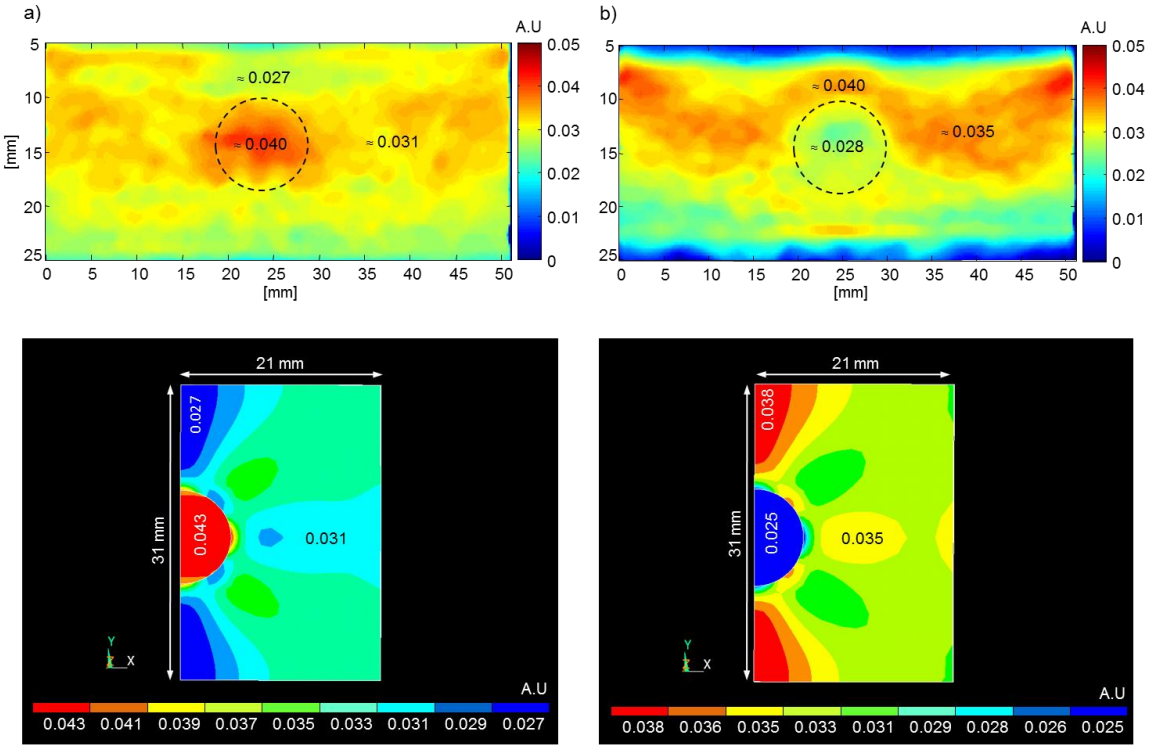

Fig 5.7. Experimental (top) and simulated (bottom) cumulative strain maps of both phantoms after 1 mm (3.3%) compression for the soft (a) and hard (b) inclusion. The color bars are dimensionless for both the experimental and the simulation results.

The experimental strain values, 2.8% for the hard inclusion and 3.5% for its surrounding material are in very good accordance with the simulation results with 2.5% for the inclusion and 3.5% for its surrounding material (Table 5.1). The experimental values were obtained by calculating the mean value and standard deviation within a window with an area of 10 mm^2 for the inclusions the media. The strain within the hard inclusion was higher than that one of its surrounding material, whereas the strain within the soft inclusion was lower than that one on its surrounding material. The strain distribution across the media surrounding the inclusions of both phantoms was quasi-uniform and similar in magnitude.

Table 5.1. Experimental and simulated cumulative strain maps for both phantoms after 1 mm axial compression.

	Cumulative Strain [%]					
	Soft phantom			*Hard phantom*		
	Incl.	*Med. top*	*Med. Side*	*Incl.*	*Med. top*	*Med. side*
Experimental values	4.00 ± 0.04	2.70 ± 0.01	3.10 ± 0.03	2.80 ± 0.02	4.00 ± 0.04	3.50 ± 0.02
Simulated Mean value of nodal stresses.	4.30	2.70	3.10	2.50	3.80	3.50

5.3.2 Experimental and simulated cumulative stress maps

Fig 5.8 contains the experimental and simulated cumulative stress maps for both phantoms after 1 mm (3.3%) uniaxial displacement. It can be seen that there is good

accordance between the experimental and simulated maps in terms of stress magnitude (Table 5.2) and distribution (Fig 5.8). The experimental stress values, with1.23 ± 0.02 kPa for the hard inclusion and 0.80 ± 0.01 kPa for its surrounding material are in very good accordance with the simulation results, with 1.21 kPa for the inclusion and 0.97 kPa for its surrounding material. The values contained in Table 5.2 were retrieved by calculating the mean value within a window with an area of 4 x 4 mm^2 for the inclusions and 4 x 8 mm^2 for the media. The hard inclusion showed a much higher stress level than its surrounding medium, whereas the soft inclusion presented much lower stress than its surrounding material. In both phantoms the stress was quasi-uniformly distributed across the area surrounding the inclusions. Moreover, in order to investigate the presence of any stress relaxation phenomena, stress measurements were also performed 1 min, 2 min and 3 min after each 0.1 mm (0.33%) compression step, with no significant difference observed between the different time point measurements.

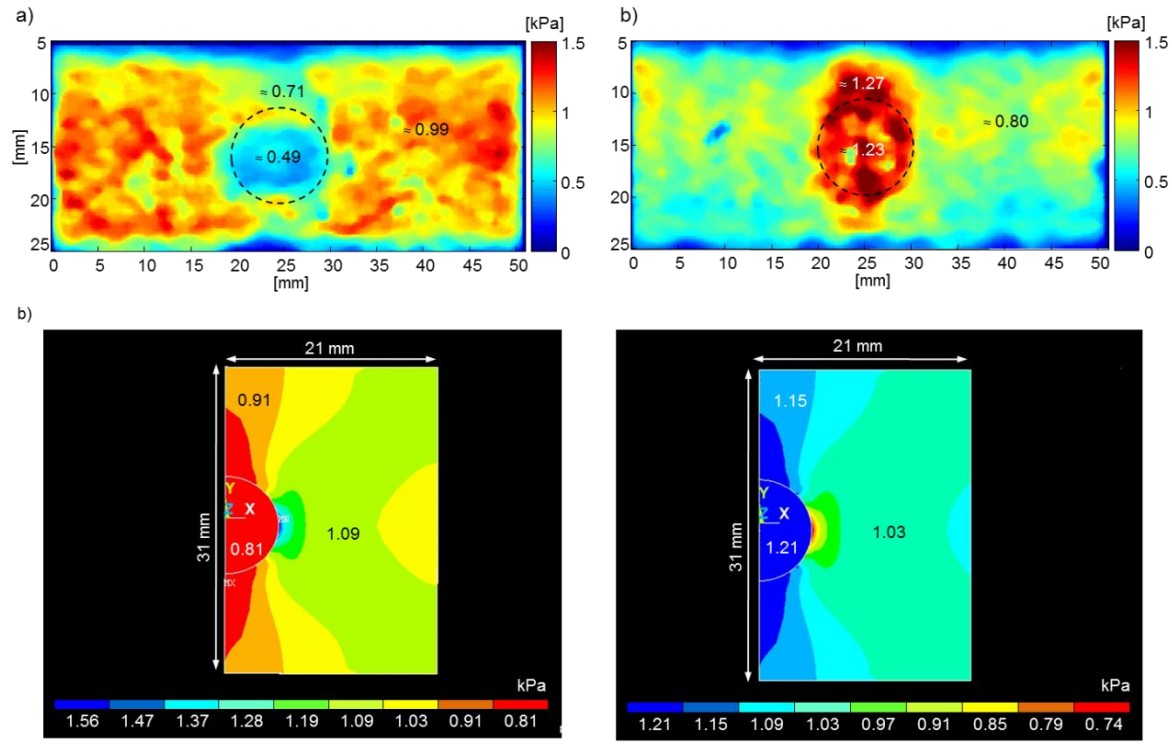

Fig 5.8. Experimental (top) and simulated (bottom) cumulative stress maps of both phantoms after 1 mm (3.3%)compression for the soft (a) and hard (b) inclusion. The color-bars are in kPa for experimental and the simulation results.

Table 5.2. Experimental and simulated values from cumulative stress maps for both phantoms after 1 mm (3.3%) axial compression.

	Cumulative Stress [kPa]					
	Soft phantom			*Hard phantom*		
	Incl.	*Med. top*	*Med. side*	*Incl.*	*Med. top*	*Med. side*
Experimental values	0.49 ± 0.01	0.71 ± 0.01	0.99 ± 0.01	1.23 ± 0.02	1.27 ± 0.03	0.80 ± 0.01
Mean value of nodal stresses.	0.81	0.91	1.09	1.21	1.15	0.97

5.3.3 Nonlinear shear modulus maps in agar-gelatin phantoms

The phantoms were compressed until the stress applied induced anisotropy [24] within the media and the inclusions, entering the nonlinear region. This allowed the quantification of the 2D nonlinear shear modulus maps after a cumulative displacement of 6 mm (19.8%) and 5 mm (16.5%) for the soft and hard inclusion respectively (Fig 5.9).

Table 5.3 contains the nonlinear shear modulus values in kPa for the inclusions and their surrounding media. These values were also retrieved by calculating the mean values within a window with an area of 4 x 4 mm^2 for the inclusions and 4 x 8 mm^2 for the media. As an example, the obtained nonlinear shear modulus for the inclusion for the soft phantom #2 and hard phantom #1 was -11.7 ± 2.4 kPa and 146.8 ± 11.7 kPa respectively.

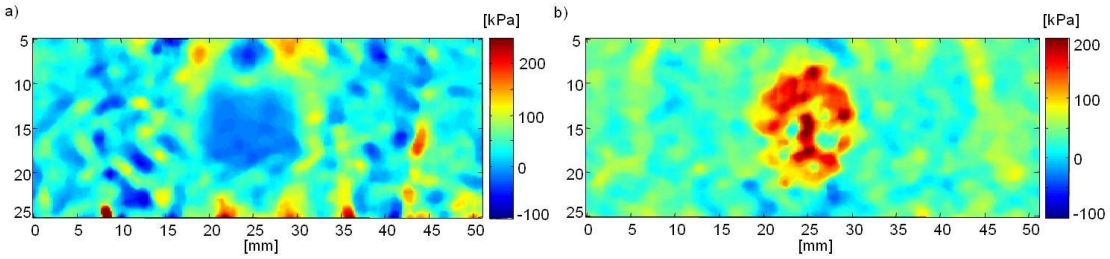

Fig 5.9. Nonlinear shear modulus maps after an absolute axial compression of: a) 6 mm for the soft phantom #2 and b) 5 mm for the hard phantom #1.

Table 5.3. Linear and nonlinear shear modulus values after 6 mm axial compression for all the soft and hard inclusion phantoms.

	Nonlinear Shear Modulus [kPa]		Linear Shear Modulus [kPa]	
	Inclusion	Medium	Inclusion	Medium
Soft Phantom # 1	-74.9 ± 5.6	34.8 ± 5.5	4.6 ± 0.2	17.5 ± 0.7
Soft Phantom # 2	-11.7 ± 2.4	29.4 ± 8.5	5.2 ± 0.2	17.8 ± 1.5
Soft Phantom # 3	-11.1 ± 1.5	161.9 ± 7.7	5.6 ± 0.2	26.4 ± 1.6
Hard Phantom # 1	146.8 ± 11.7	42.5 ± 4.9	16.3 ± 1.1	8.1 ± 0.2
Hard Phantom # 2	229.8 ± 7.3	61.2 ± 4.1	24.1 ± 0.9	12.5 ± 0.3
Hard Phantom # 3	228.0 ± 12.1	80.9 ± 3.6	22.5 ± 0.7	11.8 ± 0.3

5.3.4 Nonlinear shear modulus maps in *ex vivo* beef liver samples

Three beef liver samples were compressed in steps of 0.1 mm until reaching 16% (≈ 3 mm) of axial compression in the same manner as the phantoms did. Fig 5.10 depicts the 2D linear and nonlinear shear modulus maps for sample #2.

Table 5.4 presents the linear and nonlinear shear modulus values for the three different samples, which were obtained by calculating the mean value over the entire map. The retrieved shear moduli were in good accordance with the work of B. Arnal *et al.* [37], in which the measured shear modulus of bovine liver had a value of 3.15 ± 0.27 kPa.

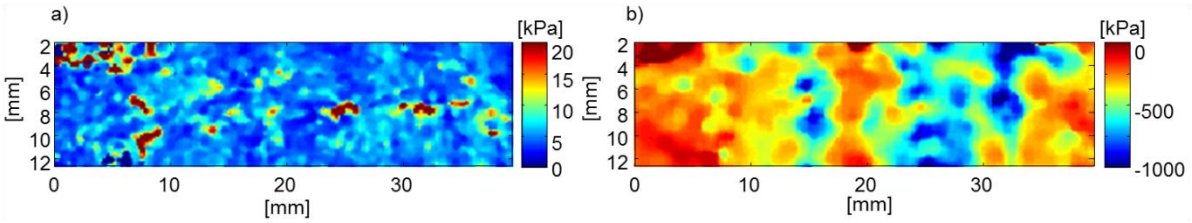

Fig 5.10. Linear shear modulus map at zero stress for a) the liver sample #2 and b) its corresponding nonlinear shear modulus map after 3 mm compression.

Table 5.4. Linear and nonlinear shear modulus after 16 % (≈ 3 mm) axial compression for the beef liver samples

	Nonlinear Shear Modulus [kPa]	Linear Shear Modulus [kPa]
Sample #1	-128.4 ± 6.1	3.2 ± 1.1
Sample #2	-302.8 ± 58.3	4.9 ± 2.8
Sample #3	-576.6 ± 97.5	8.0 ± 3.5

5.4 *Ex vivo* application

5.4.1 *Ex vivo* strain and stress calculation in mouse colon tissues

Mechano-transduction refers to the mechanisms or processes by which cells transform given mechanical stimuli into chemical activity. Increasing evidence shows the involvement of mechano-transduction processes in the regulation of the interplay between shape-related strains and state of expression of the genome in living tissues. However, tools allowing long term control of physiological mechanical strains from the inside of the tissues are lacking to investigate the impact of such processes in organisms *in vivo*. Experiments *ex vivo* have demonstrated that the pressure potentially associated with intestinal transit or tumour growth, triggers the development of tumours in pre-tumoral transgenic mice colon tissues [38].

This work is performed within the frame of a multi-disciplinary research project in cooperation with E. Farge and his research team (INSERM-CNRS-Institut Curie). This ongoing project aims to investigate the involvement of the local stresses (caused by tumour growth on pre-tumoural tissues) in the development of such mechano-transduction processes leading to oncogene expression. Otherwise stated, the project aims to investigate the influence of the stresses generated by tumour growth on the triggering of mechano-transduction processes, which may potentially lead to cancer development on the surrounding cancer-prone tissues. The goal was to develop experiments allowing the endocytic accumulation of magnetic liposomes in the colon of mice by natural means, and the magnetic induction of the mechanical strains *in vivo* for up to three months. Tumour growth pressure was mimicked by the manipulation of the ferromagnetic fluid locally concentrated in the cells. The task

assigned to our group consisted in using US imaging to investigate the *ex vivo* tissue response to short-time (a few minutes) perturbations by varying the distance between mouse colon samples embedded in agar-gelatin phantoms and a magnet.

5.4.1.1 US Imaging

For these experiments, an US probe (256 elements, 15 MHz central frequency, Vermon, France) was used. The probe was driven by the same programmable ultrafast imaging device employed in previous experiments reported in this manuscript.

A first US experiment aimed to evaluate the feasibility of measuring the deformation induced within an agar-gelatin phantom (2% by weight of agar and 4% by weight of gelatin) by the interaction between a 0.5 cm diameter magnet and tiny (0.2 cm diameter) plastic tubes (located inside the phantom) containing ferromagnetic fluid. The magnet and the probe were placed over the phantom's surface as shown in Fig 5.11.

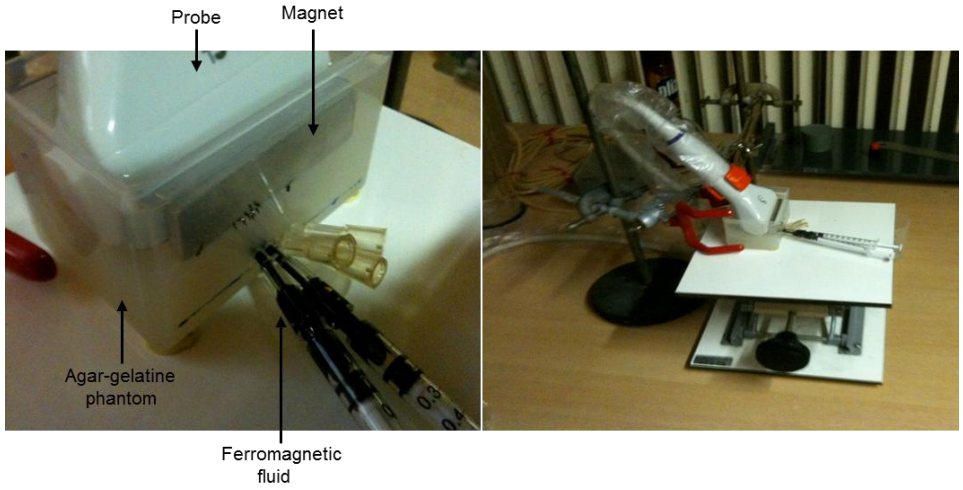

Fig 5.11. Measurement setup for the initial trial. Ferromagnetic liquid was injected into the small plastic tubes (Ø = 2 mm) that traversed the agar-gelatin phantom. The magnet (1 T/m^{-1}) was then placed over the phantom's surface. The idea was to observe if the ferromagnetic fluid-magnet interaction generated displacement within the phantom that could be detected with ultrasound.

A B-mode image was acquired before injecting the ferromagnetic fluid into the plastic tubes crossing the phantom to be used as the reference image (Fig 5.12(a)). B-mode images were acquired after each of the tubes was filled with the fluid. The cumulative displacement within the phantom (blue area) after injecting 0.2 ml of ferromagnetic fluid was approximately 35 µm (Fig 5.12(b)). As the magnet was positioned on top of the phantom, the displacement was mainly generated along the depth of the image and had its maximum values on the pixels closest to the tubes.

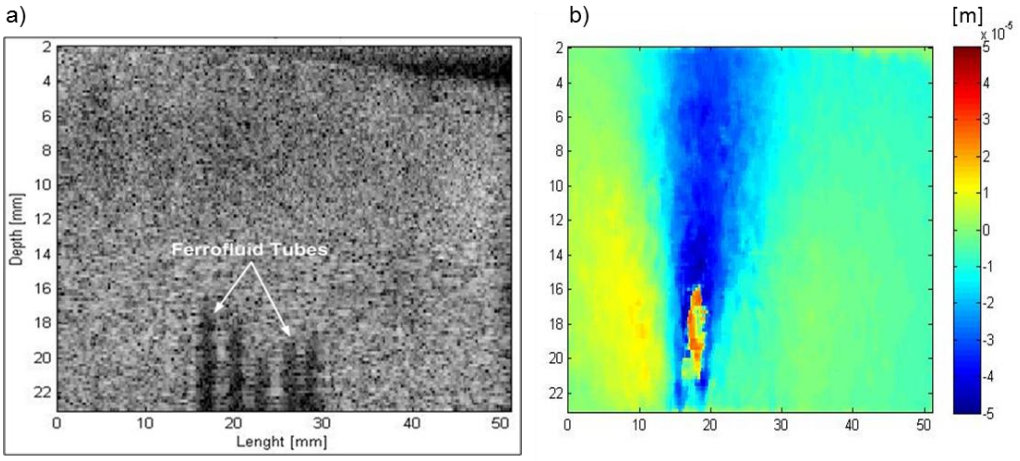

Fig 5.12. a) B-mode images of the plastic tubes containing the ferromagnetic fluid. The image shows the attenuation caused by the tubes; b) Displacement map. The displacement induced by the ferromagnetic interaction within the phantom (blue zone) was of approximately 35 µm. The noisy area on the displacement map is the result of the attenuation caused by the tubes.

Fig 5.13 presents the characterization of 3 mm diameter magnet used in these experiments. The magnetic field strength is given in kiloGauss (kG) as a function of the distance from the magnet. One can appreciate that the magnetic field strength increases exponentially as one moves closer to the magnet.

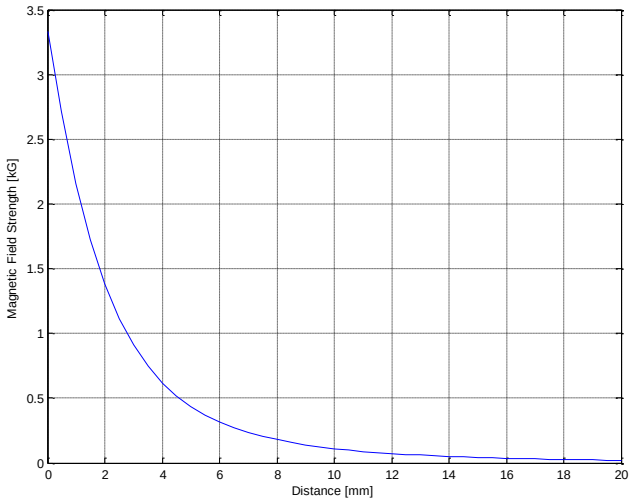

Fig 5.13. The curve depicts the magnetic field strength in kG as a function of the distance for the 3 mm diameter magnet employed in the experiements. The magnetic field strength increases exponentially as one moves closer to the magnet.

Since the experimental results showed the feasibility of measuring micro-metric displacements caused by the magnetic interaction, the following step consisted in measuring *ex vivo* the displacement within the magnetized colon of mice to subsequently retrieve the strain and stress by using the procedure explained before in this chapter.

5.4.1.2 Animal preparation

Wild-type (healthy) and transgenic (genetically modified) mice were used for the experiments. To mimic pressure from inside the tissue, the cells were magnetized *in vivo* following an intra-venal injection of ferromagnetic fluid encapsulated into PEG-Coated liposomes. While the animals were under the effect of the anaesthesia, the colon was targeted by fixing a 3 mm diameter magnet (1 T/m^{-1}) under the skin, 5 mm away from the colon (Fig 5.14(a)). The magneto-liposomes were then injected into the colon. The magnet induced forces (red and blue arrows) on the colon that mimic the pressure forces generated as the tumour grows larger (Fig 5.14(b)). The mice which received the ferromagnetic fluid injection and which carried the magnet are referred as "Injected+Magnet". The mice which received the ferromagnetic fluid injection but which did not carry the magnet are referred as "Injected". Finally, the mice which did not receive the ferromagnetic fluid injection or carry the magnet are referred as "Control". The mice which carried the magnet, did it for a period ranging between 1 week to 3 months.

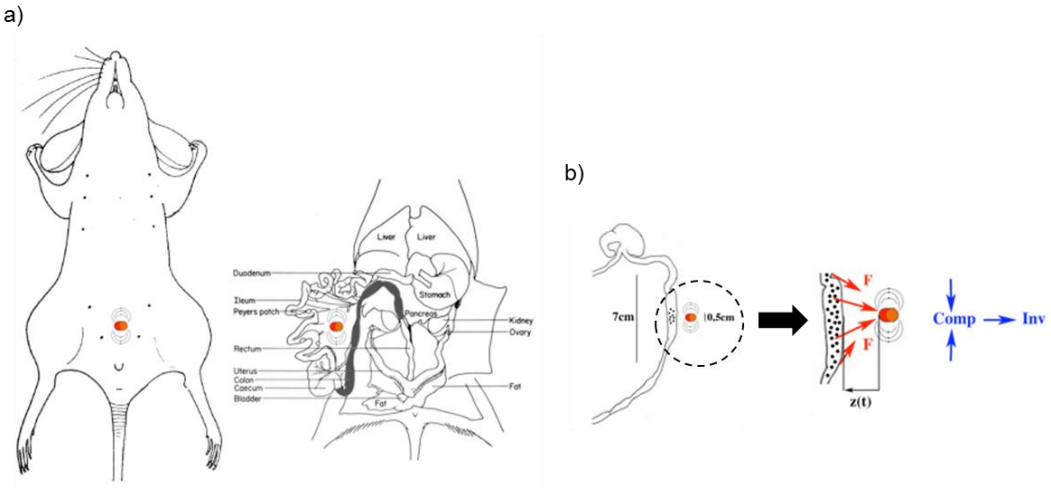

Fig 5.14. Targeting the colon by positioning the magnet. a) In order to concentrate the ferromagnetic liposomes into the colon tissue, a 0.3 cm magnet is ventrally applied onto the colon (in black in the "in situ" view) of an anesthetized mouse before intra-venally injecting the sample; b) The magnet induces forces (red and blue arrows) on the colon that mimic the pressure forces generated by the tumour growth.

It is strongly believed that endocytosis at the cellular level protect the ferromagnetic particles from the immune system and liver digestion for about two to three months, which is the time required by a mouse colon tumour to develop [39]. Additionally, it has been proven that implantation of cells having internalised magnetic liposomes through endocytosis *ex vivo*, show stable accumulation of magnetic fluid in the living cells on the time scale with no wash out on the 3 months *in vivo* [40].

The magnetized colons of several Wild-type and transgenic mice were extracted after sacrificing the animals in order to perform *ex vivo* measurements. Each colon sample was placed in an agar-gelatin phantom (2% by weight of agar and 4% by weight of gelatin). A small magnet (5 mm in diameter) was axially approached towards the colon in steps of 0.5

mm until completing 3 mm of absolute axial displacement. Fig 5.15 depicts the experimental setup.

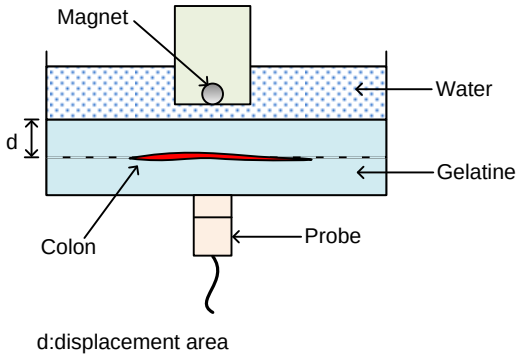

Fig 5.15. Measurement setup for the ex vivo measurement of the displacement induced by the interaction between the magnet and the colon. The magnet was approached axially towards the colon in steps of 0.5 mm.

Fig 5.16 displays a representative B-Mode image and the corresponding displacement map for a transgenic colon sample 2 months after the ferromagnetic injection, after an absolute axial displacement of 3 mm. The area were the colon was placed (dark blue area) presented the highest amount of displacement with approximately 35 µm, whereas the mean displacement for the rest of the phantom was approximately 18µm. These values were in very good accordance with the ones obtained in the experiment performed with the plastic tubes filled with the ferromagnetic fluid.

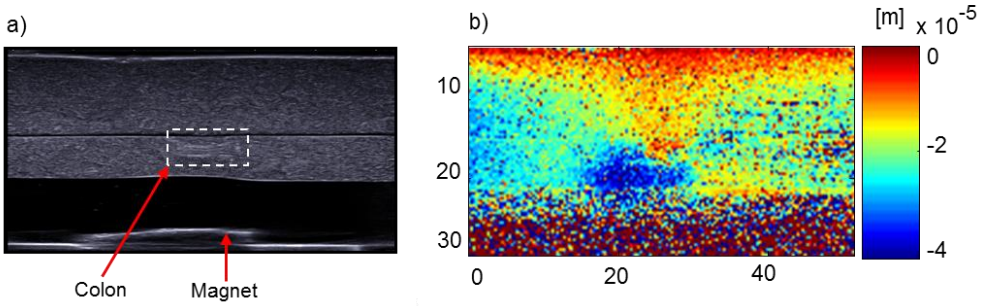

Fig 5.16. A mouse colon sample 2 months after the ferromagnetic injection; a) The B-mode image shows the sample and the magnet; b) Displacement map after 3 mm of absolute axial displacement. The mean value of displacement within the colon (dark blue area) and the rest of the phantom was of 35 µm and 18 µm respectively. The displacement maps have a resolution of about 0.2 mm.

Having proved the feasibility of accurately measuring micro-metric displacements, ex vivo measurements were performed on Wild-type and transgenic mouse colon samples to retrieve the cumulative strain (deformation) and stress within the samples after a given amount of axial compression. Fig 5.17 contains the strain maps for different transgenic colon samples after an absolute axial compression of 3 mm. Fig 5.17(a) Control (no injection/no magnet), Fig 5.17(b) Injected (injection/no magnet) and, Fig 5.17(c) Injected + Magnet (injection + magnet). The experiments were performed 2 months after the ferromagnetic fluid

injection (in the case of the "Injected" and the "Injected + Magnet" samples). The colon is encircled by the dotted-line window on each map. The corresponding sample elasticity and stress values are displayed below each strain map. The strain is denoted by the colour-bar in percentage (%). One observes that the "Control" and the "Injected + Magnet" colon samples, presented the minimum and maximum stress levels with 166.4 ± 405.9 Pa and 1.02 ± 0.15 kPa, respectively.

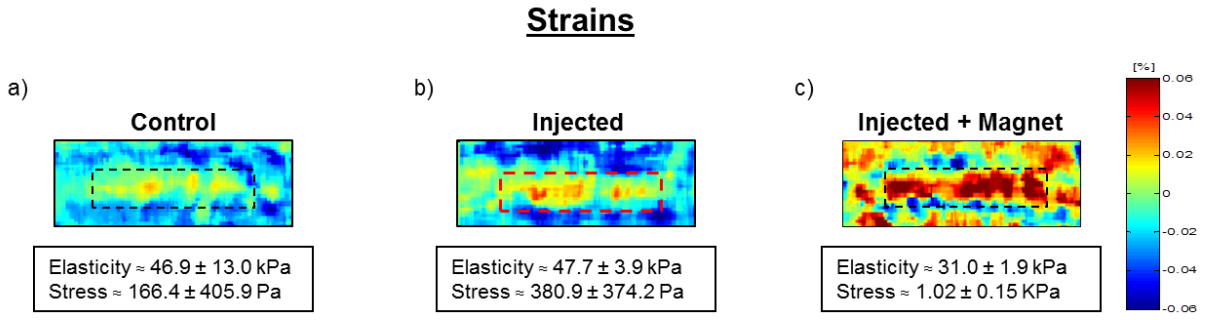

Fig 5.17. Strain maps for different kinds of transgenic colon samples, 2 months : (a) Control (no injection/no magnet), (b) Injected (injection/no magnet) and, (c) Injected + Magnet (injection + magnet). The experiments were performed 2 months after the ferromagnetic fluid injection (in the case of the "Injected" and the "Injected + Magnet" samples). The colon is encircled by the dotted-line window on each map. The corresponding sample elasticity and stress values are displayed below each strain map. The strain is denoted by the colour-bar in percentage (%). One observes that the "Control" and the "Injected + Magnet" colon samples, presented the minimum and maximum stress levels with 166.4 ± 405.9 Pa and 1.02 ± 0.15 kPa, respectively.

5.5 Discussion

The combination of conventional US and quantitative elasticity images obtained with the SSI technique provides a very useful tool for the characterization of tissue mechanical properties as shown in Fig 5.4. Here, the high contrast in elasticity between the inclusions and their surrounding material could be clearly determined and the shear modulus retrieved. When a medium is submitted to an external (manual palpation) or internal stress (such as blood pressure), the quantification of the shear modulus gives access to the estimation of local stress values through Hooke's law while strain imaging is performed, an important feature of the SSI technique which was here demonstrated to lead to quantitative nonlinear elasticity (Landau coefficient) imaging. In the future, this method could probably be implemented on standard imaging probes driven by ultrafast US scanners, which would make it easily transferrable to clinics. Moreover, the presented setup does not require the use of force sensors in order to estimate the stress field applied on the surface of the organ by the front face of the probe.

The fact that the magnitude of the compression between two consecutive steps was small enough (≈ 0.33%) to keep the material within its linear regime, allowed the retrieval of the Young's modulus and the use of Hooke's law to quantify the stress ($\Delta\sigma$) between two consecutive steps. The experimental shear modulus values for the hard inclusions were positive and drastically decreased with increasing axial compression (from 16.3 ± 1.1 kPa at

zero stress to 11.1 ± 0.7 kPa at 6 mm compression) as seen in the experiment described in Fig 5.6. For the medium, the shear modulus slightly decreased (from 8.1 ± 0.1 kPa at zero stress to 6.3 ± 0.1 kPa after 6 mm compression) with the same increasing compression. On the contrary, the shear modulus within the soft inclusion steadily increased (from 4.8 ± 0.2 kPa at zero stress to 8.0 ± 0.2 kPa) when the compression reached 6 mm (≈ 19%). For the *ex vivo* liver samples, the retrieved shear moduli are retrieved with a good accordance with the literature [37].

One can clearly verify in the phantom experimental results that the shear modulus of a tissue mimicking material is inversely proportional to the strain under an external force or stress. This means that the higher their elastic constant, the less they deform. This could be clearly observed in the strain maps (Fig 5.7), with the soft inclusion presenting the highest strain values, whereas the hard inclusion the lowest ones under the approximately same amount of axial stress. There was a slight difference in the strain values between the surrounding materials of both inclusions, which could be due to the fact that the stress was not uniformly applied. However, such a small difference could be neglected as it did not influence the stress or the nonlinearity calculations.

As opposed to the strain, the stress and the nonlinear shear modulus were found to be directly proportional to the material's shear modulus at zero stress. Therefore, the higher the shear modulus of a material, the higher the stress and its nonlinear shear modulus (see Fig 5.8). The hard inclusion showed a very high stress level whereas the soft one a very low one. The stress for the media surrounding both phantoms presented also very similar values due to having the same agar-gelatin concentration (2% A - 5% G). The stress for the medium surrounding the soft and hard inclusion after 1 mm compression was 0.99 ± 0.01 kPa and 0.8 ± 0.01 kPa, respectively (see Table 5.2).

The results of the experiments performed on phantoms had good accordance with the simulations as seen in Fig 5.7 and Fig 5.8. The difference between the strain and stress levels around the inclusions was very small and may have been caused by two factors. Firstly, to simplify the calculations, only the axial component of the strain tensor was taken into account, ignoring the lateral and elevational components. Secondly, the experimental results were influenced by the nonlinear effects due to the applied compression. The simulation software assumes the medium to be perfectly isotropic and without any kind of nonlinearity.

The estimation of the nonlinear shear modulus in agar-gelatin phantoms was found to be reproducible and its standard deviation remained below 13% (Table 5.3).The resolution of the nonlinear shear modulus maps (≈1 mm) was comparable to that one of the shear modulus maps. Both hard and soft inclusions were easily identified as seen in Fig 5.9. The nonlinear parameter was found to be negative for the soft inclusions (respectively -74.9 ± 5.6 kPa, -11.7

± 2.4 kPa and -11.1 ± 1.5 kPa for the different soft phantoms) and positive for the hard phantoms (respectively 146.8 ± 11.7 kPa, 229.8 ± 7.3 kPa and 228.0 ± 12.1 kPa for the different hard phantoms).

The retrieval of the nonlinear shear modulus in *ex vivo* beef liver samples was also reproducible. The nonlinear shear modulus values were negative for all the samples, with a mean value of -335.9 ± 53.9 kPa (Table 5.4). Interestingly and opposite to what happened in agar-gelatin or PVA phantoms [24], the nonlinear shear modulus seems to decrease with an increasing shear modulus. This can be due to the internal structure of the soft tissues, which is very different in phantoms. Nevertheless, to our knowledge, these are the first reports of *ex vivo* nonlinear shear modulus quantification in liver samples.

A point of particular interest lies in the fact that the nonlinear shear modulus is a very sensitive parameter which rapidly affected the shear wave speed in our experiments. One can take benefit of this sensibility. Indeed, contrary to a conventional approach where one would try to estimate the stress/strain curve at high strain values (>10%) in order to retrieve the nonlinear parameter, Hooke's law was only used here to retrieve the stress field between two consecutive compression steps ($\Delta\sigma$) and not to retrieve nonlinearity (Fig 5.3). This value of stress was subsequently used to calculate the nonlinear parameter by applying the mathematical development presented in Eq. 5, taking into account the displacement induced within the medium by the shear wave propagation and the quasi static compressions ($\varepsilon_{SSI} << \varepsilon_{Static}$). Thus, to retrieve the nonlinear shear modulus parameters it is not necessary to enter the nonlinear region of the stress-strain curve. One can retrieve the nonlinear shear modulus by taking benefit of the acoustoelasticity theory combined with shear wave propagation. The calculation of this nonlinear parameter can be performed at much smaller strains. It only requires the use of enough points for the linear fitting of Eq. 5 in order to avoid an erroneous or an inaccurate value for each pixel of the 2D nonlinear shear modulus map. In the experiments presented in this chapter on phantoms, 20 small compression steps of 0.33% were sufficient to reach accurate estimates of the nonlinear shear modulus.

The use of this concept for *in vivo* medical applications will require acquiring quantitative shear modulus maps fast enough during a quasi-static compression of the investigated organ. The Supersonic Shear Imaging technique can retrieve a quantitative shear modulus map deep into tissues in less than some milliseconds and consequently it would not represent a limiting factor for clinical experiences. The estimation of successive strain and stress maps during the quasi-static compression would only require the real time implementation of interleaved sequences of SSI imaging and strain imaging, which is not a technical issue on the programmable US scanners (*Aixplorer, Supersonic Imagine*, Aix en Provence, France) used in our experiments.

Even though the *ex vivo* experiments on cancerous mice tissues samples produced encouraging results, these are only preliminary results of this on-going project. The technique employed was able to measure micro-metrical displacements and therefore, retrieve the stress applied to the tissue. Nevertheless, it needs to be improved in order to be able to perform *in vivo* measurements. Imaging *in vivo* organs such as the colon is an arduous task due to being very small (approximately 1 mm in diameter) and difficult to distinguish within the body. Currently, *ex vivo* experiments are being performed on wild-type and transgenic mice. The results show that the transgenic mice are more prone to develop cancer tumours, as a result of the stress induced by the magnetic interaction between the ferromagnetic liquid injected into the colon and the subcutaneously-placed magnet.

The presented set-up is a part of a bigger project, which aims show the influence of applied stresses on cells in cancer development. Future works would include finding a way to implement this technique *in vivo* in pre-clinical and clinical studies.

5.6 Conclusion

The combination of Supersonic Shear Imaging and static elastography allowed to provide quantitative mapping of the nonlinear elasticity parameter in soft tissues. Such quantitative mapping is possible thanks to the acoustoelasticity theory. By estimating the variations of the shear wave propagation speed during a static compression of the medium, it is possible to retrieve the nonlinear elastic parameter at strain values much smaller than the ones required for the direct estimation of the material nonlinear stress/strain relationship. When compared to numerical finite element simulations, the experimental strain and stress maps in gelatin phantoms showed great accordance. The results demonstrated that nonlinear elasticity can be estimated with good reproducibility (standard deviation < 11%) and that nonlinear elastic shear modulus maps exhibit a millimetric resolution. For the first time, the nonlinear shear modulus of *ex vivo* liver samples was reported. As expected, for an important amount of applied stress, the elasticity of biological tissues was found to be strongly nonlinear. Although we have demonstrated the feasibility to quantify stress and shear nonlinearity in soft phantoms and *ex vivo* liver samples, it would be necessary to perform *in vivo* studies to validate these results before clinical investigations can take place. The capability of the technique to retrieve *ex vivo* very small deformations (*e.g.* 0.03%) in colon tissue samples was demonstrated, and open the path for future *ex vivo* and *in vivo* applications. Nevertheless, *in vivo* measurements would demand improvements on the technique, which once accomplished, would be applicable to any other biomedical approaches requiring an internal control of the tissue pressure *in vivo*. For instance, numerous diseases

such as osteoporosis and potentially immune system disorders are associated with issues in mechano-transduction processes [41].

References

[1] R. M. Lerner, K. J. Parker, J. Holen, R. Gramiak, R.C. Waag, "Sono-elasticity: Medical elasticity images derived from ultrasound signals is mechanically vibrated targets", Acoustical Imaging, L. J. Kessler, Ed. New York: Kluwer Academic, vol. 16, pp. 317-327, 1998.
[2] A. R. Skovoroda, A. P. Sarvazyan, "The reconstruction of shear viscoelastic properties using response of medium to focused ultrasonic loading", Biofizika, vol. 44, pp. 325-329, 1999.
[3] S. F.Levinson, M. Shinagawa, T. Sato, "Sonoelastic determination of human skeletal muscle elasticity", J. Biomech., vol. 28, no. 10, pp. 1145-1154, 1995.
[4] M. Fatemi, J. F. Greenleaf, "Ultrasound-Stimulated vibro-acoustic spectrography", Science, vol. 280, pp. 82-85 1998.
[5] K. R. Nightingale, M. S. Soo, R. W. Nightingale, G. E. Trahey, "Acoustic radiation force impulse imaging: In vivo demonstration of clinical feasibility", Ultrasound in Medicine and Biology., 28 (2), pp. 227-235, 2002.
[6] J. Bercoff, M. Tanter, M. Fink, "Supersonic Shear Imaging: A new technique for soft tissue elasticity mapping", IEEE Trans. Ultra., Ferro. Freq. Ctrl., 51(4), pp. 396-409, 2004.
[7] L. Sandrin, B. Fourquet, J.M. Hasquenoph, S. Yon., C. Fournier, F. Mal, C. Christidis, M. Ziol, B. Poulet, F. Kazemi, M. Beaugrand, R. Palau, "Transient elastography: a new non-invasive method for assessment of hepatic fibrosis", Ultr. Med. & Bio. 29, pp. 1705–1713, 2003.
[8] S. Catheline, J.-L. Gennisson, G. Delon, R. Sinkus, M. Fink, S. Abouelkaram, and J. Culioli, "Measurement of viscoelastic properties of homogeneous soft solid using transient elastography: An inverse problem approach", J. Acoust. Soc. Am., 116, pp. 3734–3741, 2004.
[9] J.L. Gennisson, T. Deffieux, E. Macé, G. Montaldo, M. Fink, M. Tanter, "Viscoelastic and anisotropic mechanical properties of in vivo muscle tissue assessed by Supersonic Shear Imaging.", Ultr. Med. & Bio., 36 (5), pp. 789-801, 2010.
[10] S. Catheline, J.-L. Gennisson, and M. Fink, "Measurement of elastic nonlinearity of soft solids with transient elastography," J. Acoust. Soc. Am.,114, pp. 3087–3091, 2003.
[11] M. Shinohara, K. Sabra, J.-L. Gennisson, M. Fink, M. Tanter, "Real-time visualization of muscle stiffness distribution with ultrasound shear wave imaging during muscle contraction" .MUSCLE & NERVE, Vol. 42, Issue: 3, pp. 438-441, 2010.
[12] M. Couade, M. Pernot, E. Messas, A. Bel, M. Ba, A. Hagege, M. Fink, M. Tanter, "In vivo Quantitative Mapping of Miocardial Stiffening and Transmural Anisotropy During the Cardiac Cycle", IEEE Trans. On Medical Imaging.,Vol. 30, Issue 2, pp. 295–305, 2011.
[13] M. Couade, M. Pernot, C. Prada, E. Messas, J. Emmerich, P. Bruneval, A. Criton, M. Fink, Tanter M., "Quantitative assessment of arterial wall biomechanical properties using shear wave imaging", Ultr. Med. & Bio. 29, Vol. 36, Issue 10, pp. 1662–1676, 2010.
[14] M. Muller, J.-L. Gennisson, T. Deffieux, M. Tanter, M. Fink, "Quantitative viscoleasticity mapping of human liver using Supersonic Shear Wave Imaging: Preliminary in vivo feasibility study", Ultr. Med. & Bio., Vol. 35, N 2, pp. 219-229, 2009.
[15] T. A Krouskop, T. M Wheeler, F. Kallel, B. S Garra, T. Hall, "Elastic moduli of breast and prostate tissues under Compression", *Ultrason. Imaging* (20), pp. 260-274, 1998.
[16] P. Wellman, R. H. Howe, E. Dalton, K. A. Kern, "Breast tissue stiffness in compression is correlated to histological diagnosis. *Technical Report", Harvard BioRobotics Laboratory, Division of Engineering and Applied Sciences,Harvard University*, 1999.
[17] T. J. Hall, Z. Yanning, C. S. Spalding, "In vivo real-time freehand palpation imaging" *Ultrasound Med. Biol.* 29, pp. 427– 435, 2002.
[18] R.Q. Erkamp, S. Y. Emelianov, A. R. Skovoroda, M. O'Donnell, "Nonlinear Elasticity Imaging: Theory and Phantom Study", *IEEE Trans. Ultra., Ferro. Freq. Ctrl.,* Vol. 51, N. 5, pp. 532-539, 2004.
[19] R.Q. Erkamp, A. R. Skovoroda, S. Y. Emelianov, M. O'Donnell, "Measuring the Nonlinear Elastic Properties of Tissue-Like Phantoms", *IEEE Trans. Ultra., Ferro. Freq. Ctrl.,* Vol. 51, N. 4, pp. 410-419, 2004.
[20] A. A. Oberai, N. H. Gokhale, S. Goenezen, P. E. Barbone, T. J. Hall, A. M. Sommer, and J. Jiang, "Linear and nonlinear elasticity imaging of soft tissue *in vivo*: demonstration of feasibility" , *Phys. Med. Biol.,* 54, pp. 1191–1207, 2009.
[21] N. H. Gokhale, P. E. Barbone, A. A. Oberai, "Solution of the nonlinear elasticity imaging inverse problem: the compressible case, Inverse Problems", 24 045010, 2008.
[22] X. Jacob, J.-L. Gennisson, S. Catheline, M. Tanter, C. Barriere, D. Royer, M. Fink, "Study of elastic nonlinearity of soft solids with transient elastography", Proc.-IEEE Ultrason. Symp. 1, pp. 660 – 663, 2003.
[23] S. Catheline, J.-L. Gennisson, Tanter M., M. Fink, "Observation of shock transverse waves in elastic media," *Phys. Rev. Lett.* 91 , pp. 43011 – 43014, 2003.
[24] J.-L. Gennisson, M. Rénier, S. Catheline, C. Barière, J. Bercoff, M. Tanter, M. Fink, "Acoustoelasticity in soft solids: Assessment of the nonlinear shear modulus with the acoustic radiation force", *J. Acoust. Soc. Am.,* 122 (6), pp. 3211- 3219, 2007.
[25] S.D. Hugues, J.L. Kelly, "Second-order elastic deformation of solids", *Phys. Rev.* 92, 1145 – 1149 (1953).
[26] M. F. Hamilton, Y.A. Ilinskii, A. Zabolotskaya, "Separation of compressibility and shear deformation in the elastic energy density (L)", *J. Acoust. Soc. Am.,* 116, pp. 41-44, 2004.
[27] A. Zabolotskaya, M. F. Hamilton, Y.A. Ilinskii, G.D. Meegan, "Modeling of non-linear shear waves in soft solids", *J. Acoust. Soc. Am.,* 116, pp. 2807-2813, 2004.
[28] J. Ophir, I. Cespedes, H. Ponnekanti, Y. Yazdi, X. Li, "Elastography: a quantitative method for imaging the elasticity of biological tissues", Ultrasonic *Imaging*, 13, pp. 111-134, 1991.
[29] H. Ponnekanti, J. Ophir, I. Cespedes, "Ultrasonic imaging of the stress distribution in elastic media due to an external compressor", *Ultr. Med. & Bio*., 20, pp. 27-33, 1994.

[30] B. Garra, I. Cespedes, J. Ophir, R. Spratt, R. Zuurbier, C. Magnant, M. Pennanen, "Elastography of breast legion: Initial clinical results ", *Radiology*, Vol. 202, pp. 79-86, 1997.
[31] E.E. Konofagou, P. Dutta, J. Ophir, and I. Cespedes, "Reduction of Stress Nonuniformities by Apodization of Compressor Displacement in Elastography", *Ultrasound in Medicine and Biology* 22(9), pp. 1229-1236, 1996.
[32] T. Z. Pavan, E. L. Madsen, G. R. Frank, A. A. O Caneiro, T. J. Hall, "Nonlinear elastic behavior of phantom materials for eastography", *Phys. Med. Biol.*, 55 (9), 2679, 2010.
[33] A. Itoh, E. Ueano, E. Tohno, H. Kamma, H. Takahashi, T. Shiina, M. Yamakawa, T. Matsumura, "Breast disease: clinical application of US. Elastography for diagnosis", *Radiology* pp. 239:341-350, 2006.
[34] W. Khaled, S. Reichling, O. T Bruhns., H. Ermert, "Ultrasonic strain imaging and reconstructive elastography for biological tissue", Ultrasonics, Vol. 44 Supplement 1, pp. e199-e202, 2006.
[35] L.D. Landau, M. Lifshitz, Theory of Elasticity, 3rd ed., (Butterworth-Heinemann, Oxford, 2002).
[36] J.-L. Gennisson, G. Cloutier, "Sol-gel transition in agar-gelatin mixtures studied with transient elastography", *IEEE Trans. Ultra., Ferro. Freq. Ctrl.*, 53, pp. 716–723, 2006.
[37] B. Arnal, M. Pernot , M. Tanter, "Monitoring of Thermal Therapy Based on Shear Modulus Changes : I. Shear Wave Thermometry", IEEE Trans. Ultra., Ferro. Freq. Ctrl., 58 (2), pp. 369-378, 2011.
[38] J. Whitehead *et al*, Mechanical factors activate beta-catenin-dependent oncogene expression in APC mouse colon, "*HFSP" J* 2, pp. 286-294, 2008.
[39] S. Fre, *et al.*, "Notch and Wnt signals cooperatively control cell proliferation and tumorigenesis in the intestine", *PNAS 106*, pp. 6309-6314, 2008.
[40] J.F. Deux et al., "Aortic aneurysms in a rat model: in vivo MR imaging of endovascular cell therapy", Radiology, 246, pp. 185-192, 2008.
[41] D. E. Jaalouk & Lammerding, "J. Mechanotrasduction gone awry". *Nat. Rev Mol Cell Biol*, 10, pp. 63-73, 2009.

General Conclusion

This work represents a step forward in the characterization and understanding of human cancer tumours.

3D-US has confirmed its potential in the visualization of human breast cancer tumours. Acquired 3D volumetric Data together with 3D display features might deliver new and beneficial diagnostic information specially on the coronal plane of breast pathology, contributing to a high-resolution morphological assessment free of magnification. Although in most of the studied cases the MRI-based tumour volumes were slightly higher than the 3D-US-based ones, both volumes were in very good agreement. Additionally, 3D-SWE has shown to be in important tool for the characterization of breast cancer tumours, as it offers access to the entire 3D tumour elasticity distribution. Moreover, 3D-SWE also proved to be an excellent complementary technique to 3D-US in the monitoring of patients undergoing chemotherapy treatment for breast cancer lesions. The clinical study showed that tumour elasticity and tumour volume drastically decreased during the chemotherapy treatment in almost all the studied cases.

The pre-clinical study performed on mice in which a human breast carcinoma model had been implanted, showed that for this particular model, tumour size and tumour elasticity were very well correlated. Tumour elasticity and tumour heterogeneity seemed to increase with tumour size during the growth phase. This pre-clinical study also proved that tumour elasticity was well correlated with the proportion of necrosis, cellular tissue, and fibrosis present in the tumours during the growth phase. Tumour size seemed to decrease during the chemotherapy treatment. Nevertheless, elasticity did not show any marked trend.

US was successfully used to monitor the human colon cancer tumour response to the antivascular therapy. The treatment seemingly hampered tumour growth. This was evidenced by the fact that the untreated tumours reached much higher volumes than the treated ones. Nonetheless, the study did not allow to conclude whether the antivascular treatment had an effect on the tumour elasticity, as treated and untreated ectopically and orthotopically implanted tumours presented similar elasticity values. The measurements of the tumour elasticity were affected by the tumours' vast necrotic core, generally present from the twelve day in most of the mice.

The combination of Static Elastography and the SSI technique permitted the retrieval with very good precision of the first known quantitative 2D-nonlinear Shear elasticity maps in tissue mimicking phantoms and liver beef samples. By using the method developed to retrieve shear nonlinearity, micro-metrical colon tissue displacements and stresses (a few Pascals) were retrieved *ex vivo*. The developed method opens the paths for future applications, in

which shear nonlinearity could give additional information useful to determine the pathological state of a biological tissue.

The outlook for this work seems promising. The 3D-US and 3D-SWE appear to have great applicability in cancer tumour diagnosis and in the monitoring of patients undergoing chemotherapy treatment.

Future echographic devices could offer the calculus of the tissue nonlinear shear elasticity once the technique presented in Chapter 5 has been tested in clinical studies.